A Numerical Investigation of a few Problems in Cloud Microphysics

Taraprasad Bhowmick
* * * * * *

Supervisors
Prof. Mario Trigiante, Supervisor
Prof. Eberhard Bodenschatz, Co-supervisor

I hereby declare that, the contents and organisation of this dissertation constitute my own original work and does not compromise in any way the rights of third parties, including those relating to the security of personal data.

Taraprasad Bhowmick

Göttingen, Germany, December 23, 2020

Summary

Weather forecast and climate models suffer from the difficulty to make accurate predictions because many of the interconnected physical and chemical processes over the diverse scales of atmospheric clouds are not yet well understood and parameterized. Such limitations exist, for example, in our knowledge on broadening of droplet size for rain initiation or with respect to the collisional effectiveness of the droplets or with respect to the processes that produce new cloud particles. This PhD thesis elaborates the numerical investigation on two such topic, namely 1) cloud droplet size broadening and the effect of collision in the cloud edge mixing, and 2) aerosol activation in the wake of large precipitating cloud hydrometeors.

Atmospheric clouds and clear air interfaces create a turbulent mixing, which plays an important role in the life of a cloud. The entrainment and detrainment of the clear air and cloud volume leads to a turbulent mixing at the interface, which results in broadening of the cloud droplet spectrum. In the first part of this thesis (Chapter 2), the transient broadening of three initial mono-disperse cloud droplet populations is studied in a turbulent cloud top interface. The numerical code uses the pseudo-spectral direct numerical simulation (DNS) method along with the Lagrangian droplet equations, and also a model for the collision and coalescence of the droplets. These simulations are initial value problems without the presence of any turbulent forcing model. Therefore, the evolution of in-cloud turbulent kinetic energy (TKE), temperature and the density of water vapor are of transient nature which exhibit a transient decay it their turbulent mixing intensities. The clear air and the cloudy volume mixing through the interface is observed to produce turbulent fluctuations in the fields of the density of water vapor and temperature. These turbulent fluctuations in the transported scalar quantities result in supersaturation fluctuations, which influence the locally the cloud droplet population. The small scale turbulence and the resulting local supersaturation conditions, along with the gravitational forces influence the droplet population at different weights depending on their sizes. This study finds that the larger droplet populations, with the simulated initial 25 and 18 μm radii, show a significant growth as a result of droplet-droplet collision and a higher rate of gravitational sedimentation as a result of comparatively larger size and a higher mass content. However, the simulated

smaller droplet population, with initial 6 μm radius, does not show any droplet-droplet collision. However, a large size distribution broadening is observed in this population due to the differential condensation/evaporation induced by the super-saturation fluctuations and turbulent mixing across the interface, and this droplet population was not influenced by the gravity significantly.

On the other hand, the activation of aerosols inside clouds is still an open scientific question which has significant influence in our understanding about the life cycle of the clouds, their radiative properties and hydrological fluxes. Aerosol activation produces new cloud particles which also contribute to the broadening of particle size through condensation/collisions. Therefore, a detailed understanding on the potentiality of any aerosol activation process is necessary for reliable weather modeling and climate prediction. Recent laboratory experiments have demonstrated that aerosols can potentially be activated in the wake of the precipitating hydrometeors, such as, rain drops, hails etc, because supersaturation can be produced in the wake. However, many of the quantitative aspects of this wake-induced activation of the aerosols in the wake-induced supersaturation of the precipitating hydrometeors remain unclear. In the second part of this thesis, a detailed numerical investigation is conduced in Chapter 3 to understand the evolution of fluid and the transported scalar populations in the wake of such precipitating spherical objects, which is later used in the Chapter 4 for a detailed quantification on the parameter space for the wake-induced supersaturation and its impact on the activation of the cloud aerosols that entrain inside the hydrometeor wake. It is estimated by using the Lagrangian tracking of aerosols that a significant fraction of aerosols are activated in the supersaturated wake. These 'lucky aerosols' are indeed entrained in the vortices of the hydrometeor wake when the hydrometeor produces oblique wake and therefore, these aerosols can reside in this supersaturated wake environment for sufficiently long duration which is necessary for the aerosol activation. This presented study shows that the wake-induced activation of aerosols can produce some significant concentration of new cloud particles that is similar to the other well known secondary particle production processes.

Acknowledgements

Finally I want to sincerely thank my wife, Trina Das, without whose continuous support this PhD would not become possible.

Contents

List of Tables

List of Figures

xv

XVII

XVIII

Chapter 1

Introduction

Atmospheric clouds play a significant role in both the local and global evolution of the weather and the climate. The clouds control the energy and the hydrological cycle by impacting the incoming and outgoing solar radiations and by affecting the amount of precipitations [123]. Cloud are important for the transport of water vapor, heat, and other advected scalars, e.g., the pollutant concentrations. Clouds are omnipresent in our visible atmosphere and varies a lot in terms of location, altitude, depth, moisture content, particle size distribution and many more [56]. Out of all these types of clouds, the low altitude stratocumulus and cumulus clouds over the tropics and the subtropics cover a large portion of earth's atmosphere and therefore controls the earth's radiative budget [153], however they mostly result in light precipitation. While the deep convective clouds mostly result in high precipitation and dominates the global precipitation budget [97]. Studies have shown that the warm rain accounts for approximately 31% of the total rainfall and about 72% of the total rain area in the tropics [84]. These low level warm clouds and the deep mixed phased convective clouds are typically formed on top of the planetary boundary layer. Although the importance of the atmospheric warm low level clouds and the deep convective clouds on the evolution of the weather and climate is well documented, a number of physical and chemical processes inside clouds are still not well understood and parameterized [134]. Such processes which have a direct impact on the cloud life cycle, however are still not well understood are for example, the processes of droplet size broadening for the rain initiation [27], or the collisional effectiveness of the droplet-droplet collision and the influencing factors behind it [113], or the processes that produce new cloud particles inside a mature cloud [25]. However, all such processes inside these clouds, which span over a wide range of temporal and spatial scales [16], are important for our understanding of the clouds, and for realistic weather and climate forecasting. Therefore, these processes need to be carefully investigated to improve the weather predictions and climate modeling (see Pruppacher and Klett (2010) [116], Stull (1988) [135] and Devenish et al. (2012) [27]).

1.1 Droplet Size Broadening in Cloud Turbulence

This section of the Introduction presents an overview, motivation and the state of the art for investigations of the droplet size broadening within the clouds and in the interface, with exposure to the cloud turbulence and mixing. Atmospheric clouds contain a vast range of dynamically active scales which are interconnected and therefore, adds a layer of complexity to the microphysical processes that are relevant for the cloud droplet evolution. Droplet condensation/evaporation, preferential concentration, dispersion, and the cloud transport processes are the most important ones behind the microphysical evolution of the cloud droplets [27, 127]. However, the smallest scales of the flow [46] have dominance over these microphysical processes, which indeed can not be solved in the large scale simulations or in the atmospheric circulation models. Therefore, such processes need to be parameterized accurately for a realistic prediction by the models which solve the whole cloud or much larger spatio-temporal extent [14, 89]. Therefore in order to investigate the cloud droplet microphysical evolution in the dynamically significant scales of a turbulent environment, the particle resolving direct numerical simulations (DNS) have been used extensively to investigate some of the cloud microphysical processes, however, using some idealized atmospheric flow configurations.

In such simulations, not only all the turbulent scales down to the diffusive scales must be solved, but also the motion [92] and the growth of every single cloud droplet in the fluid flow need to be tracked. However, due to the computational limitations and the computationally intensive nature of such DNS studies, only a small portion of a cloud could be considered. The basic numerical model used in all such works was introduced by Vaillancourt et al. (2001) [148]. In this model the Navier-Stokes (NS) equations with the Boussinesq approximation [86] are solved for the air phase on an Eulerian grid. The suspended cloud droplets are considered as inertial variable-mass points. The cloud droplet model takes into account the variation of the droplet size due to condensation or evaporation following the local interpolated supersaturation conditions [116]. Such works on one hand, mostly focused on the simulation of a small portion of the homogeneously mixed cloud-core, and introduced an external forcing to reproduce the inflow of turbulent kinetic energy as a result of the larger-scale cloud motions [149, 77, 81]. The other studies on the other hand, have extended this methodology to investigate the effects of non-uniformity in the underlying turbulent flow, and focused on its consequences on the cloud droplet microphysical evolution. Such non-uniformity was introduced, for example, in the form of a turbulent kinetic energy (TKE) gradient and a gradient in the supersaturation distribution [44]. Götzfried et al. (2017) [44] and Kumar et al. (2014, 2017) [78, 79, 80, 140] for example, considered the turbulent evolution of a thin slice of the cloud layer with adjacent ambient clear air layers to analyze the cloud edge affects on the cloud droplet population. Whereas, Andrejczuk et al. (2004, 2006, 2009) [2, 3, 4] have considered the decaying moist turbulence with

2

worm-like structures of supersaturated and subsaturated regions. Gao et al. (2018) [41] investigated the differences between cloud microphysical evolution for various initial configuration of cloud and clear air layers, both considering the presence and the absence of turbulent forcing.

The interface between the turbulent cloud and non-turbulent/turbulent ambient results in entrainment/detrainment [94] and mixing in between supersaturated and subsaturated air parcels. Such cloud edges for several last decades are considered to have significant influences on the size distribution of the cloud droplets [27]. The broadening of the droplets through inhomogeneous mixing contributes to enhance the collision and coalescence rate [116, 82]. Therefore, understanding of the cloud droplet evolution inside the mixing zone will contribute to bridge the gap known as the 'condensation - coalescence bottleneck' in between between the condensational growth (effective for smaller droplets, below 10 μm radius) [34] and the collisional growth (effective for larger droplets, above 40 μm radius) of the cloud droplets [46, 147]. In the cloud edge mixing zones, two mechanisms influence the droplet microphysics significantly: a) the presence of large fluctuations in the supersaturation, which broadens the cloud droplet size distribution by the condensation/evaporation of water vapor, and b) the large accelerations in some localized regions of the clouds [127, 132], that result in occasional collisions between the droplets. However, the efficacy of droplet-droplet collision is strongly dependent on the droplet size distribution as well as the intensity of turbulent mixing [112]. Moreover depending on the location of entrainment and mixing, different physical processes are observed in the evolution of the droplet size distribution. The droplet population may experience supersaturation conditions in between the two limiting mixing situations: a) homogeneous mixing, where the entrained dry air and the cloudy moist air quickly mix at the small scale, so that the entire droplet population evaporate/condensate at the same time resulting in negligible droplet size broadening [78], and b) inhomogeneous mixing, where only a portion of the volume remains subsaturated/supersaturated and therefore, a part of the droplet population therein quickly evaporate/condensate, whereas, the other parts of the droplet population remains almost unaffected [85], and in combination together, such differential mixing result in significant droplet size broadening.

The previously mentioned studies have detailed many aspects of the in-cloud turbulence, cloud edge mixing, various cloud droplet microphysical processes and their individual impact on the cloud droplet size broadening. However, a comprehensive study on the turbulent mixing through the cloud interface and an investigation on its impact on the various sizes of initial cloud droplet populations and their collisional rate using the Lagrangian tracking of the individual cloud droplets would reduce the gray area about the 'condensation - coalescence bottleneck'. The presented study in the Chapter 2 aims to overcome this knowledge gap by conducting a series of pseudo-spectral direct numerical simulations using the Eulerian-Lagrangian model along with a collision detection algorithm for various

initial monodisperse cloud droplet populations, which is also reported in Bhowmick and Iovieno (2019) [9]. Following the investigation of transient dynamics of different initial monodisperse droplet populations in the same initial background turbulent interface conditions, a serious of simulations are conducted with the same initial monodisperse population of 20 μm radius droplets in various initial saturation and airflow stratification conditions to understand the impact of these flow configurations on the droplet size broadening.

1.2 Impact of Aerosols in Cloud Interactions

In this section of the Introduction, an overview, motivation and the state of the art for investigating the production process of secondary particles in the cloud are presented. As previously mentioned, the processes that produce new cloud particles inside a mature cloud [25] is an open area of research. Especially the activation of aerosols and species therein controls the lifetime of a cloud [73] in which fractions of cloud condensation nuclei (CCN) and ice nucleating particles (INP) develop into new hydrometeors [8]. Physical processes contributing to the activation [35] within a mature cloud can not explain the observed discrepancies between the measured activation and the observed hydrometeor population, which is several orders of magnitude higher than the expected activation [116, 58]. Moreover, since the supersaturation condition of such clouds are just nearly saturated [69], new aerosols can not activate in it due to their activation barrier. One possible explanation of this riddle might be the wake-induced supersaturation [39, 38, 20] and activation of aerosols behind large precipitating hydrometeors, i.e. wake-induced nucleation [114, 115]. However, the existence of supersaturation in the wake of a hydrometeor was considered to have neglible impact on the activation of aerosols in the earlier works by Nix and Fukuta (1974) [105], and Fukuta and Lee (1986) [38]. This overview, however, changed recently when the experimental investigation by Prabhakaran et al. (2017) [114] on the falling drops (diameter of $\mathcal{O}(1)$ mm) in near critical point conditions of pressurized sulfur-hexafluoride showed evidences of homogeneous nucleation in the wake. However, homogeneous nucleation from pure water vapor is extremely rare due to the very high nucleation barrier [24]. Prabhakaran et al. (2020) [115] conducted a follow-up experiment on heterogeneous nucleation using sodium chloride and silver iodide aerosols under atmosphere-like conditions. Warm droplets with a diameter of ~ 2 mm were able to induce the activation of aerosols into CCNs and INPs in their wake when precipitating through a subsaturated colder environment. Recently, a numerical analysis of supersaturation in the wake of a warmer hydrometeor moving through various colder environments was performed by Chouippe et al. (2019) [20]. Their work confirms the existence of a supersaturated region in the wake of a hydrometeor that settles through a colder saturated environment. The maximum supersaturation observed in the wake was

higher when the temperature difference between the hydrometeor and the ambient was the larger. In a more recent study, Krayer et al. (2020) [72] extended their earlier work [20] and explicitly estimated the influence of wake supersaturation on the ice enhancement factor using a model based on a power law dependence of the local supersaturation [60, 7] and concluded that the local ice nucleation enhancement alone cannot produce a sufficient number of activated ice nuclei to solve the observed number discrepancy that is stated previously.

Although the development of supersaturation was studied numerically, direct computation of nucleation remained rather difficult as it depends on a very wide range of parameters, including the size distribution of the sub-micrometer aerosol particles [28], number concentration [8], chemical composition [75, 25], porosity or solubility [67] of the aerosols, presence of other bio and ion species [24], and also on few other factors. Processes responsible for entrainment of small aerosol particles from the lower free troposphere to the boundary layer are also complex, which for example, can happen during strong downdrafts created by convective precipitation [151]. However, activation does not happen all the time despite the abundance of sub-3 nanometer sized particles in the atmosphere throughout a diurnal cycle [76]. Moreover, studies have shown that the deactivation and reactivation of aerosols result in droplet size broadening inside clouds [155]. Complexity in the nucleation of an aerosol deepens further in mixed phase clouds containing both water and ice phased hydrometeors. Ice-nucleation due to deposition and condensation-freezing can happen on an aerosol during supersaturation with respect to ice phase at freezing temperatures [95]. Activation of the aerosols through immersion freezing on a CCN or by contact freezing on a supercooled water droplet is also witnessed [29, 67]. The activation of aerosols as a CCN or an INP happens through different physical and chemical processes, which are active at different thermodynamic, cloud and aerosol conditions. For example, Petters and Wright (2015) [111] evidenced that a negligible concentration of INP exists at a cloud temperature higher than $-5\,°C$, while the concentration of INP at cloud temperatures between $-5\,°C$ to $-15\,°C$ can vary up to 5 orders of magnitude. This variability in the number concentration of INP decreases as the temperature of the clouds reduces [111, 49]. The review by Hoose and Möhler (2012) [55] presents a general overview of the various INP production processes, such as, immersion freezing, deposition nucleation, contact nucleation, evidencing their strong dependence on the ambient temperature, supersaturation condition and the aerosol species.

This study of the wake-induced supersaturation behind the precipitating hydrometeors is one of many engineering and scientific studies which need to understand the nature of the wake, evolution of the fluid and the transported scalars and the interactions behind the spherical/near-spherical objects in fluid flow [23, 96]. This flow past a sphere presents different regimes at different Reynolds number Re, based on the sphere diameter, the velocity of the incoming flow and the viscosity. The steady axisymmetric structure of a wake at low Reynolds number,

up to $Re \sim 210$, was studied experimentally, for example by Teneda (1956) [139] and numerically by Tomboulides and Orszag (2000) [142] among others [104]. The steady axisymmetric regime is followed by a steady oblique wake structure, with Re up to 280, which was observed experimentally by Magarvey and Bishop (1961) [90] and numerically by Johnson and Patel (1999) [66] for example. An unsteady structure of the wake appears at higher Re, and was reported by Fornberg (1988) among others [36, 109]. The drag coefficient C_D of a sphere, which varies with the roughness of the sphere surface and Re, was studied in detail, for example, by Eichhorn and Small (1964) and others experimentally [15, 122, 30, 146] and by Tabata and Itakura (1998)[138], Birouk and Al-Sood(2007) [13] numerically. At present, how the drag, lift and pressure coefficients vary both locally as well as globally with respect to the sphere is well known [142, 13, 154]. The two dimensional structures of the streamlines, vorticity and pressure contours along the orthogonal central planes through the sphere are also well known over various studies, such as, Tomboulides and Orszag (2000) [142] and others [66, 5].

Many engineering applications and natural processes, for example, the wake-induced supersaturation behind the precipitating hydrometeors rely on understanding the interactions between a sphere and the ambient, also involving the transport of various scalar species, either passively advected by the ambient flow or interacting actively with the flow through various physical processes, for example, through evaporation and buoyancy. The rate of scalar transport, in particular the convective heat transfer from spherical objects at various Re, has been investigated both numerically, for example, by Bagchi et al. (2000) [5] and Richter and Nikrityuk (2012) [121] and experimentally by Kramers (1946), among others [71, 42, 157, 152] to determine the heat transfer coefficient. Similar to the drag coefficient, attention was given to the dependence of the local Nusselt number (a ratio of the convective and the diffusive (conductive) heat transfer) on the sphere surface and its global average for different Re [5, 152]. The profiles of the dimensionless temperature contours along the central orthogonal plane for various Re have also been described in the studies by Bagchi et al. (2000) [5] and Chouippe et al. (2019) [20]. A coupled system involving an interplay between different scalars can also be present, for example, in case of the phase change during droplets evaporation or freezing resulting in heat and mass exchange with the ambient air. Such interaction has also been studied both experimentally by Ranz and Marshall Jr. (1952) [120] and Friedlander (1957) [37] and numerically by Dennis et al. (1973) [26] and Chouippe et al. (2019) [20]. All these studies are mainly concerned with the average scalar flux at the surface of the sphere, which determines the mass and temperature change rate of the sphere. However, a detailed description of the wake regarding the spatial evolution of the fluid velocity and scalar populations, including the scalar concentrations and the convective fluxes, both in two and three dimensions for various steady Re, have not been fully explored.

Descriptive statistics on the spatial structure of the wake is of primary importance if the extent of the wake with certain properties needs to be quantified. Supersaturation in the wake of precipitating cloud water droplets, which have important implications for cloud life cycle as investigated by Bhowmick et al. (2020) [11] and Krayer et al. (2020) [72], requires for example a detailed analysis of the transported scalar population in the wake. In order to quantify the extent of the supersaturated volume in the wake of a cloud hydrometeor, where aerosols can grow by the deposition of the excess water vapor in the supersaturated wake and can be activated due to sufficiently long exposure to supersaturation in the droplet wake [11]; the details of the scalar population in the wake need to be known with a quantification on the scalar transport and its population distribution. Therefore in the Chapter 3, a comprehensive numerical study on the details of the momentum and scalar transport in the wake of a sphere using a population density distribution for the steady axisymmetric and oblique wake regimes is presented. Based on the foundation of the scalar transport studies in the Chapter 3, a detailed investigation on the parameter space of the wake-induced supersaturation behind precipitating hydrometeors is conduced in Chapter 4. In the Chapter 4, the cloud aerosols are also introduced as Lagrangian tracers due to their negligible Stokes number, and a detailed analysis on the aerosol activation potential of the wake-induced supersaturation behind precipitating hydrometeors is being reported.

End of Chapter 1

Chapter 2

Cloud Droplet Population in Warm Cloud Top Interface

A part of this chapter is already published in Bhowmick, T. and Iovieno, M. (2019), "Direct Numerical Simulation of a Warm Cloud Top Model Interface: Impact of the Transient Mixing on Different Droplet Population", Fluids, volume 4, issue 3, article number 144 [9]. In this chapter, the transient evolution of cloud water droplet populations inside a simplified top interface model of a warm cloud is presented. The objective of this work is to investigate the differences in microphysical transient evolution of various cloud water droplet populations with sizes which approach the lower bound of the size gap [15-40 μm radius] [46] and sizes below the size gap, and their feedback on the surrounding air. Direct numerical simulations (DNS) using the Eulerian-Lagrangian model along with a collision detection algorithm (mostly neglected for this kind of studies) are used for this work (see also Onishi et al. (2015) [107]). Various thermodynamic processes, such as, supersaturation, buoyancy, phase change of water vapor to liquid water and corresponding latent heat production are interlinked by one-way coupling in between the cloud droplets and the surrounding fluid velocity, and two-way coupling of the cloud droplets with the air temperature and the water vapor density. This study investigates the momentum and scalar transport inside a cloud interface characterized by a strong kinetic energy gradient (see also Götzfried et al. (2017) [44]). Such configuration generates a strong intermittent transient mixing layer [144, 62, 63] as a result of the entrainment/detrainment of fluid from/to the ambient regions to/from the near interface cloud volume [63, 21]. This introduces non-trivial complex behavior in the droplet velocity distribution as a result of the interplay between larger scales and the gravity, with very little dependence on the simulated Reynolds number [63]. Therefore, even if the simulated Reynolds number which can be achieved in the direct numerical simulations is much smaller and not comparable at all with the real life cloud Reynolds number which is in the order of $10^4 - 10^5$, it is considered that such low Reynolds number simulations still can provide information

that can be useful to understand some of the real cloud phenomena. The present simulations undergo a transient decay in the turbulent kinetic energy (TKE) [32, 2, 44, 21]. The methodology and the simulation set-up for this study is presented in section 2.1 and 2.2. Results are presented in section 2.3 which include statistics and visualizations on the transient evolution of the fluid flow and statistics of the droplet populations. A discussion on the role of condensation/evaporation, sedimentation, flow stratification conditions and droplet-droplet collisions on the evolution of the different droplet populations is also presented in regards to the mixing layer separating the lower cloudy region from the upper clear air region. A summary and conclusions of this chapter is given in Section 2.4.

2.1   Details of the Physical Model

This study simulates the interactions in between the low altitude warm cloud top and the above-lying ambient clear air regions, and investigates its impact on the cloud water droplets by using the DNS. Two cubic boxes, each of 0.256^3 m^3 volume; one representing the warm cloud and the other representing the associated clear air region with different turbulent and thermodynamic properties are combined together, to create the simulation domain (see Figure 2.1(a)). The portion of the domain representing the cloudy air is seeded with a cloud droplet population of mono-disperse size distribution. The airflow is modeled with the incompressible fluid flow conditions along with the Boussinesq approximation for the computation of the buoyancy feedback to the fluid flow.

In this physical model, the cloud droplets are considered as point-particles, with variable mass as one of its attributes. This simplification avoids the necessity to solve the details of the fluid flow around each single droplet, and therefore, makes this approach feasible for the simulations of more than a few droplets. However, there are justifications associated to it. 1.) One has to assume that the sizes of the particles are much smaller than the smallest flow scale which is the Kolmogorov scale in a turbulent flow. In this study, the diameter of the cloud droplets are in μm range, while the Kolmogorov scale is in mm range, and therefore it is justified to use the point-particles model. 2.) Also the concentration of the particles must be small in the ambient fluid, so that one particle does not interact directly with another neighboring particle. This means that the regions perturbed by the different particles do not overlap, so that each particle does not directly see the perturbation in the flow, which is induced by other particles. Basically, in case of a volume fraction of the particles less than 10^{-6} of the ambient fluid, the point-particles with one-way coupling is a valid model, and for a volume fraction less than 10^{-3}, one should consider point-particles with two-way coupling, according to Elghobashi (1991) [31]. The governing equations for the airflow which is the carrier fluid and the cloud droplets which are the dispersed medium, are presented below.

2.1.1   Equations for Solving the Flow Field

The numerical model for the evolution of the fluid flow considers Navier-Stokes (NS) equations for humid air. This model is coupled with the individual Lagrangian tracking of cloud water droplets, which are introduced in the initial condition. The numerical model of this study follows the similar model used by Vaillancourt et al. (2001) [148], which is later also used by Kumar et al. (2014) [78], Gotoh et al. (2016) [43], Götzfried et al. (2017) [44], Gao et al. (2018) [41]. The air phase equations use a Boussinesq-like approximation [86]. The fluid flow model include the continuity and the momentum balance equations for the airflow velocity $\mathbf{u} = (u_1, u_2, u_3)$, and the temperature T and the water vapor density ρ_v equations, known as Advection-Diffusion (AD) equations. Temperature and water vapor density are modeled as advected active scalars, which interact with the fluid flow through the buoyancy feedback. The fluid flow equations are:

$$\nabla \cdot \mathbf{u} = 0 \tag{2.1}$$

$$\frac{\partial \mathbf{u}}{\partial t} + \mathbf{u} \cdot \nabla \mathbf{u} = -\frac{1}{\rho_0} \nabla p + \nu \nabla^2 \mathbf{u} - B\mathbf{g} \tag{2.2}$$

$$\frac{\partial T}{\partial t} + \mathbf{u} \cdot \nabla T = \kappa \nabla^2 T + \frac{L}{\rho_0 c_p} C_d \tag{2.3}$$

$$\frac{\partial \rho_v}{\partial t} + \mathbf{u} \cdot \nabla \rho_v = \kappa_v \nabla^2 \rho_v - C_d \tag{2.4}$$

where $\partial / \partial t$ is the temporal derivative, ρ_0 is reference mass density of air at temperature T_0 and pressure p_0, ∇p is the pressure gradient, ν is the kinematic viscosity, $\mathbf{g} = (0,0,-g)$ is the gravitational acceleration, κ is the thermal diffusivity of air, L is the latent heat for condensation of water vapor, c_p is the specific heat at constant pressure, and κ_v is the water vapor diffusivity. The buoyancy B in the momentum balance equation (2.2) is the "source" term which represents the buoyancy force per unit volume due to small variations of temperature and water vapor density in the humid air. In the temperature or the enthalpy (2.3) and the humidity (2.4) equations, the source term C_d represents the condensation rate of the water vapor, that is, the local condensating or evaporating water mass per unit time and unit volume.

These source terms are expressed as:

$$B = \frac{T - T_0}{T_0} + \epsilon \frac{\rho_v - \rho_{v,e}}{\rho_0} \tag{2.5}$$

$$C_d = \frac{1}{V} \sum_i \frac{\mathrm{d}m_i}{\mathrm{d}t} = \frac{1}{V} \sum_i 4\pi \rho_L r_i^2 \frac{\mathrm{d}r_i}{\mathrm{d}t} \tag{2.6}$$

where T_0 is the reference temperature, $\rho_{v,e}$ is the reference density of the water vapor, $\epsilon = R_v/R_a - 1 = 0.608$ is a constant dependent on the gas constants R_v and

11

R_a of the water vapor and the air respectively, ρ_L is the density of liquid water, and r_i is the radius of the i-th cloud droplet. The sum in the feedback term C_d is calculated on the droplets only within the (small) local volume V, where m_i is the mass of the i-th droplet. In the simulations, this volume V is the volume of a computational grid cell. Droplet volume fraction, which is the ratio of the volume of droplets to the volume of carrier fluid, for the largest initial droplet population with the initial radius, $r_{in} = 25\ \mu$m, is 1.12×10^{-6}. This is considered as a dilute suspension by Elghobashi (1991) [31], where the momentum feedback from the droplets in form of the two-way momentum coupling can be neglected. Therefore, in the computation of the buoyancy force, no momentum feedback is considered from the droplets to the fluids. In case of the dilute suspension, one-way coupling is sufficiently accurate to capture the interactions in between the droplets and the surrounding fluid [31]. The numerical model of Vaillancourt et al. (2001) [148] considers water vapor mixing ratio $q_v = \rho_v/\rho_d$ (ρ_d is the mass density of the dry air) as the transported active scalar instead of the density of water vapor ρ_v. However, due to negligible changes in the ρ_d for the considered temperature and relative humidity conditions, the equations of ρ_v and q_v are analogous, with appropriate changes in the feedback term C_d.

2.1.2   Equations for Cloud Droplets as Lagrangian Particles

The Lagrangian descriptions of the cloud droplets consider them as inertial point particles driven only by gravity and the Stokes drag [158]. Since the droplet density is much higher than air density ($\rho_L/\rho_0 \sim 10^3$) and the Reynolds number of the droplet relative velocity with respect to the surrounding air is very small (after Pruppacher and Klett (1978) [116] pg 575 and Vaillancourt et al. (2001) [148], usually below 0.1), the Stokes drag model is used. Moreover, their sizes change due to the condensation/evaporation of the water vapor, which is driven by the local heat and water vapor diffusion around the droplets. The equations for the i-th droplet are presented below:

$$\frac{\mathrm{d}\mathbf{x}_i}{\mathrm{d}t} = \mathbf{v}_i \tag{2.7}$$

$$\frac{\mathrm{d}\mathbf{v}_i}{\mathrm{d}t} = -\frac{\mathbf{v}_i - \mathbf{u}(\mathbf{x}_i, t)}{\tau_i} + \mathbf{g} \tag{2.8}$$

$$\frac{\mathrm{d}r_i}{\mathrm{d}t} = C\frac{\varphi(\mathbf{x}_i, t) - 1}{r_i}, \quad \varphi(\mathbf{x}_i, t) = \frac{\rho_v(\mathbf{x}_i, t)}{\rho_{vs}(T)(\mathbf{x}_i, t)} \tag{2.9}$$

where $\mathbf{x}_i$ is the droplet position, $\mathbf{v}_i$ is the droplet velocity, φ is the local relative humidity, ρ_{vs} is the density of saturation vapor, and τ_i is the droplet response time, which is:

$$\tau_i = \frac{2}{9}\frac{\rho_L}{\rho_0}\frac{r_i^2}{\nu}. \tag{2.10}$$

The droplet growth rate equation (2.9) is dependent on the condition of surrounding relative humidity (Pruppacher and Klett (1978) [116] pg 511), and the proportionality coefficient C is defined as:

$$C = \kappa_v \frac{\rho_{vs}(T_0)}{\rho_L} \left(1 + \frac{L^2 \rho_{vs}(T_0)}{R_v T_0^2} \frac{\kappa_v}{\lambda_T} \right)^{-1}$$

where λ_T is the thermal conductivity of the air. As in Kumar et al. (2013) [77], $L/(R_v T)$ is approximated as $\gg 1$ in the definition of C. A details on the derivation of the dimensionless equations can be found in the Appendix A of this thesis.

2.2   Details of the Numerical Method in DNS

Model equations for the fluid flow phase are solved using the Fourier–Galerkin (FG) pseudo-spectral method as in Iovieno et al. (2001) [61]. The temporal advancement is approximated using a low storage second order Runge-Kutta (RK2) method with exponential integration of the diffusive terms [53]. The numerical code uses one dimensional (1D) slab parallelization using Massage Passing Interface (MPI) libraries. De-aliasing is carried out during the data transposition. Discrete Fourier Transforms (DFT) are computed using the FFTW subroutine library. On the other hand, the Lagrangian model equations for the droplets are solved in the physical space using the same RK2 method for the temporal integration. After every time-step, droplets are exchanged among neighbouring processors/tasks according to their current respective positions. The fluid velocity, temperature and vapor density at particle positions are computed through a trilinear interpolation within each mesh cell. This trilinear interpolation is expected to be sufficient in the Lagrangian droplet model when $k_{max}\eta \gtrsim 2$. The feedback term C_d is computed through the cell averaging (particle-in-cell method). A higher order interpolation methods, e.g. third order B-spline method would be optimal according to van Hinsberg et al. (2013) [52], in the sense that the interpolation error of the third order B-spline method would be less than the discretization error. However, as outlined by Sundaram and Collins (1996) [137], the interpolation and the reverse interpolation schemes must be symmetric in order to guarantee the energy conservation in the domain. Therefore, the linear particle-in-cell reverse interpolation should be replaced with an equivalent higher order method (see for example Carbone and Iovieno (2018) [18]).

The pseudo-spectral code used triply-periodic boundary conditions for all the fluid flow variables. A non-periodic temperature profile is introduced in the vertical direction by the decomposition of T as $\Gamma x_3 + T'$; where, the field T', which contains the temperature fluctuations, is triply periodic, but the full temperature field T is not periodic in the vertical direction. The initial condition for T' increases linearly from the reference temperature $T_0 = 283.16\,°C$ to $285.16\,°C$ in the cloudy part of

the domain, while it drops at the interface near $x_3/L_{x_3} = 0$ by $4\,^\circ\text{C}$ (see Figure 2.1(d)), and again increases linearly from $281.16\,^\circ\text{C}$ to $283.16\,^\circ\text{C}$ inside the clear air part of the domain. Therefore, the temperature field T has only one interface at $x_3/L_{x_3} = 0$. Sign of temperature gradient $\Gamma = \Delta T/L_{x_3}$ determines the stability of the flow. With this decomposition, domains can be simulated for stable, unstable or neutrally stratified airflow conditions. Such decomposition of the temperature field modifies the temperature equation (2.3) into:

$$\frac{\partial T'}{\partial t} + \mathbf{u} \cdot \nabla T' = \kappa \nabla^2 T' + \frac{L}{\rho_0 c_p} C_d - \Gamma u_3. \tag{2.11}$$

The code also includes a detection module for the droplet-droplet binary collision. This module implements coalescence of the colliding droplet masses. After each time-step, the algorithm looks for if the distances between the pairs of droplet centers become smaller or equal to the sum of their redii, by assuming a linear in time variation of radius and position within the each time-step. A collision between droplet i and j is considered to have occurred, if the first solution of $|\mathbf{x}_i(t) - \mathbf{x}_j(t)|^2 - (r_i(t) + r_j(t))^2 = 0$ lies between t and $t + \Delta t$, and their relative velocity acts inward. Since the droplet Weber numbers, which are the ratios between the droplet kinetic energy and droplet surface energy, are very small ($\ll 1$), each collision is modeled as a successful coalescence. This is in agreement with the experimental investigation of water droplet collisions by Rabe et al. (2010) [118]. Conservation of the mass and the momentum are then used to determine the size, position and the velocity of the new droplet which emerges from the collision.

2.2.1   Details of the Simulation Setup

The simulation domain replicates a small portion of a warm cloud top and a layer of clear air above it. All the interactions in between the cloud and the clear air happens through the interfaces which are formed at the edges of both the cloud and the clear air regions. Simulation parameters, constants and domain specifications used in our simulations are tabulated in Table 2.1. The values of the basic referred states correspond to the reference height H_{ref} of 763 m, which is a typical height for the low altitude warm clouds as described in Jen-La Plante et al. (2016) [65].

Table 2.2 summarizes the details of the simulation runs. In the simulation setup, an initial population of mono-disperse cloud droplets of three different droplet size distributions are introduced in the cloudy volume of the simulation domain. These simulation runs are **R25**, **R18** and **R6**. Whereas, the carrier airflow initial conditions remained the same for all these simulations. The droplets (which have a different initial size in each simulation) evolve affected by the momentum, thermal energy and the water vapor density of its surrounding airflow, and these populations undergo various microphysical processes such as gravitational sedimentation, preferential concentration, evaporative reduction or condensational growth in size,

and growth by collision and coalescence. A sketch of the simulation domain is shown in Figure 2.1(a). The gravitational force (as presented in Figure 2.1(a)) acts both on the fluid flow (in form of buoyancy forces B in equation (2.2)) and on the momentum of the cloud droplets in equation (2.8). In this cloud top simulation setup, gravity therefore acts in downwards direction $(0,0,-g)$, causing heavier droplets to settle down towards the bottom boundary of the cloudy volume.

Table 2.1: Simulation parameters, constants and domain specifications used for simulation setup.

Quantity (Symbol)	Value	Unit
Reference temperature (T_0)	283.16	K
Reference atmospheric pressure (p_0)	92.4	kPa
Reference air density (ρ_0)	1.13	$\mathrm{kg\,m^{-3}}$
Reference kinematic viscosity (ν)	$1.56 \cdot 10^{-5}$	$\mathrm{m^2\,s^{-1}}$
Gravitational acceleration (g)	9.8	$\mathrm{m\,s^{-2}}$
Thermal conductivity of the air (λ_T)	$2.5 \cdot 10^{-2}$	$\mathrm{J\,K^{-1}\,m^{-1}\,s^{-1}}$
Thermal diffusivity of air (κ)	$2.2 \cdot 10^{-5}$	$\mathrm{m^2\,s^{-1}}$
Diffusivity of water vapor (κ_v)	$2.54 \cdot 10^{-5}$	$\mathrm{m^2\,s^{-1}}$
Specific heat of air at constant - pressure (c_p)	1005	$\mathrm{J\,kg^{-1}\,K^{-1}}$
Latent heat for condensation of - water vapor (L)	$2.5 \cdot 10^6$	$\mathrm{J\,kg^{-1}}$
Gas constant for water vapor (R_v)	461.5	$\mathrm{J\,kg^{-1}\,K^{-1}}$
Gas constant for air (R_a)	286.84	$\mathrm{J\,kg^{-1}\,K^{-1}}$
Density of liquid water (ρ_L)	1000	$\mathrm{kg\,m^{-3}}$
Saturated water vapor density - at T_0 temperature ($\rho_{vs}(T_0)$)	$9.4 \cdot 10^{-3}$	$\mathrm{kg\,m^{-3}}$
Constant in equation (2.9) (C)	$9.22 \cdot 10^{-11}$	$\mathrm{m^2\,s^{-1}}$
Simulation grid step (Δx)	0.001	m
Simulation domain discretization - ($N_1 \times N_2 \times N_3$)	$256 \times 256 \times 512$	
Simulation domain size - ($L_{x_1} \times L_{x_2} \times L_{x_3}$)	$0.256 \times 0.256 \times 0.512$	$\mathrm{m^3}$

2.2.2 Details of the Initial Setup for the Flow Field

In field measurements of the cloud turbulent properties and associated clear air properties show varying turbulent intensities. This produces TKE gradients across the interfaces. Velocity fluctuations inside the cloudy regions [129] mostly show

higher TKE than that of the clear air region as shown in Figure 2.2(a) (see also [65, 91, 131]). This happens mainly due to the instability of the moist air-mass, developed due to the buoyant updraft which results in shear layer formation inside the clouds [45]. This difference in kinetic energy is replicated by the average of velocity fluctuation root mean square (rms) distribution u' in the initial condition (Figure 2.1(c)) of the present simulations. The clear air region of the simulation domain, shown in the right side region of the Figure 2.1(c) have lesser energy than the associated cloudy region (left side of the domain). The kinetic energy ratio between the cloudy domain and the clear air domain has been chosen to be around 20, which is in the range of the values which can be deduced from in-cloud measurements of [65, 91] in Figure 2.2(a).

Table 2.2: Details of simulation runs

| Quantity | Simulation IDs | | |
	R25	R18	R6
Initial Droplet Radius r_{in} [μm]	25	18	6
Total number of initial droplets	286,240	286,240	286,240
Initial droplet number - density $N_d(0)$ [cm^{-3}]	17	17	17
Initial liquid water - content lwc [gm m^{-3}]	1.12	0.42	0.02
Initial Stokes number St	1.59	0.82	0.09
Initial rms of velocity - fluctuations u' in cloud [m s^{-1}]	0.268	0.268	0.268
Initial energy ratio E_{cloud}/E_{air}	20	20	20
Temperature difference between - cloudy and clear air ΔT [K]	4	4	4
Initial integral scale L - of cloud and air [m]	0.0235	0.0235	0.0235
Initial Taylor micro-scale - Reynolds no. Re_λ of cloud	90	90	90
Initial Taylor micro-scale - Reynolds no. Re_λ of air	20	20	20
Simulation time-step Δt [s]	$1.224 \cdot 10^{-4}$	$1.224 \cdot 10^{-4}$	$1.377 \cdot 10^{-5}$
Total simulation duration [s]	2.1	2.1	2.1

The thickness of the initial velocity fluctuations interface, measured as the distance between the horizontal planes where the difference of the TKE is 90% of the difference of kinetic energy between the cloudy and clear air regions, is about
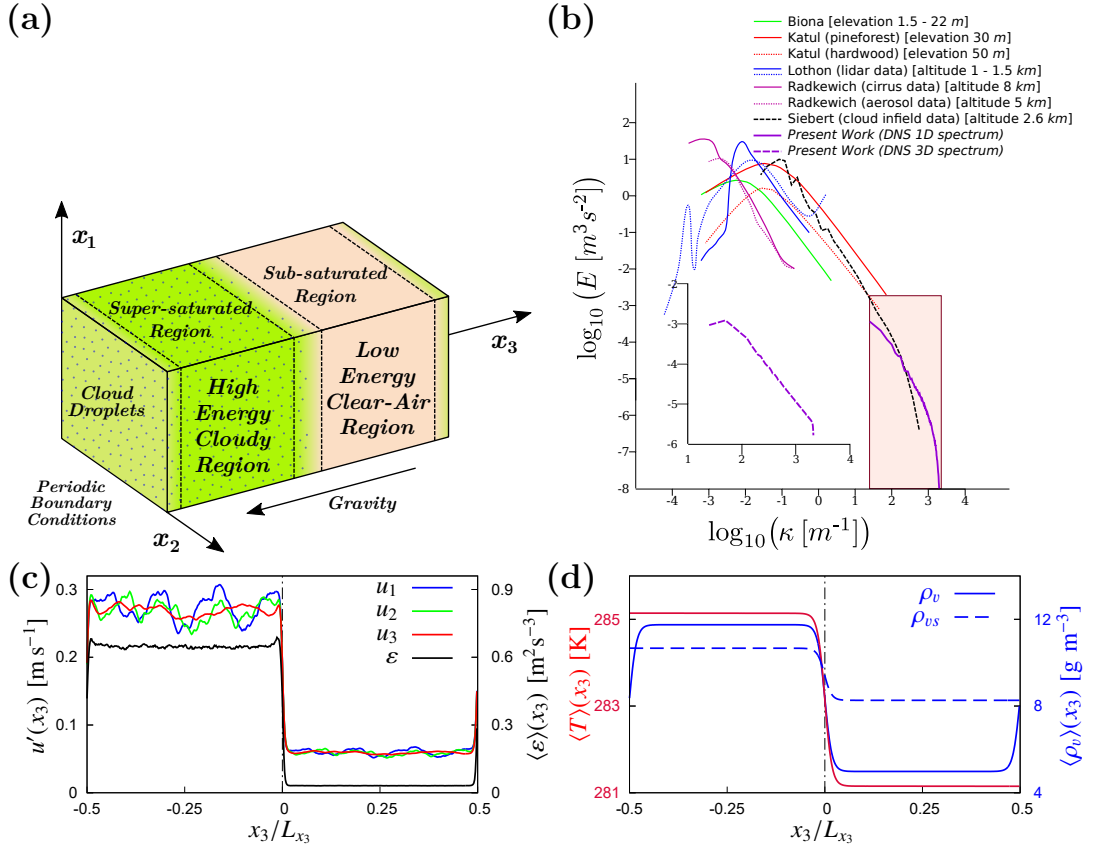
Figure 2.1: Simulation setup:(a) scheme of the three dimensional simulation domain and the boundary conditions; (b) comparison between the TKE spectrum $E(k)$ of present simulation with the infield measurements; (c) initial distribution of the rms of velocity fluctuations u' and TKE dissipation rate $\langle \varepsilon \rangle$; and (d) simulated initial profile of temperature $\langle T \rangle$ and water vapor density $\langle \rho_v \rangle$. The plots in panels (c) and (d) present the horizontal plane averaged quantities (directions (x_1, x_2)) varying along the vertical direction x_3.

0.006 m (see Figure 2.1(c)). Figure 2.1(b) presents few examples of spatial one-dimensional TKE spectra from infield measurements by Biona et al. (2001) [12], Katul et al. (1998) [68], Radkevich et al. (2008) [119], Lothon et al. (2009) [88] and Siebert et al. (2015) [130], to which the one dimensional initial TKE spectrum of the present simulations in the wave-number space k has been superimposed (the three dimensional TKE spectrum is shown in the inset). In a DNS, the Kolmogorov micro-scale η needs to be resolved, which plays an important role for the microphysical evolution of cloud droplets [27, 46]. Therefore, only a fraction of the inertial sub-range and the dissipation range (up to the last three decades of TKE spectrum in logarithmic wave-number space) can only be reproduced. The initial velocity field is generated by the superposition of the Fourier modes with random phases.

17

The amplitudes of these Fourier modes are determined from the following model 3D-spectrum:

$$E(k) = A\frac{(k/k_0)^\alpha}{1 + (k/k_0)^{\alpha+5/3}}f(k/k_{max}).$$

Coefficient α controls the low wavenumber slope of the spectrum ($\alpha = 2$ in present work). Coefficients A and k_0 control the variance and the initial correlation length and $f(k/k_{max})$ produces the exponential tail in the highest simulated wavenumbers approaching $k_{max} = \pi/\Delta x$. The initial one and three-dimensional TKE spectra in Figure 2.1(b) plot the spectra of the initial homogeneous isotropic turbulence (HIT) field of the cubic domain, where k_0 is defined as $2k_{min}$ (k_{min} is the lowest wavenumber) and an exponential tail is created for wavenumbers $k \geq 2k_{max}/3$. Transition of initial fluctuations for airflow velocity from higher values inside the cloudy region $\mathbf{u}_c$ to the lower values inside the clear air region $\mathbf{u}_a$ of the domain is carried out using a hyperbolic tangent function $p(x_3)$ in the vertical direction x_3 for the linear superposition of the two initial cloudy and clear air isotropic fields (see Tordella and Iovieno, (2006) [143], supplemental material of Tordella and Iovieno, (2011) [144], and Iovieno et al. (2014) [62]) as,

$$\mathbf{u}(x_3) = \mathbf{u}_c(x_3)p(x_3) + \mathbf{u}_a(x_3)(1 - p(x_3)^2)^{0.5},$$

$$p(x_3) = \frac{1}{2}\left[1 + \tanh\left(80\pi\frac{x_3}{L_{x_3}}\right)\tanh\left(80\pi\left(\frac{x_3}{L_{x_3}} - \frac{1}{2}\right)\right)\tanh\left(80\pi\left(\frac{x_3}{L_{x_3}} - 1\right)\right)\right].$$

Generally in the numerical experiments, the localized sources of turbulence in stratified environments were created in many different ways, for example, by impulsive or continuous forcing, with or without mean flow. However, all these ways exhibit a common behavior, that the initial vertical growth rate of the turbulent patch is almost unaffected by the stratification. And it reaches a maximum vertical extent on a time scale proportional to the Brunt-Väisälaa frequency N of the ambient fluid,

$$N^2 = -\frac{g}{\rho_0}\frac{\mathrm{d}\rho(x_3)}{\mathrm{d}x_3},$$

where g is the gravity acceleration and ρ_0 the reference density. The interface thickness has been observed to reduce while the frequency increases.

For this study, an unstably stratified temperature profile is selected, which can also be locally observed from the small scale local temperature profiles obtained from in-cloud measurements as shown in Figure 2.2(b) (see also Figure 2 of Ref. [65]). It must be noted that the in-cloud measurements shown in Figure 2.2 show the inclined descent of the measurement aircraft, and therefore are not indicative of an actual vertical profile. However, for the purpose of defining the temperature inside the cloud core of the simulation domain and the temperature of the abovelying clear air zone, the data of Figure 2.2 provide important insights. Initial temperature and water vapor fields are all uniform on the horizontal planes, but
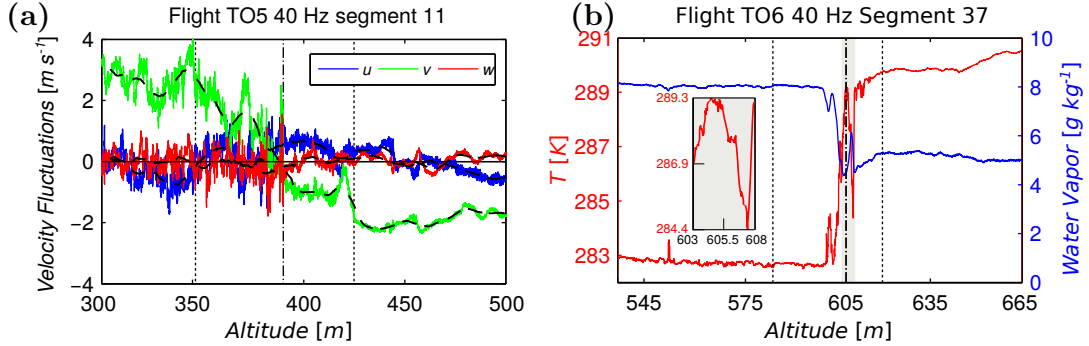
Figure 2.2: In-cloud measurements: (a) the measurements of velocity fluctuations $\mathbf{u}'$ at cloud top interface [65] and (b) the measurements of temperature T and water vapor mixing ratio q_v at cloud top interface [65].

varying in the vertical x_3 direction. No fluctuations for the temperature and the water vapor density have been introduced in the initial conditions. Therefore, the transient supersaturation fluctuations are generated only due to the mixing or due to the condensation/evaporation of the droplets to a minor extent. As a result, any particle size broadening can be attributed to the non-uniform supersaturation field, generated by the mixing process due to the gradient of TKE across the interface. The constants T_0 and $\rho_{v,e}$ in the equation (2.5) are chosen as the mean values of T and ρ_v over the whole domain as in the initial conditions. The thickness of the initial mean temperature and the mean density of water vapor interface is slightly wider, which is around 0.007 m (Figure 2.1(d)). The initial mean density of the water vapor and the unstable mean temperature distribution inside the domain simulate the supersaturated (relative humidity (RH) $\varphi = 1.1$, 10% supersaturation) condition for the cloudy volume and a subsaturated ($\varphi = 0.6$, 40% subsaturation) condition for the clear air volume conditions. The supersaturated condition inside the cloudy region of the simulation domain will help the local cloud water droplets to grow by the deposition of water vapor on them in form of condensational growth. Whereas, the entrainment of the subsaturated clear air inside the cloudy volume will result in subsaturation, and will result in an evaporative size reduction of the cloud droplets. These mean values of the supersaturation are around the upper bound of the atmospheric measurements by Siebert and Shaw, (2017) [128].

2.2.3 Details of the Initial Setup for the Droplets

Three different mono-disperse populations of cloud water droplets of initial 25 μm, 18 μm, and 6 μm radii are initially introduced for the three simulations. The droplets are seeded at random positions inside the cloudy part of the domain, that is, in the supersaturated region of the domain. Initial velocity of the droplets is set to be equal to the interpolated flow velocity at the droplet position.

Boundary conditions for the cloud droplets also follow periodic boundary conditions in the two horizontal directions. This means that the droplets which exit the domain from horizontal boundaries, will re-enter from the opposite side with the same velocity like the fluid flow. However, the droplets which are settling on the bottom boundary of the simulation domain, are removed from the simulation. This is done to consider that those droplets are no longer present inside the cloudy volume. In this way, these settling droplets can not re-enter the simulation domain from the top in the clear air region above the cloud. This choice has both some positive as well some negative impacts on the simulated cloud droplet statistics. Due to gradual removal of the heavier droplets from the cloudy portion of the domain, the number of samples for the averaged droplet quantities were reduced near the bottom boundary of the cloudy volume. However, this removal setup simultaneously prevented the cloud droplets from reappearing inside the clear air part of the domain, as a result of the periodic boundary conditions. Therefore any spurious droplet feedback is removed for the fluid volume near the top of the clear air region. In the simulation, size reduction happens for the droplets only due to the evaporation of the liquid water from their individual masses. In case of a droplet, which reduces below 4% of their initial radius, it is assumed that the droplet is completely evaporated within the next one time-step. This is implemented to avoids the numerical instability of the small droplets, which have the time-scales much smaller than the Kolmogorov time-scale.

2.3 Simulation Results

2.3.1 Transient Evolution of the Flow Field

The evolution of the cloud interface is simulated as an initial value problem, without presence of any kind of volume forcing. Therefore, the only force that can amplify the velocity of the fluid flow is the buoyancy force generated by the variations of temperature and water vapor density in the humid air. Transient evolution of the various volume averaged quantities, such as TKE E, its dissipation rate ε, Taylor micro-scale Reynold's number Re_λ, and integral length scales L exhibit transient decay or growth with time as shown in Figure 2.3. Turbulent fluid statistics along the anisotropic x_3 direction is carried out by plane averaging $\langle \cdot \rangle$ across homogeneous (x_1, x_2) horizontal planes. For the computation of the volume averaged turbulent quantities $\langle \cdot \rangle_V$, the plane averaged quantities $\langle \cdot \rangle$ are again averaged over the bulk of the cloudy region, which is $[1/8 \leq x_3/L_{x_3} \leq 3/8]$, and the bulk of the clear air region, which is $[5/8 \leq x_3/L_{x_3} \leq 7/8]$. The definitions for E, ε, λ, Re_λ and L are given as:

$$\langle E \rangle = \frac{1}{2} \sum_{i=1}^{3} \langle u_i'^2 \rangle; \qquad \langle \varepsilon \rangle = \frac{1}{2} \nu \sum_{i,j=1}^{3} \langle (\frac{\partial u_i'}{\partial x_j} + \frac{\partial u_j'}{\partial x_i})^2 \rangle;$$
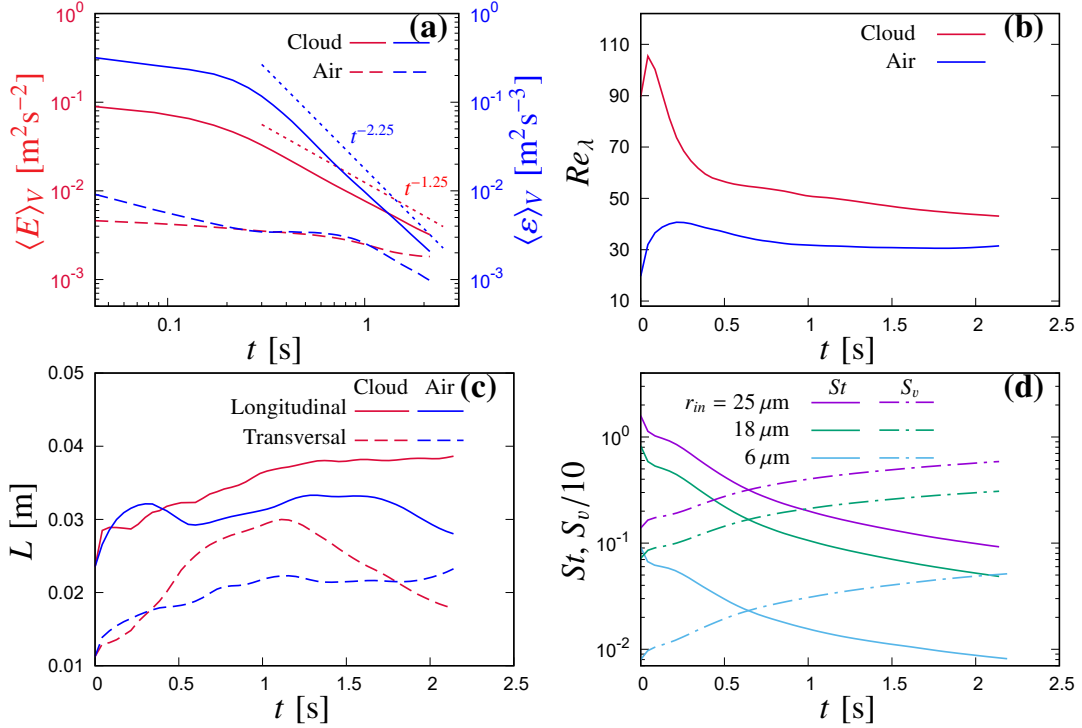
Figure 2.3: Transient evolution of the flow inside the clear air and cloudy region:(a) decay of TKE E and dissipation rate ε; (b) Taylor micro-scale Reynolds number Re_λ; (c) longitudinal and transversal integral length scales L; and (d) average cloud droplet Stokes number St and settling parameter S_v of the different droplet populations. Plots (a-c) are from the simulation **R25**. Differences are small among the three simulations. The plots in panels (a), (b) and (c) present volume averaged quantities for both the cloudy and clear air regions of the simulation domain.

$$u'^2_{avg} = \frac{1}{2}(\langle u'^2_1 \rangle + \langle u'^2_2 \rangle); \qquad \lambda = u'_{avg}\sqrt{\frac{15\nu}{\langle \varepsilon \rangle}}; \qquad Re_\lambda = \frac{u'_{avg}\lambda}{\nu};$$

$$B(r) = \langle u'_i(x_i)u'_i(x_i + r) \rangle; \qquad L = \frac{1}{B(0)}\int_0^\infty B(r)dr;$$

where u'_{avg} is the average of the rms velocity fluctuations along two homogeneous directions (x_1, x_2) along which flow should remain homogeneous and isotropic. This is because the only sources of in-homogeneity and anisotropy are gravity and energy/temperature/density of water vapor gradient, which are all acting along vertical x_3 direction. $B(r)$ is the velocity correlation function [99]. The evolution of E and ε is plotted using logarithmic scale in the both axes in Figure 2.3(a). In order to use logarithmic scale, the initial time in the Figure 2.3(a) is set equal to first saving instance (0.043 seconds), which is used also for the other three plots of Figure 2.3. More than the half of the initial E and ε inside the cloudy region is

decayed during the first 0.3 seconds. After that the evolution of the E and ε follows a power-law scaling with time (with scaling exponent of -1.25 for E, and -2.25 for ε).

Figure 2.3(b) presents time evolution of the Re_λ, which shows two phases in its evolution inside the cloudy region. During the first phase of initial transient till 0.3 seconds, turbulence develops from the initial random conditions. Initially an increase is observed in Re_λ due to the rapid increase in spatial scales (such as λ, L) which is dominant compared to the decrease in E with time. This is followed by the second phase where a sharp decrease in Re_λ is observed, due to the rapid decrease in E with time which dominates over the the increase in λ. During the second phase, E decays at $t^{-1.25}$ while the λ grows as $t^{0.5}$. Therefore, altogether a gentle decay of Re_λ at $t^{-0.125}$ is observed. Since the decrease in E is much slower inside the clear air region than the increase in its spatial scales, and the detrainment of E happens towards the clear air region from the cloudy volume. Therefore, the evolution of Re_λ shows an increment for little longer duration in the clear air compared to the cloudy region, which is rather followed by a slow decrease.

For calculation of the integral length scales L, both the longitudinal and the transversal integral scales are computed along the two homogeneous directions, and they are averaged. In Figure 2.3(c), the transversal length scales are seen not to be exactly one half of the longitudinal length scales, which indicates an anisotropic evolution of the flow across the domain with time. Since the scales can not grow beyond the domain size, the effect of the numerical boundary of the domain also influenced this anisotropic evolution of the integral scale. The decay in the turbulent kinetic energy also produces a growth of the Kolmogorov micro-scale $\eta = \sqrt[4]{\nu^3/\langle\varepsilon\rangle}$. Since $k_{max}\eta$ varies from 1.0 at the beginning to 3.7 at the end of the simulation inside the cloudy region of the domain (inside clear air region, $k_{max}\eta \geq 2$ always), the resolution of the simulation increases with time (see also Elghobashi and Truesdell (1992) [32]). The growth of the η also produces a transient evolution in the average droplet Stokes number St and the settling parameter S_v for the different droplet populations inside the domain, which is shown in Figure 2.3(d). St is a ratio between the droplet response time τ_i in equation (2.10) and the Kolmogorov time scale $\tau_\eta = \sqrt{\nu/\langle\varepsilon\rangle}$. S_v is a ratio between v_p and u_η, where $v_p = \tau_i g$ is the terminal velocity of a droplet, and $u_\eta = (\langle\varepsilon\rangle\nu)^{1/4}$ is the Kolmogorov velocity. Due to a decay in the kinetic energy and the corresponding growth in η in the domain, the droplets become gradually less and less sensitive to the turbulence, which is indicated by the transient growth of the S_v parameter. Whereas, the droplet Stokes number St gradually reduces.

Figure 2.4 presents the time evolution of the fluid/air statistics. Time has been re-scaled using an initial eddy turnover time $\tau_0 = L/u'$ =0.115 seconds, which is taken at t =0.043 seconds (the first saving instance). This shift in time τ_0 is done in order to reduce the influences of the initial evolution phase of the flow, when
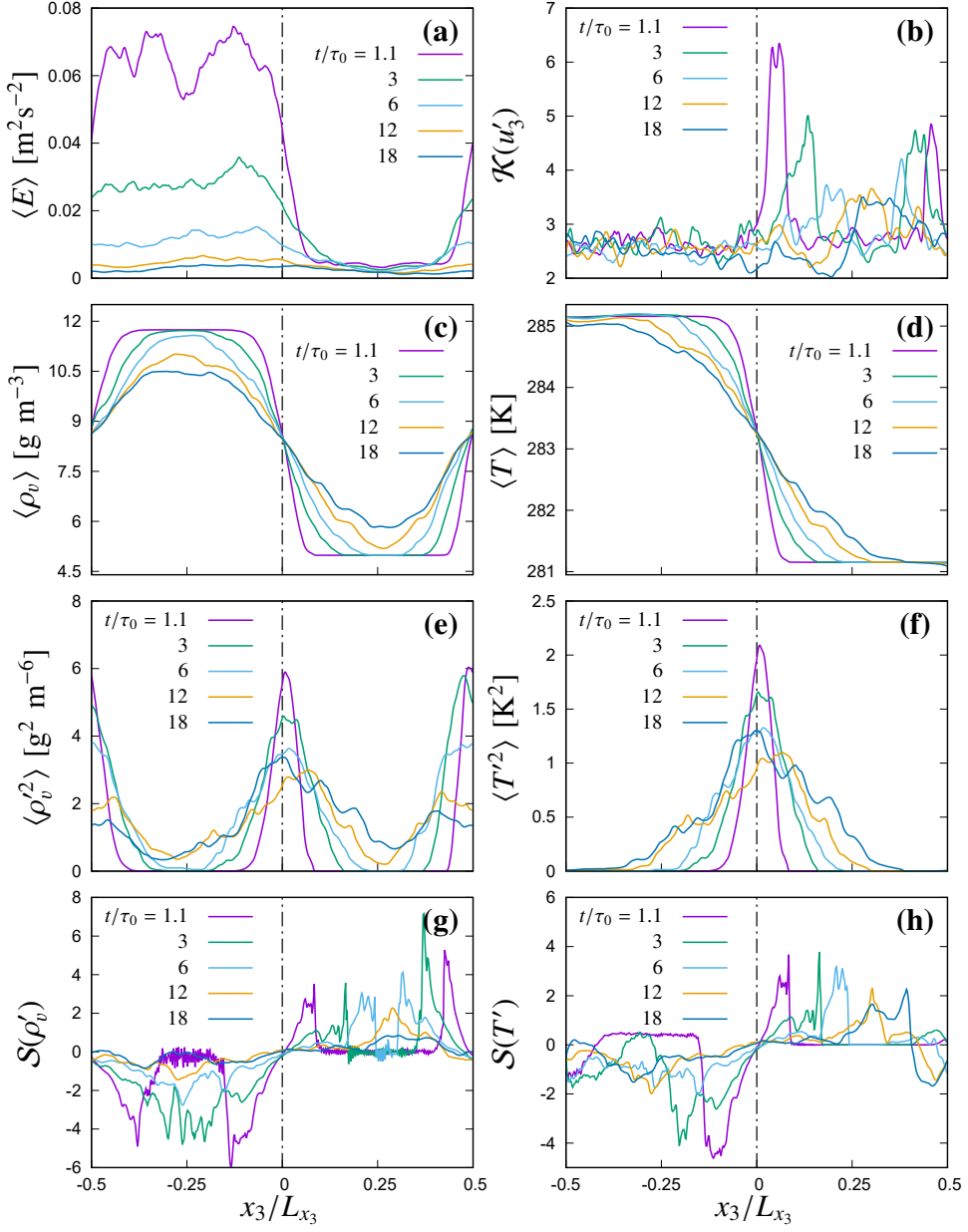
Figure 2.4: Transient evolution of flow statistics:(a) TKE $\langle E \rangle$; (b) kurtosis of vertical velocity fluctuations $K(u_3')$; (c) mean water vapor density $\langle \rho_v \rangle$; (d) mean temperature $\langle T \rangle$; (e) variance of water vapor fluctuations $\langle \rho_v'^2 \rangle$; (f) variance of temperature fluctuations $\langle T'^2 \rangle$; (g) skewness of water vapor fluctuations $S(\rho_v')$; and (h) skewness of temperature fluctuations $S(T')$ evolution. All plots present horizontal plane averaged quantities as in Figure 2.1(c) and (d). The presented data are from simulation **R25**. Differences are small among the three simulations.
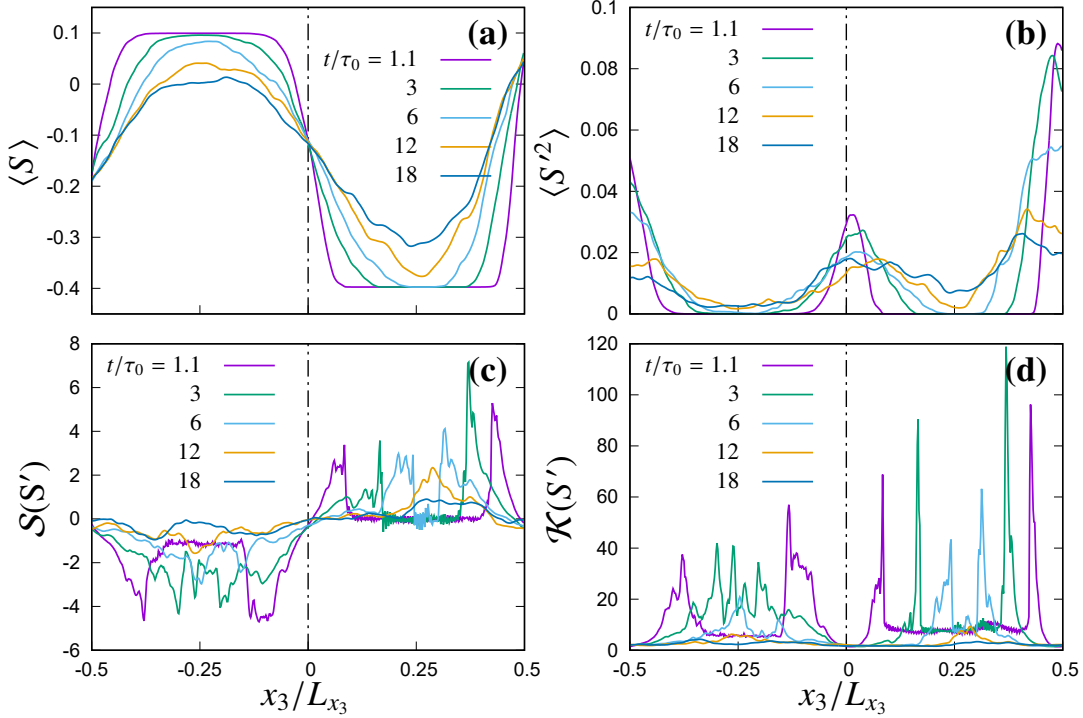
Figure 2.5: Transient evolution of supersaturation:(a) mean of supersaturation $\langle S \rangle$; (b) variance $\langle S'^2 \rangle$; (c) skewness $S(S')$; and (d) kurtosis $K(S')$ of supersaturation fluctuations. All plots present horizontal plane averaged quantities.

turbulence develops from the initial random quantities. Since all the three different simulations were initialized with the same initial background fluid flow conditions, similar transient evolutions are observed for various fluid turbulent quantities. In transient evolution of $\langle E \rangle$ in Figure 2.4(a), a detrainment of the TKE to the clear air region of the domain can be observed which happen through the initial interface (dotted line in the middle). Some detrainment also happen through the top boundary on top of the clear air region of the domain due to periodic boundary condition, which generates a secondary inhomogeneous layer. Detrainment of the TKE and the widening of the TKE interface towards the clear air region of the domain can be recognized by following the positions of the peaks in the kurtosis for the vertical component of the fluid velocity u_3 in the Figure 2.4(b). These peaks move toward the core of the clear air region. Skewness $S(\cdot) = \langle (\cdot)^3 \rangle / \langle (\cdot)^2 \rangle^{3/2}$ and kurtosis $K(\cdot) = \langle (\cdot)^4 \rangle / \langle (\cdot)^2 \rangle^2$ of the fluid quantities are computed using the horizontal plane averages $\langle \cdot \rangle$, and expressed as a function of vertical direction x_3. Large values for the skewness and kurtosis indicate heavy-tailed distributions of the fluctuating quantities, which can be observed at the interface region as a result of the anisotropic mixing in between the cloudy and clear air regions of the

domain, driven by the initial TKE gradient. After 6 initial eddy turnover time ($t/\tau_0 = 6$), the overall TKE and the amplitude of the kurtosis peaks are observed to become significantly small, indicating a quasi-homogenized condition. During the final stage of the simulation ($t/\tau_0 = 18$), it can be seen that a negligible amount of TKE is left inside the fluid motion. The smaller peaks of the kurtosis represent a well mixed stage in the distribution of the rms of the velocity fluctuations throughout the domain. Decay rate in the kinetic energy at this stage is reduced by the production of buoyancy inside the mixing layer. The unstably stratified temperature profile in the vertical direction amplifies the vertical motion further (see also Gallana et al. (2014) [40]), and the fluctuations of ρ_v and T produce buoyancy fluctuations (equation (2.5)). Both these physical processes introduce energy into the vertical motion (equation (2.2)). This cumulative effect becomes visible only after $t/\tau_0 = 6$ (see the growth of $\langle E \rangle$ in the mixing region in Figure 2.4(a)), when the flow has lost most of its initial turbulent kinetic energy. This additional source of kinetic energy accelerates the growth of the mixing layer, and reduces the extent of the undiluted regions as well. During the later stage of the evolution, $t/\tau_0 > 12$, the initial configuration of two different regions is almost no more distinct, and the flow begins to approach a homogenized state.

Figure 2.4(c) and (d) present the time evolution of the mean of the water vapor density $\langle \rho_v \rangle$ and the temperature $\langle T \rangle$ respectively. Mean of both the density of water vapor and the temperature decrease inside the cloudy region of the domain, whereas, it increase inside the clear air region. The resulting profile of mean supersaturation $\langle S \rangle$ (which is initialized with a magnitude of 10% inside the cloudy region and -40% inside the clear air region) shows a decrease in its magnitude inside the supersaturated cloudy region and an increase inside the subsaturated clear air region (Figure 2.5(a)). The mixing process tends to homogenize and produce a uniform supersaturation profile. Therefore, the mean supersaturation value remains positive ($\langle S \rangle > 0$) only in the central part of the cloudy region during the final stage ($t/\tau_0 = 18$). Whereas, most of the domain remains subsaturated ($\langle S \rangle < 0$). Figure 2.4(e) and (f) present the time evolution of the variance of water vapor fluctuations $\langle \rho_v'^2 \rangle$ and the temperature fluctuations $\langle T'^2 \rangle$. Variance in the plane averaged supersaturation fluctuations $\langle S'^2 \rangle$ as a result of the water vapor density fluctuation and the temperature fluctuation is shown in Figure 2.5(b). Although in the initial condition, no fluctuations are introduced for the temperature and the density of water vapor fields, fluctuations are actually generated by the mixing in the interface region, which propagated inside the undiluted core of the cloudy or the clear air region gradually during the spreading of the mixing region. There is also a minor source for the fluctuations in the fluid flow quantities, in form of the droplet feedback term C_d in equations (2.3) and (2.4). However, since the mean condensational time-scale is much larger than the initial eddy turnover time-scale, C_d could only give an overall small contribution for generating the fluctuations. In Figure 2.4(e) and 2.5(b), two peaks are observed in the fluctuations of the density of water vapor

and supersaturation, one of which is in the interface in the middle of the domain, and other one is near the bottom and the top boundaries, due to periodicity in the initial density of water vapor condition. However, the initial temperature is non-periodic in the vertical direction, and varies only at the mixing interface in the middle of the domain. Therefore, Figure 2.4(f) shows only one peak in the variance of the temperature fluctuations. Temporal growth of the scalar (density of water vapor, temperature, and supersaturation) mixing layers, and the widening of the scalar interfaces become evident from the shift in the peaks of the skewness and the kurtosis of the scalars towards the undiluted central regions as shown in Figure 2.4(g and h), and Figure 2.5(c and d), which gradually decrease in magnitude with the mixing spreading all across the domain.

Figure 2.6 presents the time evolution of one dimensional (1D) horizontal/ transversal (x_1, x_2) spectrum of the three components of air velocity $E_{u'_1}(k)$, $E_{u'_2}(k)$ and $E_{u'_3}(k)$ in the wavenumber space k, sampled at the middle horizontal plane of the initial configuration of the cloudy region, and at the middle plane of the initial interface region (with 3 adjacent plane averaging in both cases). The 1D spectra in wavenumber space $E_{u'_1}(k)$, $E_{u'_2}(k)$ and $E_{u'_3}(k)$ distributed in the homogeneous x_1, x_2 directions are computed as:

$$E_{u'_1}(k) = \frac{1}{N_2} \sum_{j=0}^{N_2-1} \mid \hat{u}_1(x_1^j, k, x_3) \mid^2;$$

$$E_{u'_2}(k) = \frac{1}{N_1} \sum_{j=0}^{N_1-1} \mid \hat{u}_2(k, x_2^j, x_3) \mid^2;$$

$$E_{u'_3}(k) = \frac{1}{2} \left[\frac{1}{N_1} \sum_{j=0}^{N_1-1} \mid \hat{u'_3}(k, x_2^j, x_3) \mid^2 + \frac{1}{N_2} \sum_{j=0}^{N_2-1} \mid \hat{u'_3}(x_1^j, k, x_3) \mid^2 \right]$$

where N_i is the number of grid points in x_i direction, $\hat{f}$ is the Fourier transform of quantity f. Initially the cloudy and the clear air region were initialized with two homogeneous and isotropic turbulent cubic domains [64] with a TKE ratio of 20 in between the two regions. Therefore, the initial 1D transversal spectra for all the three components of velocity fluctuations look almost similar (some differences can be observed in the lowest wavenumbers due to the smaller number of samples). The interface region in the initial condition, however, contains lower TKE than that of the cloudy region of the domain, which is due to the linear interpolation in TKE magnitudes in between the cloudy and the clear air region. This can also be observed in the initial TKE spectra of the interface region showing a vertical shift downwards than that of the cloud core region. With time advancement, the dissipative wavenumber range from the initial condition shows transition towards smaller wavenumbers indicating a growth in the Kolmogorov micro-scale η with time, while, at the same time gradually shrinking the inertial sub-range. Moreover,
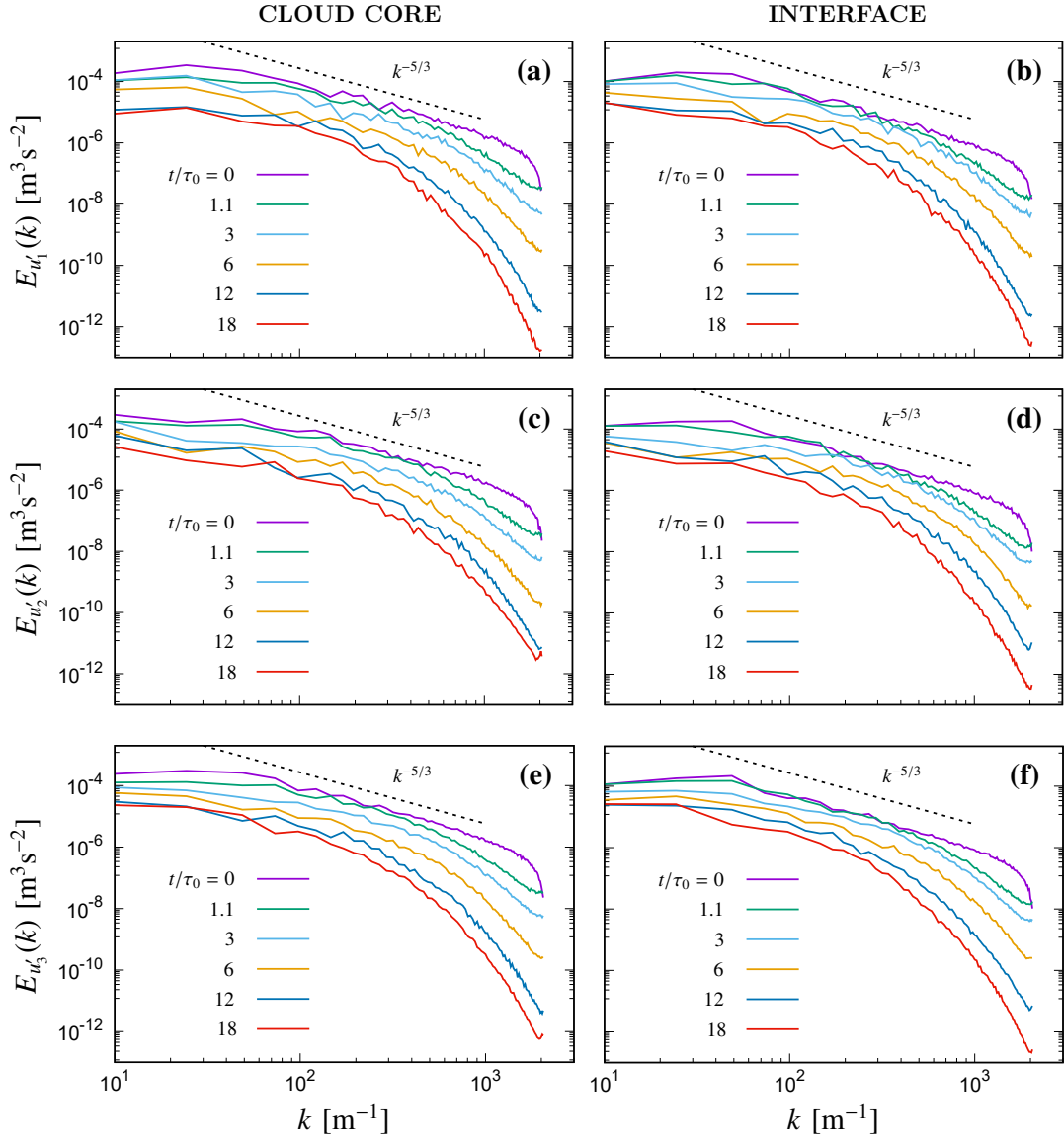
Figure 2.6: One dimensional horizontal spectra for Energy: Transient evolution of (a, b) the transversal spectra of u_1'; (c, d) the transversal spectra of u_2'; and (e, f) the transversal spectra of u_3' respectively at the cloud core and at the interface. All plots correspond to one dimensional spectrum calculated at the middle plane of the initial cloudy region of the domain and the initial interface mixing layer.

the spectra of different components of velocity fluctuations, the horizontal panels in Figure 2.6, do not replicate each other during the later instances of the simulation, resembling an anisotropic evolution of the fluid flow.

In Figure 2.7(a and b), the transient evolution of the water vapor density fluctuations spectra $E_{\rho_v'}(k)$ and in Figure 2.7(c and d), the temperature fluctuations
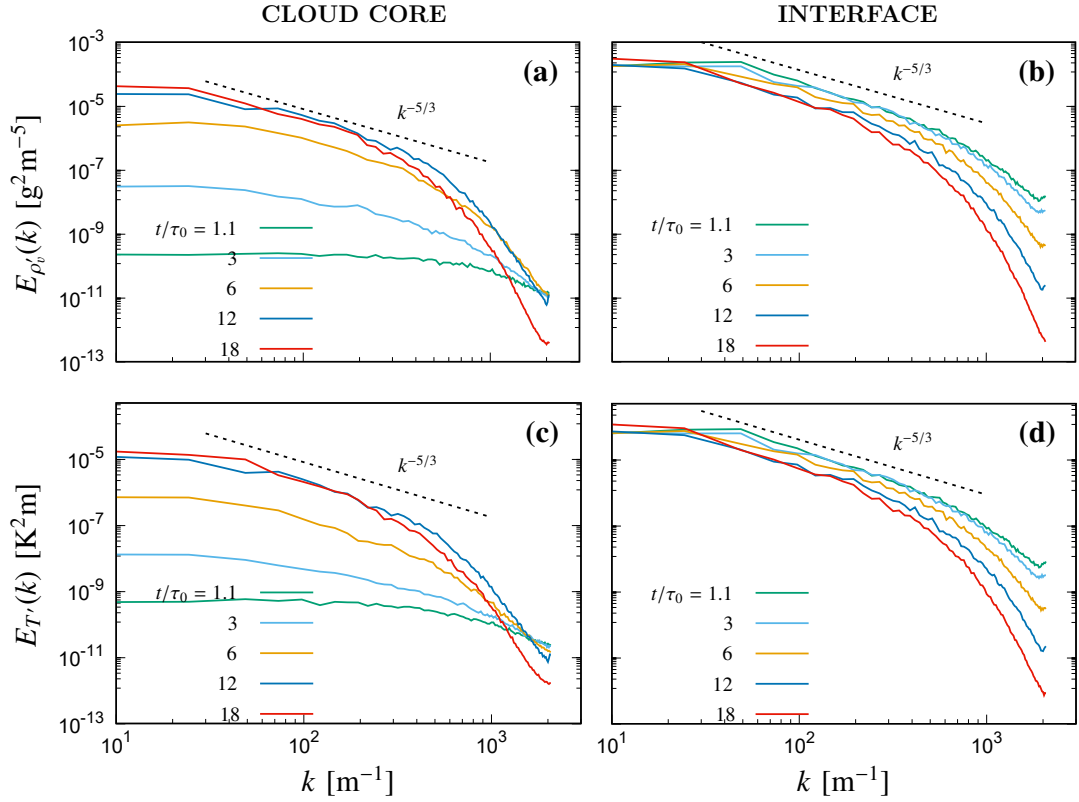
Figure 2.7: One dimensional horizontal spectra for Scalars: Transient evolution of the spectra of (a, b) the water vapor fluctuations ρ'_v; and (c, d) the temperature fluctuations T' respectively at cloud core and at the interface. All plots correspond to one dimensional spectrum calculated at the middle plane of the initial cloudy region of the domain and the initial interface mixing layer.

spectra $E_{T'}(k)$ in wavenumber space k are presented, which are sampled both at the cloud core and at the interface. Presence of a mean gradient in the initial scalar profiles along the vertical direction creates a large variance of that scalar in the mixing layer (Figure 2.4), which is observed to spread towards the undiluted core regions with time. The mean gradient in the mixing region is large enough to produce sufficient variance in the scalars to counter its dissipation and the turbulent transport. Therefore, a well mixed region can be observed to be created inside the scalar spectrum which is quickly approaching the $k^{-5/3}$ Kolmogorov inertial range [62]. Initially the only source of temperature and density of water vapor variance inside the undiluted cloudy region is the droplet condensation/evaporation. Therefore, it can be seen that initially the scalar spectra are not well developed. But after $t/\tau_0 = 10$, the growth of the mixing layer gradually destroys the cloudy core region, so that, similar scalar spectra like the mixing region is replicated inside the

cloud core as well. The equations used for computation of the scalar spectra are:

$$E_{\rho_v'}(k) = \frac{1}{2}\left[\frac{1}{N_1}\sum_{j=0}^{N_1-1} \mid \hat{\rho}_v'(k, x_2^j, x_3) \mid^2 + \frac{1}{N_2}\sum_{j=0}^{N_2-1} \mid \hat{\rho}_v'(x_1^j, k, x_3) \mid^2\right]$$

$$E_{T'}(k) = \frac{1}{2}\left[\frac{1}{N_1}\sum_{j=0}^{N_1-1} \mid \hat{T}'(k, x_2^j, x_3) \mid^2 + \frac{1}{N_2}\sum_{j=0}^{N_2-1} \mid \hat{T}'(x_1^j, k, x_3) \mid^2\right]$$

where $\hat{\rho}_v'$ and $\hat{T}'$ are the Fourier transform of ρ_v' and T' respectively. Since in the initial condition, no fluctuations are introduced in the scalar quantities, spectra for the initial conditions are not shown.

2.3.2 Transient Evolution of the Droplet Population

The three simulations of this study are initialized with three different mono-disperse cloud droplet populations listed in Table 2.2 in the same fluid flow initial conditions. The droplet populations go through distinct transient evolution according to their individual surrounding fluid flow conditions. In general, the droplets in the cloud core region experience an average condensational growth due to its supersaturated ambient condition. However, the droplets which are exiting the cloud core region, tend to evaporate due as a result of subsaturated ambient. A visualization of the flow along with droplets is shown in Figure 2.8, where enstrophy ($E = |\nabla \times \mathbf{u}|^2$) of the fluid field across a vertical plane (plane (x_3, x_1)) is presented together with the superposition of the cloud droplets around that plane. The thickness of the droplets containing slice is 0.0025 m, and the visualization is produced after 6 initial eddy ($t/\tau_0 = 6$) turnover time. Also, the regions of supersaturation S field is marked in the red and yellow contour lines. The line at $S = 0$ marks the extent of the cloudy region, where condensational growth occurs. In the region with $S \leq -0.2$ beyond the yellow contour line, the droplets would instead experience a quick evaporation. Although the enstrophy field looks almost similar, some small differences in the local enstrophy can be observed which is as a consequences of the cloud droplet feedback term C_d in equations (2.3) and (2.4). As a result, these terms determine also the buoyancy term B in the momentum balance equation (2.2). Since the buoyancy is sensitive to the small local fluctuations in the density of the water vapor ρ_v and the temperature T, differences in droplet feedback C_d due to different droplet sizes (equation (2.6)) can result into small differences in the local fluid velocity, despite the initial fluid flow conditions for the three simulations are identical. Distribution of enstrophy in Figure 2.8 gradually decreases with the time, in line with the TKE distribution also decreased as shown in Figure 2.3(a) and Figure 2.4(a). For visualization of the droplets in Figure 2.8, the droplets are normalized with their initial size r_{in} (initially normalized size of the droplets are uniform and equal to 1), and presented as variable size points accounting for the
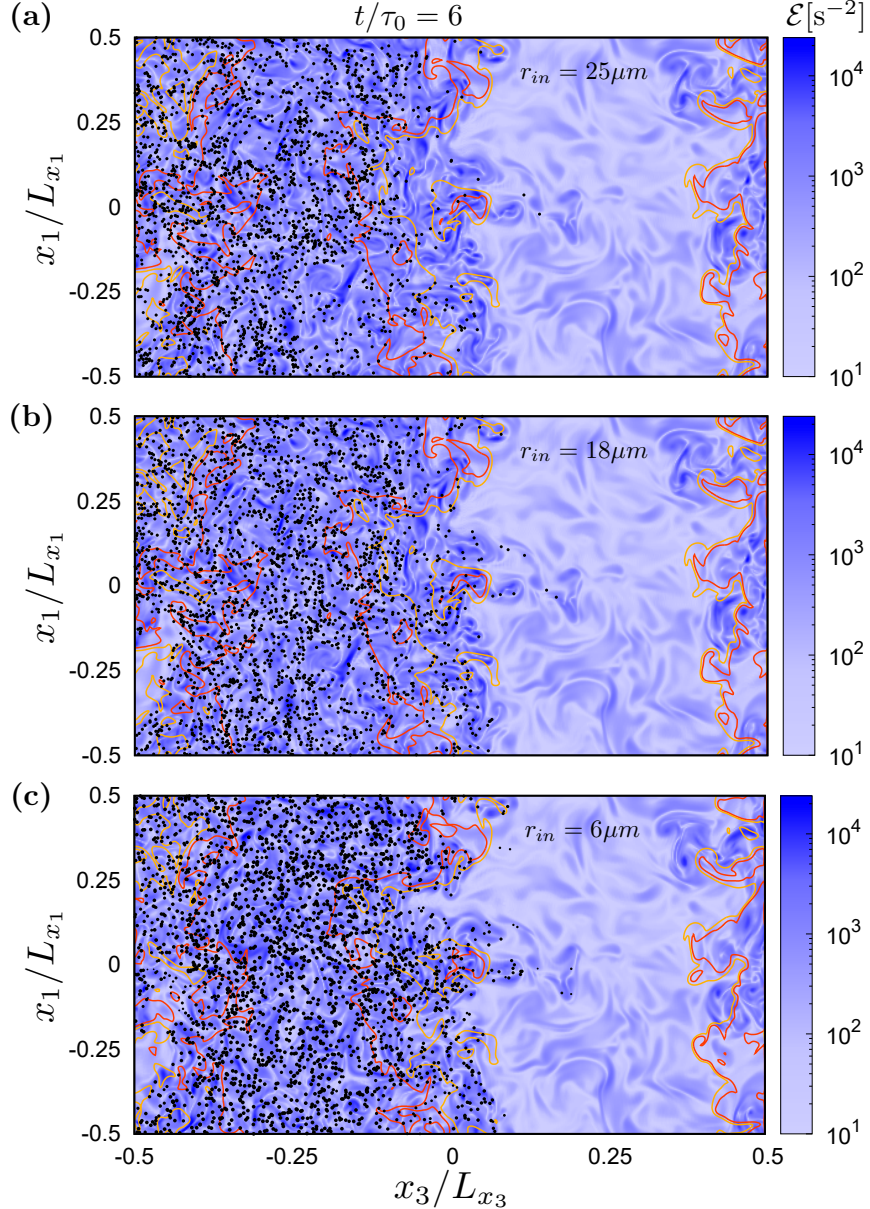
Figure 2.8: Visualization: Enstrophy E field across a vertical plane (plane (x_3, x_1)) is presented in superposition with the supersaturation S field in contour lines and cloud droplets around that plane (thickness of droplets containing slice is 0.0025 m) after 6 initial eddy ($t/\tau_0 = 6$) turnover time. Colorbar represents magnitude of the enstrophy in the flow field, red and yellow contour lines represent saturated ($S = 0$) and subsaturated ($S = -0.2$) conditions respectively. The sizes of the droplets are proportional to r/r_{in} for each population. The panels show the simulations with the droplet populations of (a) 25 μm; (b) 18 μm; and (c) 6 μm initial radius.

growth or the reduction in droplet size due to physical processes, such as, condensation or evaporation or collision. Due to much higher condensational growth rate of the smaller size (6 μm radius) droplet population, the normalized size of the presented droplets are bigger in Figure 2.8(c) than the other two populations in Figure 2.8(a and b). Since the time lapse of the presented data in this figure is small compared to the total simulation duration, the cloud droplets do not show wide range of size distribution, but rather stay close to their initial radius.

Due to differences in the cloud droplet Stokes number *St* as shown in Figure 2.3(d), droplets show different responses to the local enstrophy field. In Figure 2.8(a), the droplets of initial 25 μm mono-disperse distribution are seen to preferentially concentrate away from the regions of higher enstrophy. These population is often forming string like patterns and clustering in the areas of lower enstrophy [158]. However, the gradual reduction in the average Stokes number with time reduces this tendency to cluster. While the gravitational settling which is dominant on the larger droplet population and the droplet size broadening reduce the correlation between the droplet concentration and the local strain. A similar, but much milder tendency can also be observed in Figure 2.8(b) for the simulation with initial 18 μm mono-disperse droplet population. On contrary, a higher uniform concentration can be seen in Figure 2.8(c) for the droplet population with initial 6 μm radius, which are not significantly influenced by the local enstrophy and gravity due to almost tracer like behavior.

At the same time, the droplets also undergo gravitational sedimentation according to their individual mass. This settlement is only partially counterbalanced by the turbulence. The relative importance of sedimentation is controlled by the dimensionless settling parameter S_v [147]. Since u_η decays as $t^{-(n+1)/4}, n = 1.25$ in these present simulations, the importance of gravitational sedimentation grows with time (see Figure 2.3(d)). Larger droplets of initial 25 μm radius population begin to gather at the bottom of the domain from the very beginning of the simulation, and are observed to rarely enter the mixing layer (Figure 2.8(a)). Droplets with initial 18 μm radii have a comparatively slower rate of sedimentation, and are observed to cross the cloudy region border through the detrainment process (Figure 2.8(b)). While, on the contrary, smaller droplets (initial 6 μm radius population) do not show a noticeable rate of sedimentation. They are observed to easily detrain in the clear air zone (Figure 2.8(c)), where, due to their shorter evaporation time-scale (proportional to $r^2/|S|$) and much longer residence time (roughly proportional to L/u', but can be modified by the droplet settling velocity v_p), they can completely evaporate. Moreover, for the smaller droplet population, the presence of a strong subsaturation near the bottom boundary and at the clear air region of the domain also removed droplets by a complete evaporation of the droplet liquid water content. This evaporation contributes to cool down the subsaturated layer above the mixing region, and increases the negative buoyancy [89] and thus enhancing the mixing process. Whereas, for the larger droplets, after a few initial time-scales, this

process of detrainment to subsaturated clear air zone and complete evaporation of
the droplets can not be witnessed.
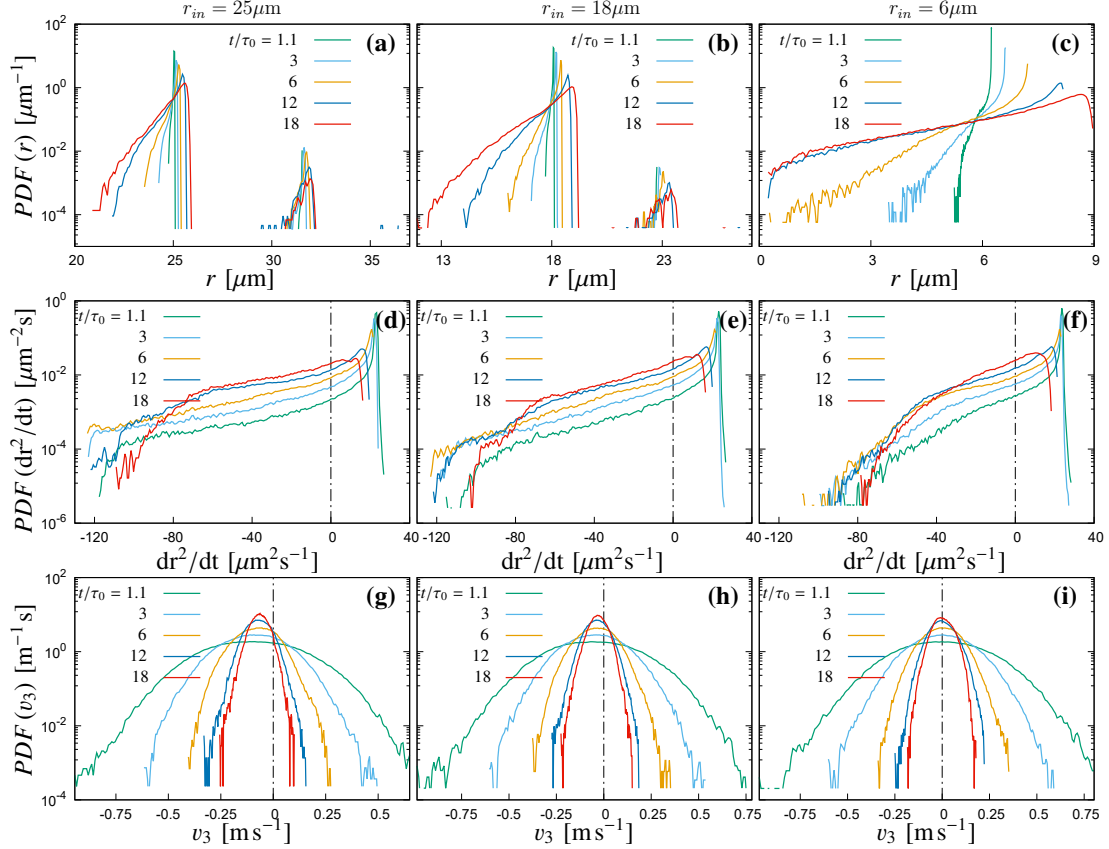
Figure 2.9: Probability density functions (PDFs): PDFs of (a, b, c) cloud droplet
radius r; (d, e, f) droplet surface area growth rate dr^2/dt; and (g, h, i) vertical
component of droplet velocity v_3 for 25 μm, 18 μm, and 6 μm initial droplet size
populations respectively.

The above-mentioned distinctive behaviors are reflected in the transient evo-
lution of the normalized probability density functions (PDFs) of the droplet size,
velocity, and growth rate. These are presented in Figure 2.9. Figure 2.9(a-c) present
the evolution of the PDFs for the cloud droplet radius with time. Both the cloud
droplet populations with initial 25 and 18 μm radius show limited broadening of
their sizes due to lesser impact of the condensation/evaporation on these popu-
lations. However, the presence of two secondary peaks, which correspond to the
collisions (Figure 2.9(a and b)), result in droplet size broadening. However, for the
droplet population with initial 6 μm radius, no collisional growth can be observed
for the simulation duration. Whereas, the width of the DSD is observed to be wider

in Figure 2.9(c) due to both the evaporation and condensation processes, and a certain number of droplets are observed to evaporate completely. The impact of the condensational size growth or the evaporative size reduction is more efficient for the smaller droplets, since the droplet radius growth rate dr_i/dt is proportional to r_i^{-1} (see equation (2.9)). The PDFs of dr_i^2/dt, which indicates the growth rate in the droplet surface area, are presented in Figure 2.9(d-f). As dr_i^2/dt from the equation (2.9) is proportional to the local supersaturation $S = (\varphi - 1)$ conditions, the simulations of the three initial mono-disperse cloud population should exhibit similar transient evolution, since the background supersaturation spatial distribution is similar for the three simulations. However, droplets experience different supersaturation conditions due to their different trajectories, which also depends on their individual sizes and the local fluid flow conditions. Smaller droplets of the initial 6 μm radius do not show the extreme negative tail of dr_i^2/dt as observed for larger droplets in Figure 2.9(d and e). This is because of the complete evaporation of the droplets from the smaller 6 μm radius population (Figure 2.9(f)). Moreover, since the subsaturation can result in highly negative dr_i/dt for the sub-micron droplets from the initial 6 μm droplet population, and since the numerical time-step for the sub-micron droplets needs to be very small and their microphysics cannot be modelled using equation (2.9); the droplets with sizes below 4% (≤ 0.24 μm) are removed, which is also detailed in the initial setup for the droplets subsection.

Due to the gravity, the vertical component of the cloud droplet velocity v_3 exhibits different behaviour compared to the velocity components along the horizontal directions v_1 and v_2. Transient evolution of PDFs for v_3 is plotted in Figure 2.9(g-i). During the early stage of evolution, the PDFs of v_3 shows wider distribution due to the presence of TKE inside the domain, which influences the droplet velocity as well. However, the decay of TKE with time narrows down the spectrum of u_3, and therefore the v_3 with time. The gravitational settling is visible in the shift of the maxima of the PDFs of v_3 toward the negative values for the larger droplets. It was previously observed in Figure 2.8(a) that the cloud droplets of initial 25 μm population are positioned near the bottom boundary of the domain due to the gravitational acceleration. From Figure 2.9(g), most of the cloud droplets of initial 25 μm population are observed to have a higher negative v_3 during the later instances of the simulation. Free fall velocity for a 25 μm cloud water droplet is 0.077 m/s. The peak of the PDF of v_3 of this population is observed at 0.063 m/s after the first time-scale, which is implying dominance of gravitational settlement with velocities close to the free fall condition. Simulation with the initial 18 μm population (Figure 2.9(h), and 2.8(b)) evidences comparatively a slower rate of settling down than the initial 25 μm population. However, the simulation with initial 6 μm population shows almost a symmetric evolution of v_3 around the zero (Figure 2.9(i)), which indicates the negligible effect of the gravitational acceleration on this cloud droplet population.

The number density of the droplets inside the simulation domain can change
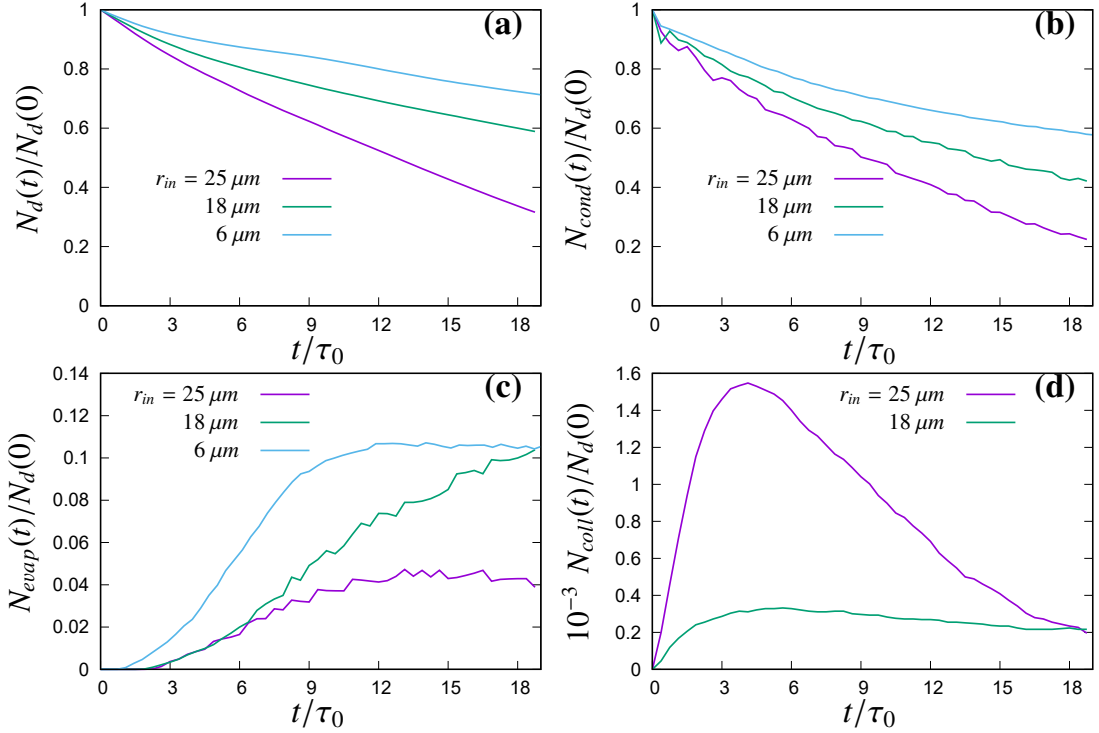
Figure 2.10: Normalized number density of droplets: Transient evolution in (a) the number density of total number of cloud droplets $N_d(t)$; (b) the number density of droplets went through condensational growth $N_{cond}(t)$; (c) the number density of droplets undergone evaporative size reduction $N_{evap}(t)$; and (d) the number density of droplets with one collision $N_{coll}(t)$ as observed for 25 μm, 18 μm, and 6 μm initial droplet size populations. No collision and coalescence is observed for 6 μm initial droplet populations.

with time due to collisions, or due to complete evaporation of the liquid water, or due to the gravitational sedimentation of the droplet out of the domain bottom boundary. To quantify the relative importance of condensation, evaporation, collision and gravitational sedimentation; the transient evolution in the number density of droplets is presented in Figure 2.10. Evolution in number density of all droplets $N_d(t)$, which is normalized by initial droplet number density $N_d(0)$, is presented in Figure 2.10(a). Here most significant reduction in total number of droplets can be observed for the initial 25 μm droplet population, and comparatively less for the initial 18 μm droplet population, and much lesser for the initial 6 μm droplet population. The most active physical process to result in reduction of the total number of cloud droplets for the initial 25 and 18 μm droplet populations is the gravitational settling and the subsequent removal of the droplets falling below the bottom boundary of the domain. However, the most active physical process for the initial

6 μm droplet population, reducing the total number of droplets is its complete evaporation in the subsaturated region of the domain. In Figure 2.10(b), the time evolution in the normalized number density of the droplet population remaining to its initial radius or exhibiting a size growth due to condensational water vapor deposition $N_{cond}(t)/N_d(0)$ is presented. $r_{in} \leq r_i < \sqrt[3]{2}r_{in}$, where $\sqrt[3]{2}r_{in}$ correspond to radius of a droplet after first collision with a similar sized droplet. Although, the initial 6 μm droplet population did not exhibit any collisional growth, but some fraction of the population grew more than $\sqrt[3]{2}r_{in}$ size due to the much higher degree of condensational growth than the larger populations. Transient evolution in the normalized number density of the cloud droplets experiencing evaporative size reduction $N_{evap}(t)/N_d(0)$ is presented in Figure 2.10(c). For the initial 25 μm droplet population, droplets with a radius smaller or equal to 24.5 μm are considered for counting the number density of the evaporating droplets. $r_i \leq 17.5$ μm for the initial 18 μm population and $r_i \leq 5.5$ μm for the initial 6 μm population. The effect of the complete evaporation for the initial 6 μm droplet population is evident from Figure 2.10(b) where the number density of the droplets equal or larger than the initial 6 μm size is observed to decrease with time. But in the Figure 2.10(c), the number density of the evaporating droplets during the later stage of the simulation is almost steady. This implies that some physical process is resulting in removal of droplets in the evaporating range. In Figure 2.9(c), the absence of sub-micron droplets is seen to happen from 12 to 18 initial eddy turnover time, which also confirms presence of the complete evaporation of sub-micron droplets for initial 6 μm droplet population. The initial 25 and 18 μm droplet population shows a growth in the DSD due to the occurrence of collision in different size ranges. Figure 2.10(d) presents normalized number density of the droplets in size ranges corresponding to collision between two similar sized droplets $N_{coll}(t)/N_d(0)$, which is the secondary peaks in Figure 2.9(a and b). For this transient evolution of the number density of colliding droplets, the source is the occurrence of collisions, and the sink is the gravitational sedimentation of the droplets out of the domain. For both the initial 25 and 18 μm droplet population in Figure 2.10(d), during the initial 4 initial eddy turnover time, the occurrence of collision dominates over the gravitational sedimentation. However, later the droplets with 1 collision for 25 μm initial droplet population are removed from the domain very rapidly, whereas, for the 18 μm initial droplet population, the number of droplets with 1 collision remains almost steady. Occurrence of collision in between larger sized droplets, which already have one collision, to the smaller droplets resulting in droplets with two or more collisions were very rare, and happened mostly in the case of 25 μm initial droplet population.

Time evolution of the one-point correlations between fluid flow and cloud droplet $B(a,b) = \langle a'b' \rangle / (\langle a'^2 \rangle \langle b'^2 \rangle)^{1/2}$, where a and b are respectively the fluid and the droplet quantities, are presented in Figure 2.11. Since the droplet distribution is not uniform, for the calculation of these correlation parameters, both the fluctuations in the cloud droplets and fluid flow quantities are plane averaged in horizontal

35
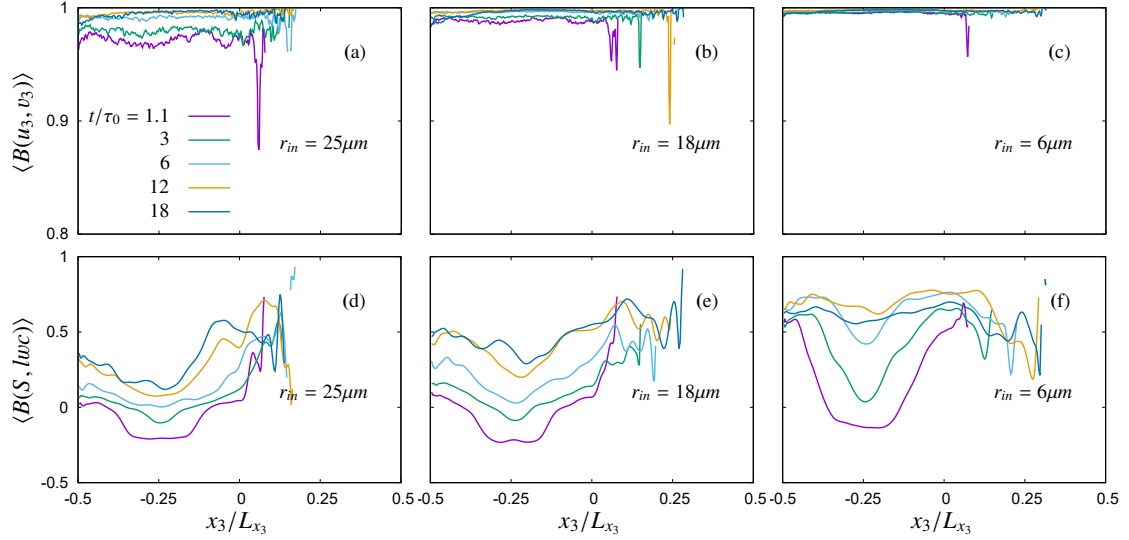
Figure 2.11: Correlation between fluid and droplet:(a, b, c) correlation between vertical component of fluid velocity fluctuations u_3' and droplet velocity fluctuations v_3' ; and (d, e, f) between supersaturation fluctuations S' and fluctuations in liquid water content lwc'. Vertical panels from the left to right present correlation diagrams for 25 μm, 18 μm, and 6 μm initial droplet size populations respectively.

directions (x_1, x_2). This is done by considering only grid cells containing cloud droplets withing its Δx^3 volume and the droplet quantities are averaged to the corresponding grid points. In the correlation between the fluctuations in the vertical component of the fluid velocity u_3' and the droplet velocity v_3' in Figure 2.11(a-c), u_3' and v_3' are very well correlated for initial 6 μm droplet population, but less correlated for 18 μm, and much lesser for the 25 μm initial droplet population during the initial instances. Spurious fluctuations in the correlation parameters are observed in the interface region, where number of droplet samples are much smaller. Since the TKE inside the domain during later instances was much smaller, and the Stokes numbers decrease (Figure 2.3(d)) as well for all the populations, the velocity fluctuations for both the fluid u_3' and the droplet v_3' tend to correlate more with the time advancement. In Figure 2.11(d-f), the correlation between the supersaturation fluctuations S' and the fluctuations in the liquid water content lwc' is presented. Due to the particle clustering and the high fluctuations in the size of the statistical samples, bezier smoothing has been applied to the correlation in between S' and lwc'. This smoothing significantly modifies the data only in the clear air region of the domain, where number of droplets are very small. Improved statistics could be obtained by considering ensemble averaging between different simulations with independent initial conditions. Since initially inside the undiluted cloudy part of the domain, S' was 0, and gradually the fluctuations picked up, the widening of the interface mixing region can be witnessed in these correlation plots. With positive

S', the positive lwc' is observed, which shows highest positive correlation for initial 6 μm droplet population. However, the correlation is less for 18 μm, and much lesser for the 25 μm initial droplet population. In general, almost no correlation is observed in between the fluid enstrophy E' and the vertical component of the droplet velocity v'_3. However, for the two larger cloud droplet populations (initial 25 and 18 μm radii), increase in the negative correlation was observed to happen with time.

In Figure 2.12, time evolution of three sample droplets from the three different simulations reaching a specific region in the initial clear air portion of the domain (see the box in the clear air region of panel (a), (c), (e) of Figure 2.12) after the 3 initial eddy turnover time ($t/\tau_0 = 3$) is presented. These droplets were transported due to the detrainment of the cloudy air to the subsaturated clear air region from the near interface region of the cloudy part of the domain. Due to subsaturation, only the droplets from the simulations with initial 25 and 18 μm droplet populations are observed to survive the entire simulation duration. The impact of the gravitational settlement is observed to be very pronounced for the larger droplet population, leading to a short residence time in the subsaturated area. Two out of the three droplets came back to the cloudy supersaturated region of the domain almost immediately, see Figure 2.12(a). Whereas, the other remaining droplet was trapped in some eddy to follow a lateral movement inside the clear air region. In Figure 2.12(b), these droplets are observed not to follow the fluid velocity exactly, but rather shows a negative v_3 indicating stronger influences of the gravitational forces on these droplets. The sample droplets from the simulation with initial 18 μm droplet population shows comparatively less influence under the gravitational forces, and remains entrapped in the eddies inside the clear air region of the domain (Figure 2.12(c)). Therefore the subsaturated ambient of these droplets produces a continuous size reduction (Figure 2.12(d)). Whereas, the local subsaturation played mostly important impact on the samples of the droplets from the simulation with initial 6 μm droplet population. After being detrained to the subsaturated clear air region, these droplets cloud not return back to the saturated cloudy part of the domain due to decay in the TKE inside the domain (Figure 2.12(e)), and eventually were evaporated completely in the middle of the simulation duration (Figure 2.12(f)).

A comparison in between some laboratory experiment by Chandrakar et al. (2016) [19] and combined DSDs from our simulations are presented in Figure 2.13. The normalized DSD in Figure 2.13(a) correspond to the steady state DSD achieved by a constant rate of aerosol injection inside a humid chamber, where the DSDs varied according to the presence of number of droplets inside the chamber. Whereas, in our simulations we follow the transient evolution of three different populations of mono-disperse droplets. Due to the presence of supersaturation fluctuations and mixing, we witnessed a transient growth in the DSD by condensation, evaporation and collision, which varied according to the initial size of the droplet population.
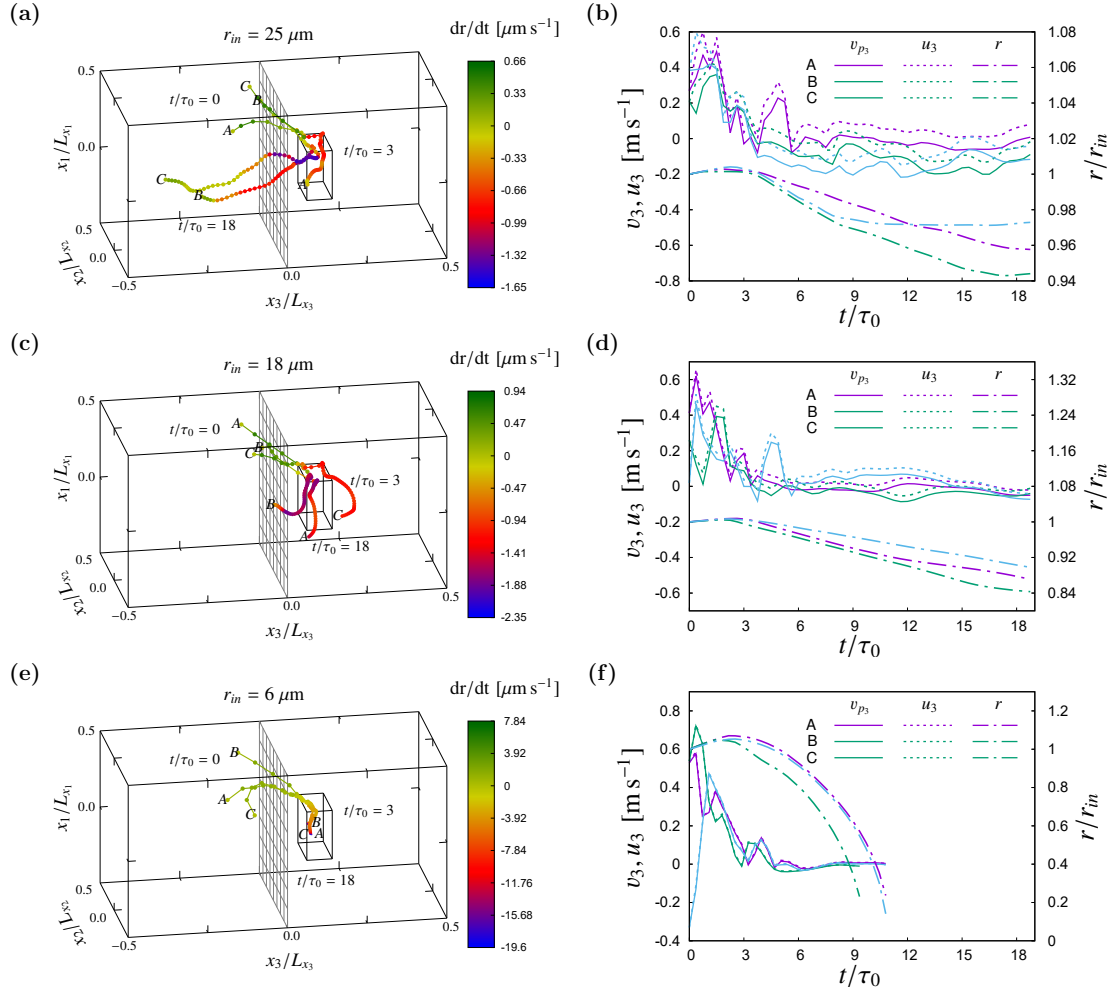
Figure 2.12: Lagrangian trajectories: A sample of few individual cloud droplet trajectories. (a, c, e) Visualization of the time evolution of droplet positions; and (b, d, f) Lagrangian history of the vertical component of droplet velocity v_3, fluid velocity at that droplet position u_3, and their normalized droplet radius r/r_{in} up to the end of simulation duration ($t/\tau_0 = 18$) or to the end of the droplet life till being completely evaporated (panels e and f) are presented. Colorbar for the left panels represents droplet radius growth rate dr/dt, thus indicating the droplet positions where condensation or evaporation occur. Size of the droplets are proportional to normalized droplet radius r/r_{in}.

Due to the simulation setup of initial value problem in our simulations and presence of mixing in between the clear air and the cloudy region of the domain, a steady state condition could not be achieved.
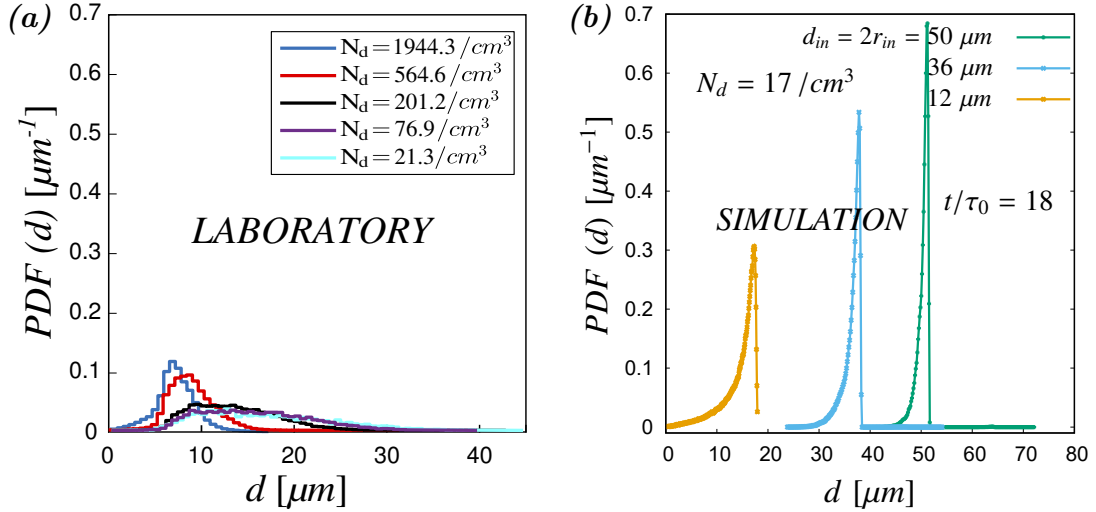
Figure 2.13: Comparison of the probability density functions (PDFs) of droplet size distribution (DSD):(a) PDF of cloud droplets for a laboratory simulation at steady state condition (droplet injection rate=droplet removal rate) [19]; and (b) a combined graph of PDFs of the three simulation runs of this study at the end of the simulation runs.

2.3.3 Impact of Stratification Stability on Cloud Droplets

A series of follow-up simulations are conducted to investigate the impact of the stable, unstable or neutrally stratified airflow conditions on the transient evolution of the initial mono-disperse cloud droplet populations. The simulation domain configuration models the transient inhomogeneous mixing in the cloud top interface, where a volume of the cloudy region and a above-lying volume of clear air region, separated by an initial interface is simulated. Similar to the previous section, the initial airflow conditions for the flow velocity are introduced to be the same for all these 9 simulations as in Table 2.3, with a similar turbulent kinetic energy ratio E_{cloud}/E_{air} of 20 and an initial rms of velocity fluctuations u' inside the cloudy volume to be $0.194\,\mathrm{m\,s^{-1}}$. The sizes of the simulation domains for all these cases are larger compared to the previous simulations. These domains have 512 grid nodes both in the horizontal directions x_1 and x_2, while contains 1024 grid nodes in the vertical x_3 direction. The simulation grid size Δx is $0.001\,\mathrm{m}$, which makes the simulation domain size $L_{x_1} \times L_{x_2} \times L_{x_3}$ equal to $0.512 \times 0.512 \times 1.024\,\mathrm{m^3}$. The initial conditions for the density of the water vapor ρ_v and the temperature T, however, are varied from one simulation to another. These variations in the initial scalar profiles are used to create (a) three different initial stability conditions according to the initial T profiles and to create (b) three different initial supersaturation conditions inside the simulation domains as detailed in Table 2.3.

Table 2.3: Details of the stratified simulation runs

		Quantity	
IDs	Type	RH_{cloud}	RH_{air}
STBL-110-60	Stable	110%	60%
USTBL-110-60	Unstable	110%	60%
NUTRL-110-60	Neutral	110%	60%
STBL-110-40	Stable	110%	40%
USTBL-110-40	Unstable	110%	40%
NUTRL-110-40	Neutral	110%	40%
STBL-105-85	Stable	105%	85%
USTBL-105-85	Unstable	105%	85%
NUTRL-105-85	Neutral	105%	85%

For the stably stratified airflow condition (STBL), a vertical temperature gradient $\Gamma = \Delta T / L_{x_3}$ of $3.82\,\mathrm{K\,m}^{-1}$ is introduced in the three stable stratification simulations. This temperature gradient models a vertically stable stratification profile with a temperature difference of $4\,\mathrm{K}$ in between the cloud and the clear region of the domain, where the cloudy volume is colder than the clear air. In case of the unstably stratified airflow condition (USTBL), the vertical temperature gradient Γ is $-3.82\,\mathrm{K\,m}^{-1}$, which models the cloudy volume to be warmer than the above-lying clear air, and therefore, a unstable stratification condition is created. The neutral stratification simulations (NUTRL) have a vertical temperature gradient $\Gamma = -6.5 \times 10^{-3}\,\mathrm{K\,m}^{-1}$ according to the standard atmospheric lapse rate, where the cloudy region of the simulation domain is modeled to be slightly warmer than the clear air region.

The initial condition for the supersaturation is introduced to create three different supersaturation gradients across the cloud and the clear air interface. The strong supersaturation gradient models initially 10% supersaturation condition (RH_{cloud}=110%) in the cloudy volume, while the clear air volume has initially 60% subsaturation (RH_{air}=40%). The moderate supersaturation gradient has the same 10% initial supersaturation condition in the cloudy volume, but a 40% subsaturation (RH_{air}=60%) in the initial clear air region. The mild supersaturation gradient models the cloudy volume with a 5% supersaturation condition (RH_{cloud}=105%) and the clear air region is 15% subsaturated (RH_{air}=85%). It must be noted that although there are three simulations for each the strong, moderate and the mild supersaturation gradients, the initial condition for the density of the water vapor changes from one simulation to the other. This is due to the change in the initial stratified airflow conditions which changes the respective temperatures of the cloudy and the clear air regions of the domain, and therefore the respective saturated water vapor density which defines the relative humidity conditions.
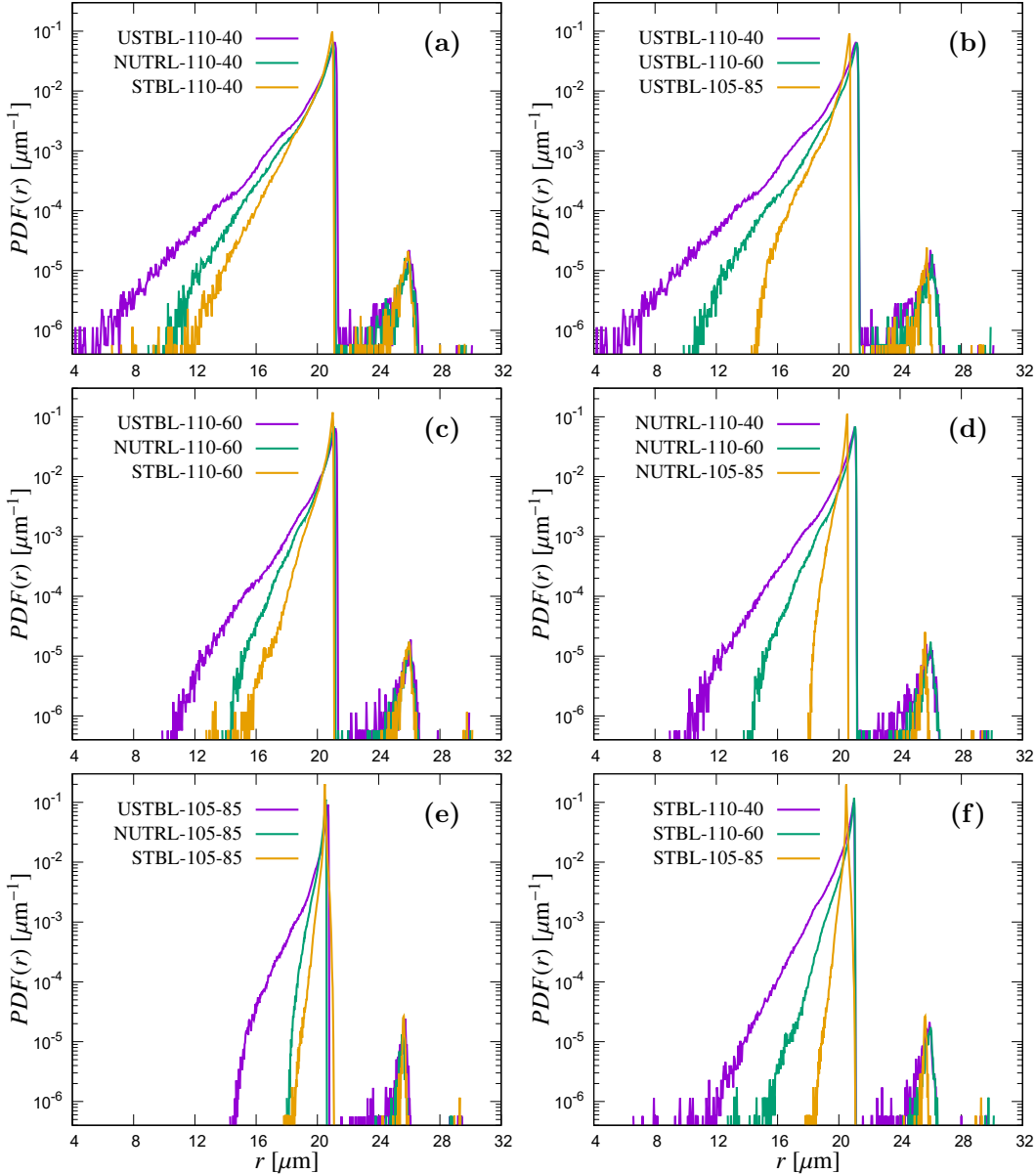
Figure 2.14: PDFs of cloud droplet radius r for various stable (STBL), unstable (USTBL) or neutrally (NUTRL) stratified airflow conditions at the end of the simulation duration $t = 4.536\,\mathrm{s}$ for various initial supersaturation conditions.

The initial conditions for the cloud droplets are the same for all the 9 simulations. A mono-disperse cloud droplet population of initial 20 μm radius is seeded randomly in the initial cloudy volume of the simulation domain for each simulation. The numbers of initial droplets in each simulation are around 3.353×10^6, which have a liquid water content of $0.84\,\mathrm{g\,m^{-3}}$ in the initial cloudy volume of the

41

simulation domain. Such liquid water content can be observed in the atmospheric clouds [131, 65]. All these simulations are conducted for a total duration of $4.536\,\mathrm{s}$, which is achieved with a total of 3.6×10^4 time steps for each simulation with a uniform time step $\Delta t = 1.26 \times 10^{-4}\,\mathrm{s}$. In this section, only the statistics of the cloud droplet population at the end of the simulation duration will be reported, that is, at the transient evolution time of $4.536\,\mathrm{s}$.

Figure 2.14 shows the probability density functions (PDFs) of droplet size distribution (DSD) for the nine simulated cases with various types of stratified airflow and the different initial conditions for the supersaturation across the interface at the end of the simulation duration $t = 4.536\,\mathrm{s}$. In the left panel, Figure 2.14(a,c,e), the nine simulation are organized according to the different initial supersaturation gradient for each plot. Figure 2.14(a) presents the $PDF(r)$ for initially 10% supersaturation condition in the clouds (RH_{cloud}=110%) and 60% subsaturation in the air (RH_{air}=40%) simulations. This is the largest simulated supersaturation gradient. Figure 2.14(c) presents the $PDF(r)$ for initially RH_{cloud}=110% and RH_{air}=60% simulations, which creates a moderate supersaturation gradient across the mixing interface. While the Figure 2.14(e) presents the $PDF(r)$ for initially RH_{cloud}=105% and RH_{air}=85% conditions, which creates a mild supersaturation gradient.

In each plot of this left panel of Figure 2.14, $PDF(r)$ for all the stable, unstable or neutrally stratified airflow conditions are plotted for a specific initial supersaturation condition. It is seen that the unstably stratified airflow condition results in highest widening in the DSD, while the stable condition in the initial temperature profile shows lowest widening in the DSD. As previously mentioned, the unstably stratified temperature profile in the vertical direction amplifies the vertical motion across the initial interface [40], and the resulting fluctuations of ρ_v and T produce buoyancy fluctuations (equation (2.5)) in the gradually widening mixing interface and increase the mixing rate. As a result, both these physical processes introduce energy into the vertical motion (equation (2.2)) and results in higher rate of mixing and supersaturation fluctuations. Therefore, the droplets in the interface region experiences a wide range of supersaturation condition, which is reflected in the wide broadening of the DSD. The stably stratified airflow condition, whereas, inhibits the mixing across the initial interface [40] although there exist a strong gradient in the initial turbulent kinetic energy condition. As a result, DSDs for the stably stratified airflow conditions are the narrowest one. The neutrally stratified airflow condition, on the other hand, shows a moderate DSD broadening in between the limits of the stable and the unstable PDFs of droplet radius, due to its quasi-stable condition. Whereas, concerning the impact of the initial supersaturation gradient, it is clearly seen in the left panel of Figure 2.14, that the strongest gradient would result in higher droplet size broadening, than the moderate and the milder gradients across the initial interface.

It must be noted in the Figure 2.14, that the $PDF(r)$ of the droplets shows both

its evolution 1.) in the gradually widening interface in between the cloudy and the clear air volume which mostly results in evaporative size reduction of the droplets, resulting in the size range below 20 μm and 2.) in the supersaturated cloud core, which is gradually shrinking in size due to the widening of the initial interface, and mostly results in a condensational growth of the cloud droplets as seen in the size range just above 20 μm, before the secondary peaks in the PDFs. These secondary peaks, whereas, represent the droplets which are formed due to collision of two nearly 20 μm radii droplets. These droplets with one collision history also go through 1.) evaporation, if some of them stays in the subsaturated ambient of the interface or gets detrained to the clear air zone, as well as 2.) condensational growth in the cloud core, as can be seen in the PDFs. There are also a few more smaller peaks above a radius of 28 μm, which represent a very small fraction of droplets which have seen 2 collisions.

In contrast to the left panel, the right panel of Figure 2.14 is organized from the top to bottom according to the unstable, then neutral and then stably stratified airflow conditions, while each plot contains the DSDs for different initial supersaturation gradients. As previously described, the highest amount of widening is visible for the unstable stratification case for all the initial supersaturation gradients. While the neutral stratification profile shows a moderate widening in the DSDs and the stable stratification profile results in the narrowest droplet size broadening. Besides the impact of the initial supersaturation gradient, which results in higher amount of broadening in the droplet size, if the supersaturation gradient is higher; one can also observe in Figure 2.14(b,d) that due to the difference in the initial cloudy volume supersaturation condition, the droplets in the cloud core grow bigger for the $RH_{cloud} = 110\%$ cases than the $RH_{cloud} = 105\%$ cases. This phenomenon, however, is different for the stable stratification case in Figure 2.14(e,f) where a fraction of the droplets grows larger with the condensation of water vapor than its size in the unstable or the neutral case for the same initial supersaturation gradient. Since, the stable stratification inhibits mixing, it is most likely that the droplets experience a similar supersaturated ambient longer for the stable case than the neutral or the unstable stratification conditions. One may assume this is the reason. However, quantitatively finding the reason behind the higher sizes of the cloud droplets for the stable stratification condition would need further investigation.

2.4   Summary and Conclusions

In this chapter, the understanding regarding the growth of the inertial cloud droplets in the transient mixing of cloud top horizontal interface is extended by inclusion of the impact of gravitational sedimentation and the impact of collision on the cloud water droplets, along with the condensational/evaporative growth/shrink

in size. Three different mono-disperse initial cloud water droplet populations of radii 25 μm, 18 μm, and 6 μm have been simulated with the same initial background airflow conditions. This configuration of flow simulation represents a transient mixing in between a warm cloud top and above-lying clear air ambient. A transient initial value problem is simulated in this chapter, where the TKE inside the domain was initialized following the infield measurements of the TKE spectra in the ranges of the inertial sub-range and the dissipation range. The in-cloud measurements of the temperature and the water vapor density is replicated in the initial conditions of the same quantities. However, no fluctuations of the temperature or the density of water vapor are introduced in the initial conditions. The mixing in between the cloudy and the clear air regions of the domain produces the fluctuations in the scalar quantities, such as, temperature, density of water vapor. Therefore, fluctuations are also achieved on the saturation ratio. The entrainment of the subsaturated clear air inside the cloudy region and the detrainment of the supersaturated cloudy air is observed to happen during this transient mixing phenomenon. These processes widened the initial interface thicknesses for the kinetic energy as well as the scalars. Initial isotropic homogeneous turbulence inside the cloudy and the clear air region of the simulation domain gradually becomes anisotropic due to mixing. This was evident from the transient growth of the correlation scales.

Depending on the initial size of the droplet population, they are observed to undergo different transients, although they were initialized with the same background flow condition. This study attempts to investigate the differences in between the cloud droplet growth in the size gap from 15 μm to 40 μm of radius, and for the droplets smaller than 15 μm of radius. It is observed that the small 6 μm radius droplets do not grow by collision, but droplets inside the size gap grow significantly by droplet droplet collision and coalescence. The mixing produces a size broadening of the initial mono-disperse population due to the supersaturation fluctuations. These local supersaturation fluctuations are more influential for the smaller population. In the larger droplet populations of both the 25 μm and 18 μm radii, collisional growth becomes important. Multiple collisions have occurred in between the different sizes of the droplets. Since the flow is decaying with time, the gravitational settling becomes more and more important for the larger population as the simulation evolves, leading to a gradual removal of the falling droplets from the simulation domain. Therefore, these larger droplet populations show higher decorrelation in their vertical velocity from that of the fluid velocity. Droplets from both the 25 μm and 18 μm initial size population are observed to be removed from the simulation domain due to gravitational sedimentation. On the contrary, the reduction in total droplet count for the 6 μm initial size population happened mostly due to the complete evaporation of the sub-micron sized droplets of this population. These droplets were very sensitive to local subsaturation due their very small size. This smaller droplet population has a small Stokes number, which makes them follow the fluid velocity almost perfectly. Also due to a very small settling parameter due

to negligible terminal velocity of these smaller population, they are not observed to sediment. With the decay in the TKE, these droplets are observed to remain dispersed in the domain with very negligible vertical velocity/sedimentation.

In order to find the impact of the stable, unstable or neutrally stratified airflow conditions on the transient evolution of the initial mono-disperse cloud droplet populations, 9 simulations are conducted with the same initial mono-disperse 20 μm radius droplet populations in the same initial flow conditions for the gradient of turbulent kinetic energy across the interface. However, the initial temperature and the density of water vapor conditions are varied to create three different initial stratification profiles and three different initial supersaturation profiles. The initial supersaturation conditions are varied as strong ($RH_{cloud} = 110\%$ and $RH_{air} = 40\%$), moderate ($RH_{cloud} = 110\%$ and $RH_{air} = 60\%$) and mild ($RH_{cloud} = 105\%$ and $RH_{air} = 85\%$). The probability distribution of the droplet sizes shows that the widening in the initial droplet size increases with the increase in the supersaturation gradient between the cloud and the clear air. Whereas, the temperature stratification profile has significant influence on the droplet size broadening. The unstably stratified airflow conditions result in increased mixing across the initial interface, which widens the droplet size distribution at the highest amount for all the supersaturation gradients. On the contrary, the stably stratified conditions inhibit the mixing across the interface, and therefore, are observed to result in least droplet size broadening. The neutrally stratified condition, whereas, produces a moderate broadening in between the limits of the droplet size ranges observed for the stable and the unstably stratified airflow conditions.

End of Chapter 2

Chapter 3

Fluid Flow and Scalar Transport in the Wake of a Sphere

A part of this chapter is already published in Bhowmick, T., Wang, Y., Iovieno, M., Bagheri, G. and Bodenschatz, E. (2020), "Population Distribution in the Wake of a Sphere", Symmetry, volume 12, issue 9, article number 1498 [10]. In this chapter, a comprehensive numerical study on the details of the momentum and scalar transport in the wake of a sphere will be presented using a population density distribution approach for the steady axisymmetric and oblique wake regimes. Descriptive statistics regarding the spatial structure of the fluid and scalar transport in the wake is of primary importance, when the extent of the wake with certain properties needs to be quantified. Investigation of the supersaturation in the wake of precipitating cloud hydrometeors, which is investigated by Bhowmick et al. (2020) [11] and Krayer et al. (2020) [72], have important implications for cloud life cycle. Such studies would requires for example a detailed analysis of the transported scalar population in the wake. In order to quantify the extent of the supersaturated volume in the wake of a cloud droplet, where aerosols can grow by the deposition of the excess water vapor in the supersaturated wake and can be activated due to sufficiently long exposure to supersaturation in the droplet wake [11]; one needs to know about the details of the scalar population in the wake with a quantification on the scalar transport and its population distribution. In this Chapter, the details of the numerical setup and the details of the momentum and scalar transport in the wake of a sphere for the various steady axisymmetric and oblique wake regimes will be presented. An introduction to the numerical methods and computational details are described in Section 3.1 and 3.2. Results are presented and discussed in Section 3.3, which includes visualization of the structure of the wake for both the fluid and the scalar transport for various steady axisymmetric and oblique wake Reynolds numbers. A new approach, the population density distribution, is used for the detailed quantification of the transport phenomena in the wake. A summary and conclusions of this chapter is given in Section 3.4.

3.1 Details of the Physical Model

In this section, an overview of the physical model, and the derived dimensionless equations and the relevant dimensionless parameters are presented.

3.1.1 Equations for Solving the Fluid Flow

The physical model considers the flow which develops past a sphere, that is placed in incompressible viscous fluid with velocity $\mathbf{u}_\infty = (u_\infty,0,0)$, pressure p_∞, and a constant density ρ. Together with the balances of mass and momentum, also the transport of passive scalars is considered, that are any contaminants present in low concentration so that they do not influence the flow. Such dynamics is described in an Eulerian framework by an advection–diffusion (AD) equation. The equations in the physical form are written as:

$$\nabla \cdot \mathbf{u} = 0 \tag{3.1}$$

$$\frac{\partial \mathbf{u}}{\partial t} + \mathbf{u} \cdot \nabla \mathbf{u} = -\frac{1}{\rho_0}\nabla p + \nu \nabla^2 \mathbf{u} \tag{3.2}$$

$$\frac{\partial \theta}{\partial t} + \mathbf{u} \cdot \nabla \theta = \kappa_\theta \nabla^2 \theta \tag{3.3}$$

where $\partial/\partial t$ is the temporal derivative, ρ_0 is reference mass density of air at reference ambient temperature T_∞ and pressure p_∞, ∇p is the pressure gradient, ν is the kinematic viscosity and κ_θ is the scalar diffusivity of the scalar θ.

If d_p is the diameter of the particle/sphere, θ_p and θ_∞ are the scalar concentration on the surface of the sphere and in the external flow respectively, the problem can be suitably made dimensionless by using d_p, u_∞ and $\theta_p - \theta_\infty$ as scales, and therefore by defining the dimensionless position, time, velocity, pressure, and scalar concentration as,

$$\mathbf{x}^* = \frac{\mathbf{x}}{d_p}, \;\; t^* = \frac{t u_\infty}{d_p}, \;\; \mathbf{u}^* = \frac{\mathbf{u}}{u_\infty}, \;\; p^* = \frac{p - p_\infty}{\rho u_\infty^2}, \;\; \theta^* = \frac{\theta - \theta_\infty}{\theta_p - \theta_\infty}.$$

3.1.2 Dimensionless Equations for Solving the Flow Field

Therefore, the dimensionless incompressible Navier-Stokes (NS) equations and the one-way coupled AD equation for the scalar are,

$$\nabla^* \cdot \mathbf{u}^* = 0, \tag{3.4}$$

$$\frac{\partial \mathbf{u}^*}{\partial t^*} + \mathbf{u}^* \cdot \nabla^* \mathbf{u}^* = -\nabla^* p^* + \frac{1}{Re}\nabla^{*2} \mathbf{u}^*, \tag{3.5}$$

$$\frac{\partial \theta^*}{\partial t^*} + \mathbf{u}^* \cdot \nabla^* \theta^* = \frac{1}{Re\,Sc}\nabla^{*2} \theta^*, \tag{3.6}$$

where $Re = u_\infty d_p / \nu$ is the Reynolds number and $Sc = \nu / \kappa_\theta$ is the Schmidt number, the ratio between the kinematic viscosity and the scalar diffusivity κ_θ. These equations are complemented by uniform flow boundary conditions far from the sphere ($\mathbf{u}^* \to (1,0,0)$, $\theta^* \to 0$) and no slip boundary conditions on the surface of the sphere with a constant scalar concentration ($\mathbf{u}^* = 0$, $\theta^* = 1$). Since only the dimensionless variables will be used throughout the rest of this chapter, $*$ will be dropped from the dimensionless variables for the sake of simplicity.

3.2   Details of the Numerical Method in DNS

In this section, the details of the numerical methods, choices of lattices for the fluid velocity and the transported scalars, and the details of the simulation setup and validation are presented.

3.2.1   The Lattice Boltzmann Method

These governing equations are numerically solved with the lattice Boltzmann method (LBM) [136, 74]. A code is developed based on the open-source library, Palabos [83]. The discretized Lattice-Boltzmann equation (LBE) solves the discrete-velocity distribution function $f(\mathbf{x}, t)$ for the velocity distribution of a fictitious fluid particle population. The LBE approximates the continuum problem [74, 98]. In LBM, the particle distribution function $f(\mathbf{x}, t)$ is governed by:

$$
\begin{aligned}
f_i(\mathbf{x} + \mathbf{c}_i \Delta t, t + \Delta t) &= f_i(\mathbf{x}, t) + \Omega_i(\mathbf{x}, t), \\
\Omega_i(\mathbf{x}, t) &= -\frac{\Delta t}{\tau}(f_i(\mathbf{x}, t) - f_i^{eq}(\mathbf{x}, t)).
\end{aligned}
\tag{3.7}
$$

Here i is the direction/index of the individual velocity components of the discrete-velocity set $\mathbf{c}$, which defines the structure of lattice. $\mathbf{x}$ and t are the location of a lattice node and the time respectively. Here a fluid particle population $f_i(\mathbf{x}, t)$ moves to a neighbouring point $\mathbf{x} + \mathbf{c}_i \Delta t$ with the velocity $\mathbf{c}_i$ at the next time step $t + \Delta t$. The collision operator $\Omega_i(\mathbf{x}, t)$ models the redistribution of the particle populations at each lattice node. In this study, the Bhatnagar-Gross-Krook (BGK) collision operator [117] is considered, with which the population $f_i(\mathbf{x}, t)$ relaxes towards its equilibrium state $f_i^{eq}(\mathbf{x}, t)$ according to the relaxation time scale τ defined below, which determines the speed of this equilibration process for the fluid particle distribution function [74]. $f_i^{eq}(\mathbf{x}, t)$ and τ are defined as:

$$
\begin{aligned}
f_i^{eq}(\mathbf{x}, t) &= w_i \rho \left(1 + \frac{\mathbf{c}_i \cdot \mathbf{u}}{c_s^2} + \frac{(\mathbf{c}_i \cdot \mathbf{u})^2}{2 c_s^4} + \frac{\mathbf{u} \cdot \mathbf{u}}{2 c_s^2}\right), \\
\nu &= c_s^2 \left(\tau - \frac{\Delta t}{2}\right).
\end{aligned}
$$

Here w_i is the weight, c_s is the speed of sound. The macroscopic quantities, such as the density ρ and velocity $\mathbf{u}$ are moments of $f_i(\mathbf{x}, t)$, according to $\rho = \sum_i f_i(\mathbf{x}, t) = \sum_i f_i^{eq}(\mathbf{x}, t)$ and $\rho\mathbf{u} = \sum_i \mathbf{c}_i f_i(\mathbf{x}, t) = \sum_i \mathbf{c}_i f_i^{eq}(\mathbf{x}, t)$ respectively.

The one-way coupling between the fluid momentum $\rho\mathbf{u}$ and the scalar concentration θ is solved by another LBM equation similar to equation (3.7), but with a distribution function $g_i(\mathbf{x}, t)$ for the scalar. To recover the AD equation, the equilibrium distribution function $g_i^{eq}(\mathbf{x}, t)$ [47] and the relaxation time scale τ_g, which determines the speed of the equilibration process for the scalar distribution function [74], are used as,

$$
\begin{aligned}
g_i^{eq}(\mathbf{x}, t) &= w_i\theta(1 + \frac{\mathbf{c}_i \cdot \mathbf{u}}{c_s^2}), \\
\kappa_\theta &= c_s^2(\tau_g - \frac{\Delta t}{2}).
\end{aligned}
$$

The scalar concentration θ is calculated according to $\theta = \sum_i g_i(\mathbf{x}, t) = \sum_i g_i^{eq}(\mathbf{x}, t)$.

3.2.2 Choices of Lattices

In the lattice Boltzmann method, different lattices are developed to recover the governing equations, for e.g. to recover the incompressible Naiver-Stokes (NS) equations considered in this chapter. In Figure 3.1, the choices of the velocity sets for the three dimensional flow is shown. For the three dimensional flows, D3Q15, D3Q19 and D3Q27 are the common choices of lattices. Theoretically, the more discrete speeds (Q-), the more accurate the lattice is. At the same time, comparison on those lattices can also be found in literature. For example, the analysis by Safi et al. (2017) [125] shows that qualitatively all the three lattices give similar result on the recovered macroscopic quantities of the NS equations. However, they conclude that "the D3Q19 stencil provides the required isotropy at a reasonable extra cost compared to D3Q15, while the D3Q27 stencil asks for more than 50% longer simulation times and no noticeable accuracy improvement upon the D3Q19 stencil". In the simulation of natural convection heat transfer, Nor Azwadi and Syahrullail (2009) [106] compared the D3Q15 and D3Q19 lattices, and concluded that the D3Q15 lattice show some discrepancy with the NS solution (Table 1 in that paper) for higher Rayleigh number and prone to instability, but D3Q19 lattice was in good agreement with NS solutions and computationally stable. On the other hand, comparison of the D3Q19 and D3Q27 lattices produce almost identical results as extensively described by Opadrishta (2016) [108] and also by Safi et al. (2017) [125], among others. Therefore, the D3Q19 and D3Q27 lattices will produce almost indistinguishable moments of the discrete velocity sets and therefore, equivalent population distribution functions at the steady Reynolds numbers of our study. Considering that the D3Q19 needs less discrete speeds and thus is more efficient than the D3Q27 lattice, we chose the D3Q19 lattice for simulating the flow field

in our simulations which have one rest-velocity and 18 non-rest velocities at each lattice node. Moreover, since the non-linear momentum advection corrections are not very significant in the steady axisymmetric or oblique wake flows, D3Q19 lattice is a better choice than the D3Q27 lattice [133].
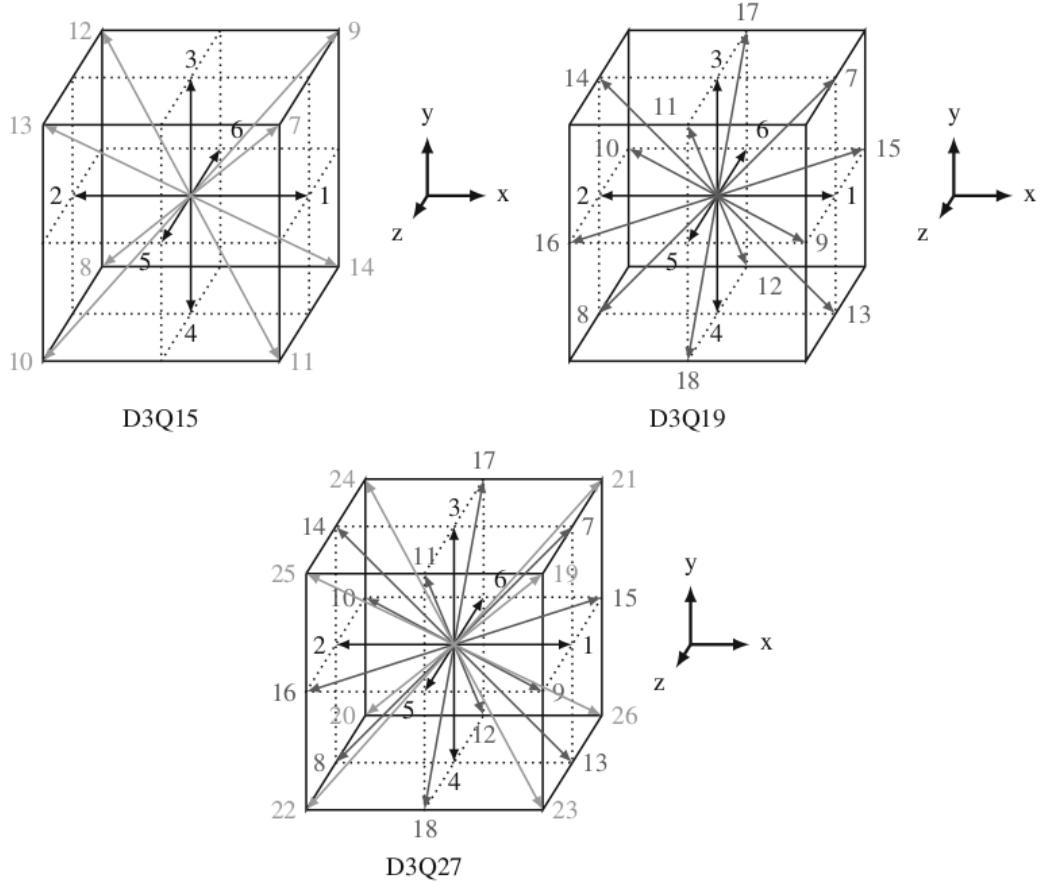
Figure 3.1: Source: Krüger et al (2017) [74]. The D3Q15, D3Q19 and D3Q27 velocity sets are shown here. The cube denoted by solid lines has edge length of $2\Delta x$. The velocities with length $|c_i| = 1, \sqrt{2}, \sqrt{3}$ are shown in black, darker grey and lighter grey colors respectively. Rest velocity vectors $c_0 = 0$ are not shown.

In order to solve the transported scalars in this study, the $D3Q7$ advection-diffusion lattice is chosen. Since only the zeroth and the first order moments of $g_i(\mathbf{x}, t)$ are used to recover the AD equation from the LBM equation, a $D3Q7$ lattice, which has a rest velocity and six velocities along the main lattice axes, is a good compromise for solving the scalar fields [74].
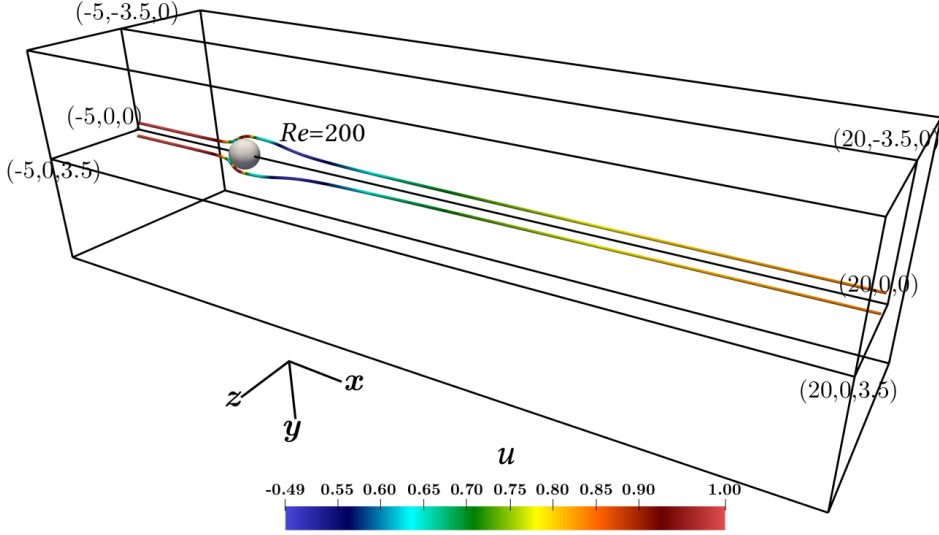
Figure 3.2: Sketch of the computational domain used in the simulations. The centre of the sphere is in the origin of the coordinate system. The flow moves from the left to the right in the picture. Two streamlines at Re = 200 are shown as an example.

3.2.3 Details of the Simulation Setup and Validation

The sphere is set in the origin of the reference frame, and the dimensionless domain is $[-5,20]d_p \times [-3.5,3.5]d_p \times [-3.5,3.5]d_p$ in size (5 diameters upstream, 20 diameters downstream and 7 diameters in the transversal directions) as shown in Figure 3.2. The domain is discretized with a uniform Cartesian mesh with a grid size equal to 1/32 of the sphere diameter. Dirichlet and Neumann boundary conditions are considered for the inlet and outlet boundaries, respectively. For the lateral boundaries in transversal directions, periodic boundary conditions are applied. A second order extrapolation scheme, proposed by Guo et al. (2002) [48], is adopted for the curved boundary of the sphere.

The numerical setup is validated by comparing the drag coefficient, the length of the recirculating zone and the angle of separation with the existing research for the fluid velocity field. Mesh independence test is performed with different mesh spatial resolutions, including $d_p/24$, $d_p/32$, $d_p/40$ and $d_p/48$, which is shown in the Figure 3.3. In Figure 3.3(a), a box plot of the drag coefficient, C_D is produced for each simulation run with different resolutions in a simulation domain size of $[-5,35]d_p \times [-5,5]d_p \times [-5,5]d_p$ for the $Re = 200$ simulation. It can be seen that the drag coefficients show negligible difference for the grid size of $d_p/32$ and lower. A comparison on the length of the recirculating zone L_W and the angle of separation is presented in Figure 3.3(b) for the different mesh resolutions, which again have shown negligible difference for the grid size of $d_p/32$ and lower, with maximum variation in the length of the recirculating zone, which is up to 0.7%. Therefore,
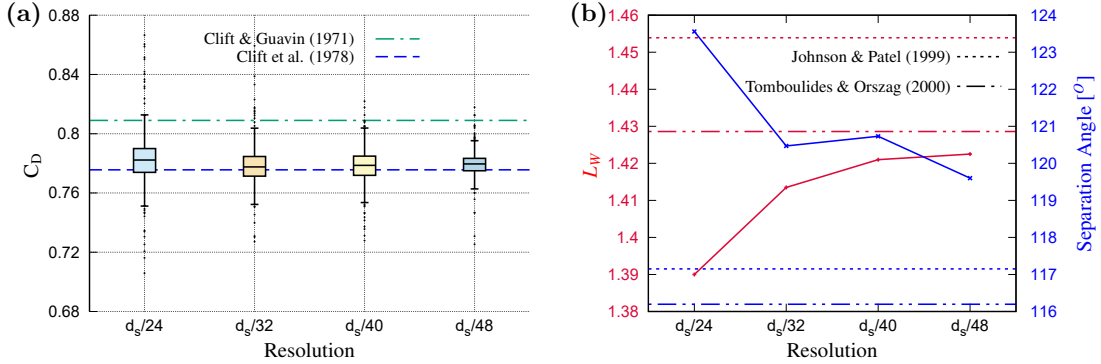
Figure 3.3: Mesh independence test: (a) Drag coefficient C_D and (b) the wake length L_W normalized with sphere diameter d_p, and the angle of separation for various spatial resolutions of the mesh at $Re = 200$, together with existing research [23, 22, 66, 142].

the $d_p/32$ grid size is chosen for conducting the following domain size independence tests.
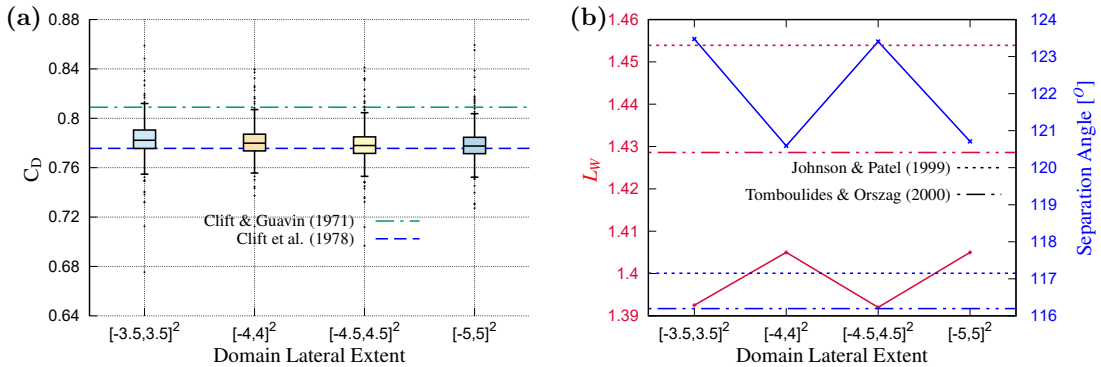
Figure 3.4: Domain lateral extent independence test: (a) Drag coefficient C_D and (b) the wake length L_W normalized with sphere diameter d_p, and the angle of separation for various lateral extents of the domain, while keeping the streamwise extent fixed at $[-5,35]d_p$ and with a constant spatial resolutions of $d_p/32$ at $Re = 200$, in comparison to the existing research [23, 22, 66, 142].

The domain size independence tests are conducted for various transversal/lateral and the streamwise extents of the domain, from $[-5,35]d_p \times [-5,5]d_p \times [-5,5]d_p$ to $[-5,35]d_p \times [-3.5,3.5]d_p \times [-3.5,3.5]d_p$ (changing the transversal/lateral extent), and from $[-5,35]d_p \times [-3.5,3.5]d_p \times [-3.5,3.5]d_p$ to $[-5,20]d_p \times [-3.5,3.5]d_p \times [-3.5,3.5]d_p$ (changing the streamwise extent) with grid size $d_p/32$. Figure 3.4 presents the domain lateral extent independence tests, where the lateral extent of the domain is varied from $[-5,5]d_p \times [-5,5]d_p$ to $[-3.5,3.5]d_p \times [-3.5,3.5]d_p$ keeping the streamwise

extent a constant at $[-5,35]d_p$ in length. In the plot of C_D in Figure 3.4(a), almost no variation is visible, which proves the transversal extent independence in the computation of the drag coefficient for a domain with lateral extent of $[-3.5,3.5]d_p \times [-3.5,3.5]d_p$ or higher. The plot of L_W and the angle of separation in Figure 3.4(b) also shows almost negligible differences in these validation quantities. The domains have shown a variation which forms a saw tooth like structure, indicating that the variation in these values are just a numerical artefact. The variation in the length of the recirculating zone, which is up to 0.71%, is the highest out of all these validation quantities. In Figure 3.5, the domain streamwise extent independence test is conducted by varying the streamwise extent from $[-5,35]d_p$ to $[-5,20]d_p$, keeping the lateral extent fixed at $[-3.5,3.5]d_p \times [-3.5,3.5]d_p$ and the grid size fixed at $d_p/32$. The C_D in Figure 3.5(a), and the L_W and the angle of separation in Figure 3.5(b) present almost no differences in these validation quantities. One point to be noted is that we use a uniform Cartesian mesh which does not fit the spherical surface of the object boundary, which result in some but very minor variation in the length of the recirculating zone and in the angle of separation from the observations by the previous researches, such as Tomboulides and Orszag (2000) [142], or Johnson and Patel (1999) [66]. All these previous research used a object's curved boundary fitting mesh, which resolves the boundary layer flow with very fine details and provides an exact quantification on the angle of separation. The angle of separation, however, can not be achieved precisely in the presented uniform Cartesian mesh. This variation, however, does not not influence the structure of the fluid and the scalar transport in the wake of the sphere, which is presented below.
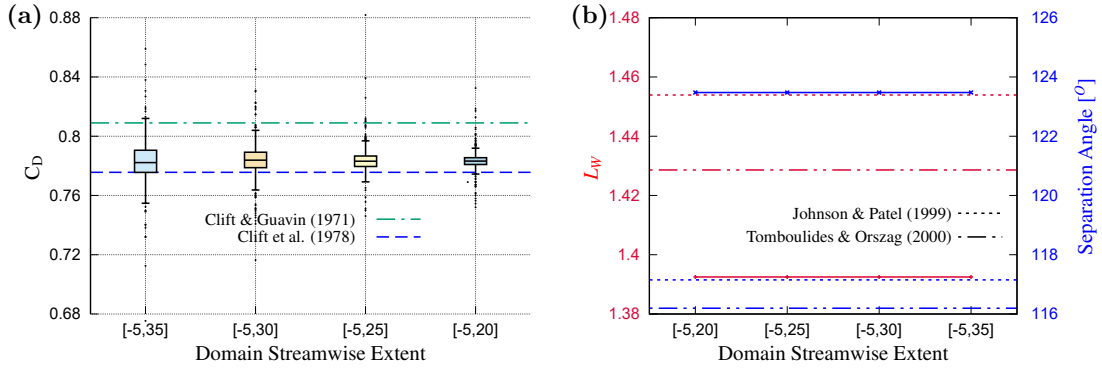
Figure 3.5: Domain streamwise extent independence test: (a) Drag coefficient C_D and (b) the wake length L_W normalized with sphere diameter d_p, and the angle of separation for various streamwise extents of the domain, while keeping the transversal/lateral extent fixed at $[-3.5,3.5]d_p \times [-3.5,3.5]d_p$ and with a constant spatial resolutions of $d_p/32$ at $Re = 200$, in comparison to the existing research [23, 22, 66, 142].

In Figure 3.6(a), the drag coefficient C_D obtained from our simulation is compared with the empirical equations (equations (3.8) and (3.9)) of Clift et al. (1978) [23] and with the numerical results of Johnson and Patel (1999) [66]. The drag coefficient deviates from the empirical equations maximum at $Re = 25$, with relative error 3.5%, which is further reduced with higher Re, e.g. less than 1% at $Re = 200$. Figure 3.6(b) presents the results of the normalized wake length L_W along with the numerical results of Johnson and Patel (1999) [66], Tomboulides and Orszag (2000) [142], and experimental data of Taneda (1956) [139], which reported transition to unsteady wake for $Re \geq 130$.
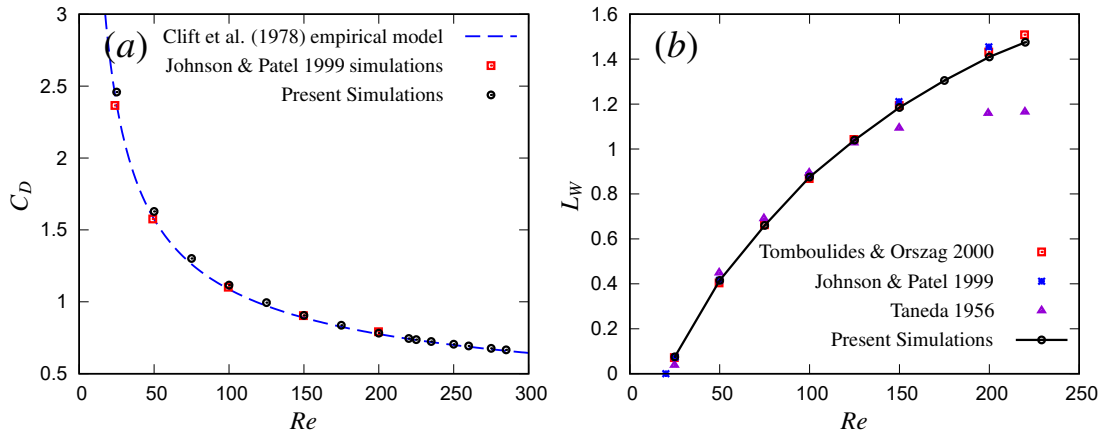
Figure 3.6: (a) Drag coefficient C_D and (b) the wake length L_W normalized with sphere diameter d_p for various steady axisymmetric and oblique Re with existing research [23, 66, 142, 139].

The scalar field is validated by comparing the normalized scalar profiles with other numerical simulations. In Figure 3.7, the numerical results of this present study is compared with the numerical results of Chouippe et al. (2019) [20] for various wake regimes. For the steady axisymmetric and the oblique wake regimes in Figure 3.7(a,b), which are investigated in this chapter, the numerical method used in this study is able to capture the dynamical evolution with sufficient accuracy. However, it must be noted that the numerical method used by Chouippe et al. (2019) is spectral/spectral-element method on a cylindrical domain, and a body fitting spectral-element mesh is used for their study. Moreover, a Galileo number $Ga = u_g d_p / \nu$ (where $u_g = \sqrt{|(\rho_p / \rho - 1)g|d_p}$ is the velocity scale dependent on the particle/fluid density ratio ρ_p / ρ, the gravitational acceleration g and the sphere diameter d_p) is used, which is proportional to the Reynolds number Re, as $Ga = \sqrt{3C_D/4}Re$. Due to the differences in the coordinate system and in the sampling plane and due to the oscillating nature of the $Re = 300/Ga = 200$ flow in Figure 3.7(c), the distant parts of the scalar contours of the present study do not appear to match well with the results of Chouippe et al. (2019).
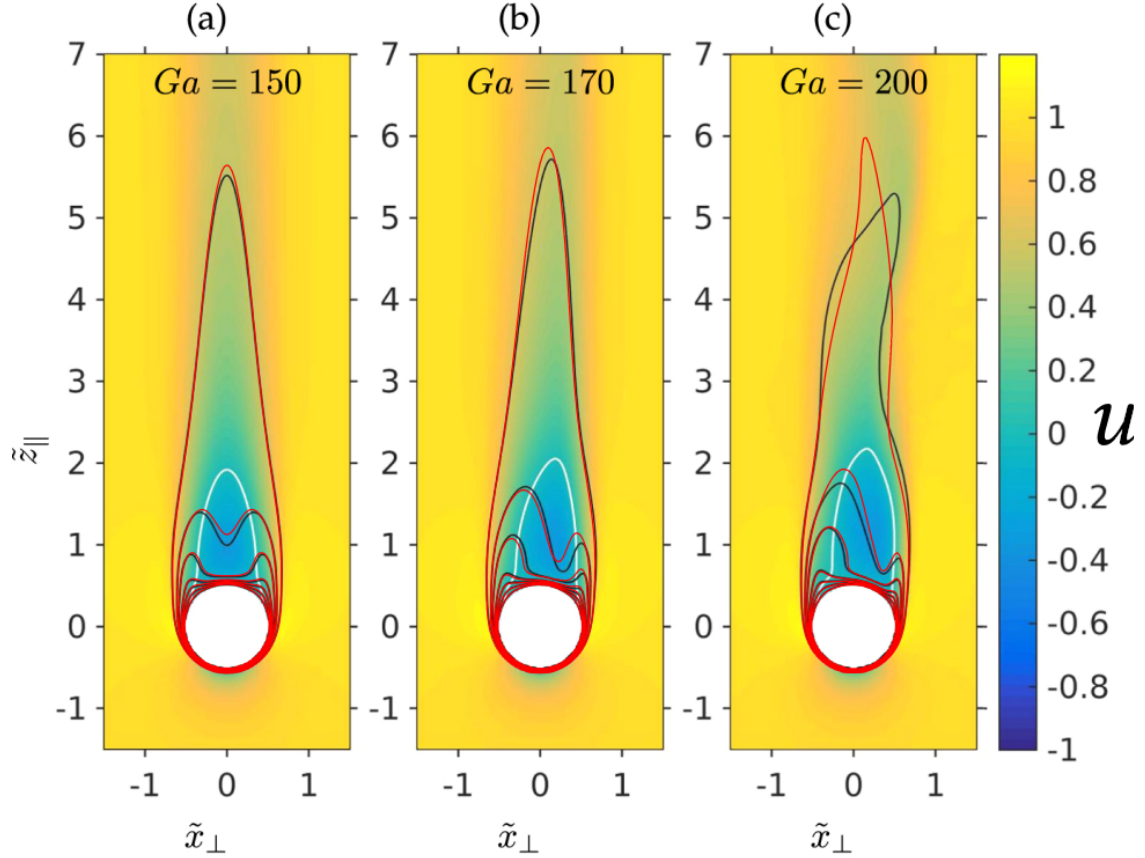
Figure 3.7: Validation of the scalar θ distribution: (a) Steady axisymmetric $Re = 200/Ga = 150$, (b) steady oblique $Re = 235/Ga = 170$ and (c) unsteady oscillating $Re = 300/Ga = 200$ scalar contours plots for scalar diffusivity of $Sc = 0.72$ by Chouippe et al. (2019) [20] in black lines is compared with the results of the present study with $Sc = 0.71$ in the red lines. The contour lines for the θ are plotted at magnitudes of 0.2, 0.35, 0.45, 0.6, 0.7, 0.8 and 0.9, ascending from the ambient towards the sphere.

In Figure 3.8, the scalar θ contours are compared for the used $d_p/32$ grid size and the highest simulated resolution of $d_p/48$ grid size. It can be seen that the highest variation in the scalar contour profiles shows a maximum of 2 lattice node difference for the grid size of $d_p/32$. Similarly, the highest difference in the scalar contour profiles for the steady axisymmetric regime in Figure 3.7(a) is 2 lattice nodes from the temperature profiles of Chouippe et al. (2019) [20] at a similar scalar diffusivity of $Sc = 0.7$.
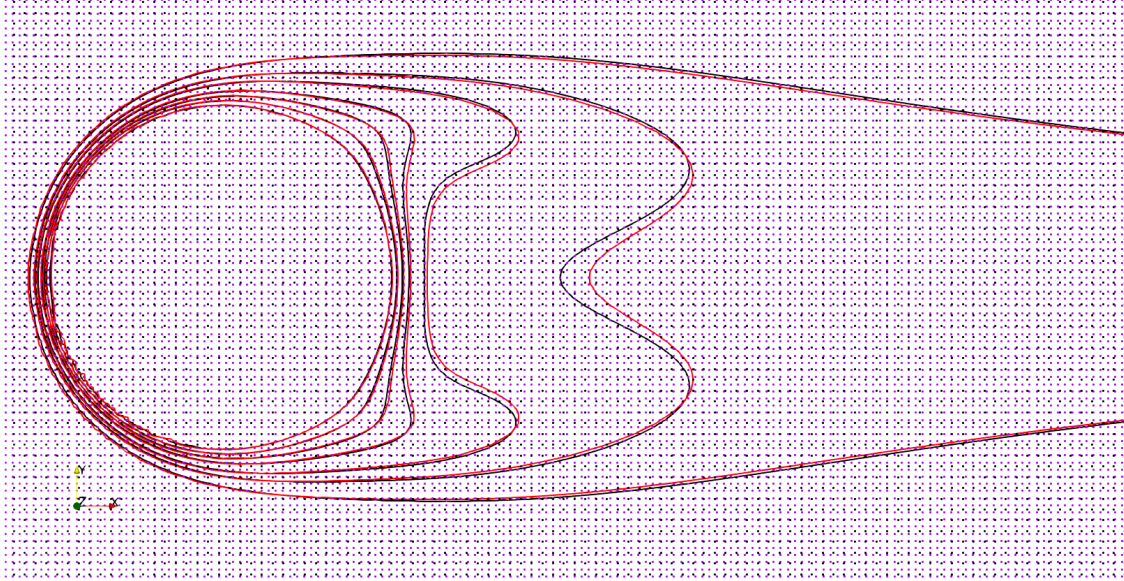
Figure 3.8: Comparison of scalar θ contours at magnitudes of 0.2, 0.35, 0.45, 0.6, 0.7, 0.8 and 0.9, ascending from the ambient towards the sphere, for the grid size of $d_p/32$ in black and for the grid size of $d_p/48$ in red colors. The black dots represent the lattice nodes for the grid size of $d_p/32$, while the pink dots are the lattice nodes at grid size of $d_p/48$.

$$C_D \;=\; \frac{24}{Re}(1 + 0.1935 \cdot Re^{0.6305}),$$
$$\text{if } 20 \leq \text{Re} \leq 260. \qquad (3.8)$$
$$\log_{10} C_D \;=\; 1.6435 - 1.1242 \cdot \log_{10} Re + 0.1558 \cdot (\log_{10} Re)^2,$$
$$\text{if } 260 \leq \text{Re} \leq 1500. \qquad (3.9)$$

3.3 Wake Structure at Steady Reynolds Numbers

3.3.1 Spatial Structure of the Fluid Flow

Our work focuses on the wake behind a wet sphere in the steady axisymmetric regime ($0 \leq Re \leq 220$) and the steady oblique regime ($225 \leq Re \leq 285$). The difference in the overall features of these regimes can be appreciated from Figure 3.9, which visualizes the streamwise velocity u in color together with the contours of two advected scalar fields θ_1 in black and θ_2 in white of different scalar diffusivities in two perpendicular planes (z, x) and (y, x) passing through the center of sphere in parallel to the incoming flow. The Schmidt numbers for the scalars are 0.71 and 0.61, respectively, which correspond to the diffusivities of temperature and
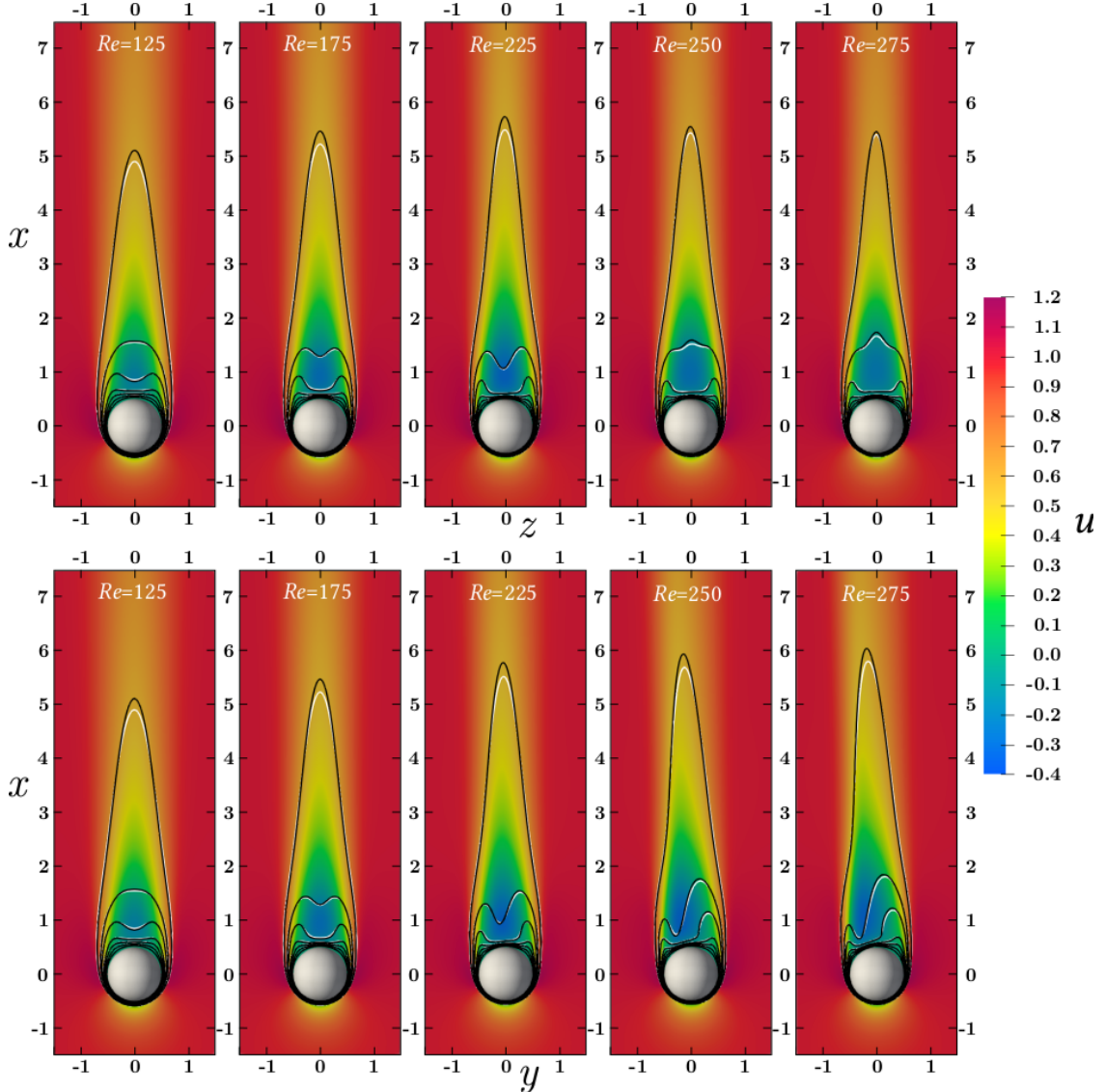
Figure 3.9: Spatial distribution of the dimensionless streamwise component of fluid velocity u in color and the contour lines of a scalar θ_1 in black ($Sc = 0.71$) and another scalar θ_2 in white ($Sc = 0.61$) for various steady axisymmetric and oblique Re. The visualization is across two central orthogonal planes (z, x) and (y, x) passing through the center of the sphere with an extent of $[-1.5, 1.5]d_p$ along the horizontal axes and $[-1.5, 7.5]d_p$ along the vertical x axis. Contour lines for θ_1 and θ_2 are plotted at magnitudes of 0.2, 0.35, 0.45, 0.6, 0.7, 0.8 and 0.9, ascending from the ambient towards the sphere.

water vapor in the air. The increase in Re features the thinning of the boundary layer, as well as a shrinking in the lateral extent of the wake and a stretching in

the streamwise direction as in Figure 3.9 up to $Re = 220$. In the oblique regime, a tilt from the centerline ($y = z = 0$) along the (y, x) plane is observed, which is symmetric along (z, x) plane, see also [66, 20]. This tilt in the oblique regime increases with Re until the wake becomes unstable and starts shedding vortices at $Re \geq 290$. The apparent decrease in the streamwise length of the wake in the top panel of Figure 3.9 from $Re = 225$ to 275 is attributed to the tilting of the wake. The transport of any scalar θ is described by the same equation (3.6). The only difference lays in their Schmidt numbers, which govern their relative diffusivities. The different diffusivities govern the profiles of the scalars at the intermediate values of the dimensionless concentration, which shows difference in the external part away from the sphere boundary and in the far wake (for $\theta \sim 0.2$ to 0.4), as shown in Figure 3.9. In Figure 3.9, the white contour lines (θ_2 with $Sc = 0.61$) have wider spread in the boundary layer region than the black contour lines (θ_1 with $Sc = 0.71$), which shows that θ_1 has higher gradient than θ_2 due to larger diffusivity coefficient. However, at the far wake region downstream, one can see a different behavior. Due to low diffusivity, the white contour lines (θ_2 with $Sc = 0.61$) smooths to the ambient concentration earlier than the black ones (θ_1 with $Sc = 0.71$). However the impact of diffusivity coefficients on scalar distribution profile needs to be verified with studies involing scalars with larger differences in diffusivities.

In Figure 3.10 and 3.11, detailed pictures on the spatial distribution of the streamlines, velocity contours and the scalar contours for two different diffusivities (θ_1 with $Sc = 0.71$ and θ_2 with $Sc = 0.61$) are presented for various steady axisymmetric Re, varying from 25 to 200 with an increment of $Re = 25$ for each presented case. Since the wake structure is symmetric by the centerline ($y = z = 0$), any orthogonal plane passing through the center of the sphere ($x = y = z = 0$) would produce identical two dimensional wake profiles like the Figure 3.10 and 3.11. As elaborated for the previous Figure 3.9, the gradual thinning in the boundary layer for both the fluid flow and the scalars can be well appreciated in Figure 3.10 and 3.11. The change in the length of the recirculating zone is well visible, where the recirculating eddies are observed to be elongated streamwise with an increment in Re. The corresponding change in the angle of separation is also visible from the streamlines. The lateral thinning of the wake structure, which prevails both in the structure of the flow velocity and also in the scalars, is explained in details with the contours plots for both the magnitudes of the velocity on the top panels and for the scalars in the bottom panels of Figure 3.10 and 3.11. It can further be seen that the wedge shaped downstream profile in the scalar wake does not happen unless Re is around 125 and higher as in Figure 3.11. For the $Re >= 125$, the scalars show lower diffusivity and transport along the centerline ($y = z = 0$) due to the gradual strengthening in the recirculating eddies, while towards the centers of these eddies, the scalars show a higher diffusivity and transport.

Figure 3.12 presents a visualization of flow transition from the steady axisymmetric wake at $Re = 150$ to the beginning of the oblique wake at $Re = 225$, and
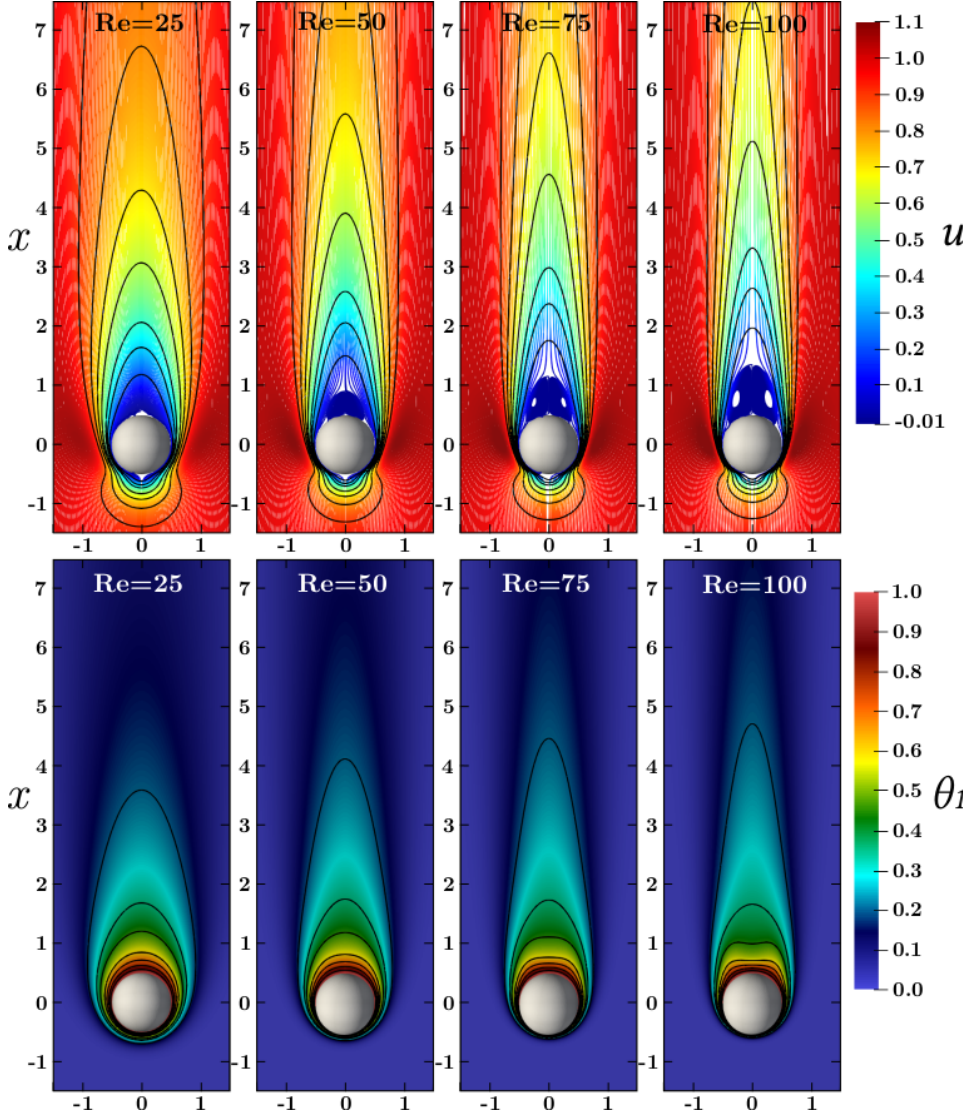
Figure 3.10: Detailed steady axisymmetric flow structure from $Re = 25$ to 100. In the top panel, the spatial distribution of the streamlines is presented in color, according to the dimensionless streamwise component of fluid velocity u. The black contour lines on the top of these streamlines are the velocity magnitudes at 0.2, 0.35, 0.45, 0.6, 0.7, 0.8 and 0.9 values, ascending from the sphere towards the ambient free flow. In the bottom panel, the spatial distribution of the scalar θ_1 with $Sc = 0.71$ is presented in color, and the scalar θ_2 with $Sc = 0.61$ is presented as contour lines. The contour lines of θ_2 are plotted at magnitudes of 0.2, 0.35, 0.45, 0.6, 0.7, 0.8 and 0.9, ascending from the ambient towards the sphere. The visualization is across the central orthogonal plane with an extent of $[-1.5, 1.5]d_p$ along the horizontal axes and $[-1.5, 7.5]d_p$ along the vertical x axis.
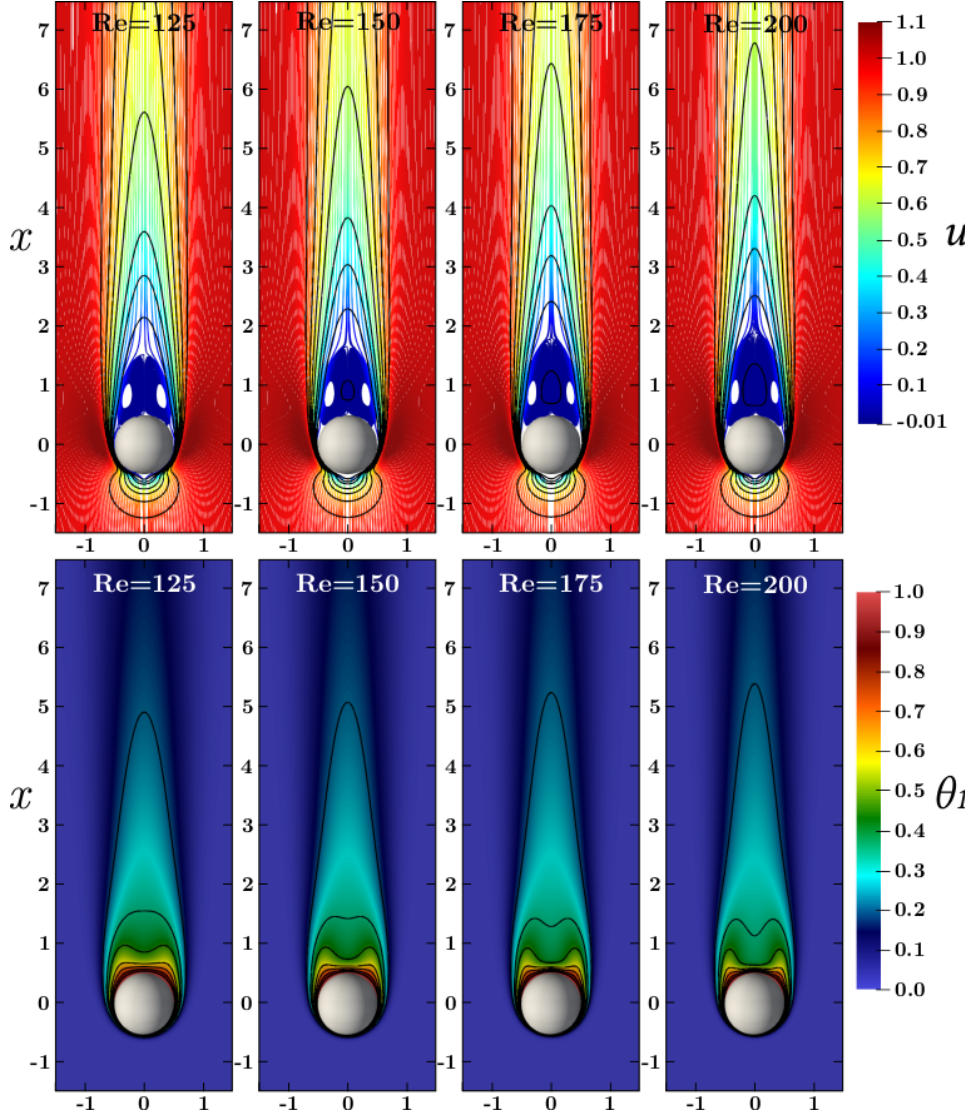
Figure 3.11: Detailed steady axisymmetric flow structure from $Re = 125$ to 200. For details see the caption of Figure 3.10.

then the fully developed oblique wake structure at $Re = 285$. The two dimensional structure of the steady axisymmetric wake transforms into three dimensional complex vortices in the recirculating zone, which starts around $Re = 225$. However, although the three dimensional structure of the $Re = 225$ wake can be well appreciated, obliqueness is rarely visible, as also seen in Figure 3.9. The streamlines of the $Re = 285$ wake in Figure 3.12 however, is very complex, which shows a typical continuity between the different vortices, as also seen by Johnson and Patel (1999) [66]. The recirculating streamlines start to entrain from the edge of a vortex and reach the core, and then exit this first vortex and enter the second vortex at its
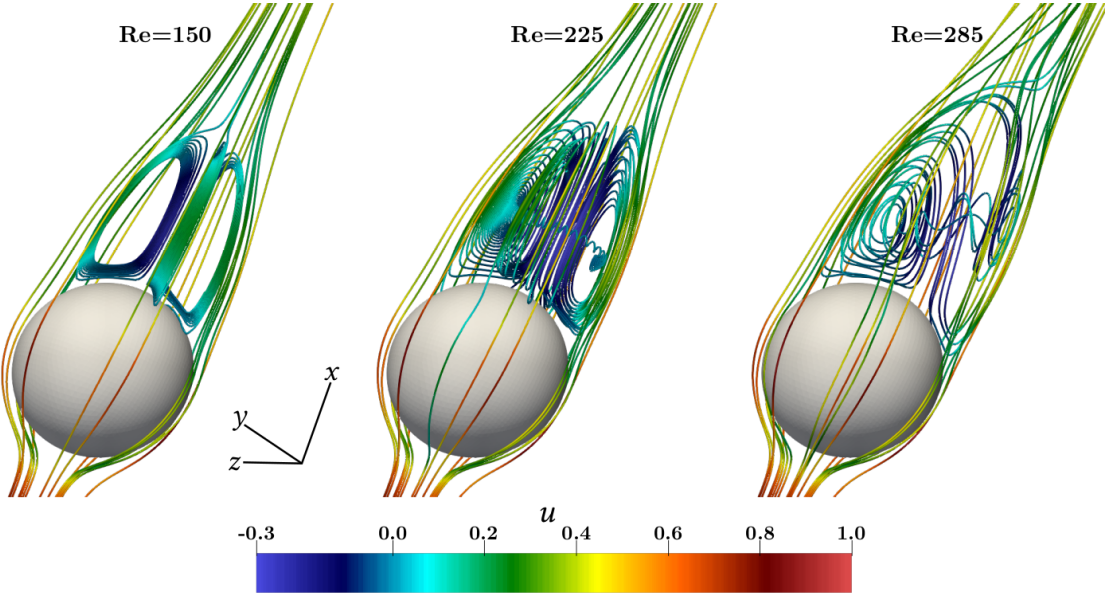
Figure 3.12: Streamlines at $Re = 150$, 225 and 285 colored according to the dimensionless streamwise component of fluid velocity u.

center. In this second vortex, the streamlines start to move gradually towards the edge of the vortex and finally go out of the recirculating zone by making a large cross-over around the first vortex. Therefore, one vortex feeding to another vortex is well seen in the oblique wake regime.

In order to provide a detailed description of the flow field, a population density approach is used. For any variable, such as the longitudinal velocity component u, its population density distribution $N(u)$ at a u_0 magnitude is defined as $N(u_0) = \mathrm{d}V_u(u_0)/\mathrm{d}u$, where $V_u(u_0)$ is the volume of the region in which u is lower that u_0. The distribution of u is shown in Figure 3.13 for three different Reynolds numbers (Re = 75, 175 and 275). Figure 3.13(a) and (b) present the contour lines of $u = 0.95$ in solid lines and of pressure $p = 0$ in dashed thin lines across the (z, x) and (y, x) orthogonal planes respectively. The domain is divided into two main parts: an upstream zone where the flow approaches the sphere and a downstream zone dominated by the presence of the wake. The dotted horizontal black line in panels (a) and (b) of Figure 3.13, located at $x = -0.325$, intersects the sphere where the dimensionless pressure p changes sign and distinguishes the two zones. The velocity component u in the upstream zone ($p \geq 0$) does not show significant changes with Re, but the above mentioned lateral thinning is visible in the downstream zone, which has mostly negative p. Tilting is also observed in Figure 3.13(b) for $Re = 275$.

Figure 3.13(c) and (d) present the population density distribution $N(u)$ of the longitudinal velocity component u in these two zones, computed along the entire
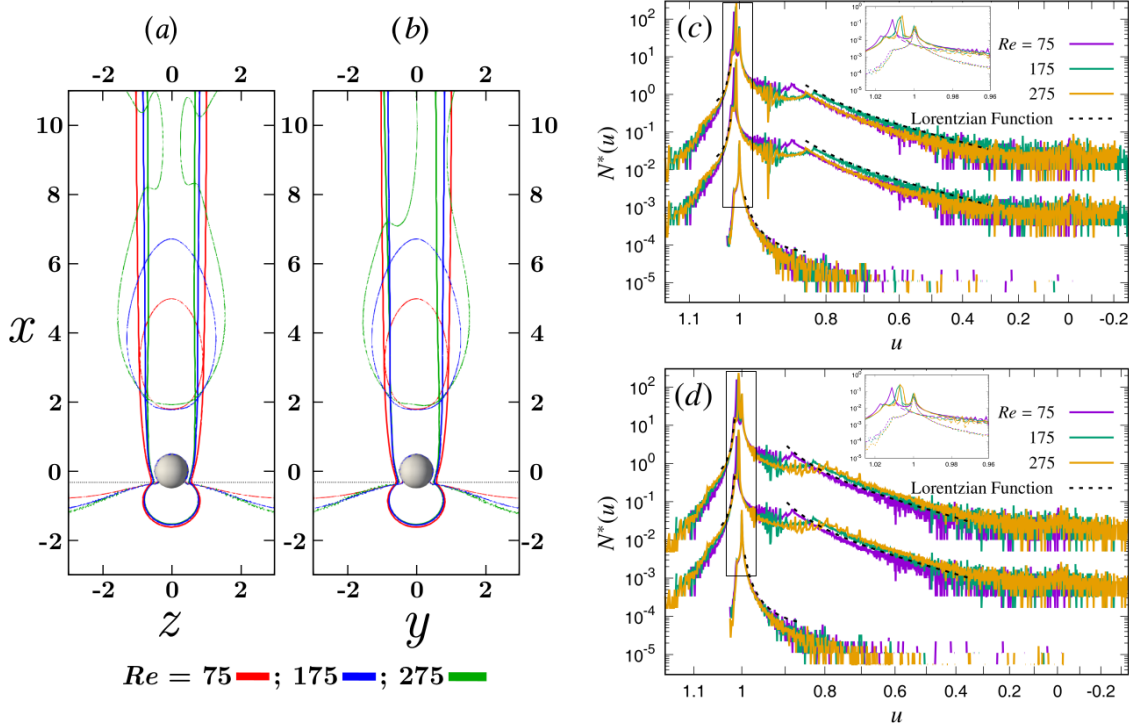
Figure 3.13: Distribution of the dimensionless streamwise velocity component u for various Re. $u = 0.95$ contours are drawn in solid lines along with $p = 0$ pressure contours in dashed thin lines along the orthogonal (*a*) (z, x) and (*b*) (y, x) planes. A horizontal dotted line at $x = -0.325$ is drawn to divide the upstream spatial structure of u from the downstream one. Normalized population density function $N^*(u) = N(u)/A$ (A is the area of the orthogonal plane) for the u sample population across the orthogonal (z, x) and (y, x) planes are plotted respectively in (*c*) and (*d*). $N^*(u)$ for the upstream, downstream and the entire planes are respectively plotted as the bottom, middle and the top sets of curves. A scale difference is created by amplifying the $N^*(u)$ of the downstream and the entire domain 30 and 900 times respectively. Sample extent in (*a,b*) is $[-3,3]d_p$ along the horizontal and $[-3,11]d_p$ along the vertical axes, whereas, in (*c,d*) it is $[-3.5,3.5]d_p$ along the horizontal and $[-5,20]d_p$ along the vertical axes.

orthogonal (z, x) and (y, x) planes of the computational domain, respectively. The distribution has been determined by dividing the range of u in 1000 bins, a resolution which allows for a smooth sample distribution while preserving its trend. In the upstream zone (bottom sets of curves in Figure 3.13(*c,d*)), $N(u)$ shows a sharp decrease in the population density as u decreases from the external ambient value of 1 towards the no-slip zero boundary condition at the sphere surface following a Lorentzian function, given in equation (3.10). Some sample population with $u \geq 1$

is also observed which resembles the region of highest velocity magnitudes near the $p \sim 0$ contour line. In order to create a visible scale separation, the $N(u)$ of the downstream zone is shifted for the middle set of curves in Figure 3.13(c,d). The negative values of velocity identify the recirculation zone behind the sphere. A large extent of the simulated wake can be well fitted by a Lorentzian distribution. The crescent like trend right after the ambient $u = 1$ is a result of the finite size of the simulation domain. Similar to the $N(u)$ of the upstream zone, some sample population with $u \geq 1$ is also observed in this downstream distribution, which are also coming from the $p \sim 0$ region. $N(u)$ of the entire plane is shifted for the top sets of curves in Figure 3.13(c,d) with an amplification of its original magnitudes. As plotted in the insets, the two highest peaks at $u \sim 1$ of the entire plane are the individual contributions from both the upstream and the downstream populations.

The Lorentzian or Cauchy-Lorentz distribution $y(u; A, u_c, b, y_0)$ is a single peak bell-shaped curve, defined as

$$y(u; A, u_c, b, y_0) \quad = \quad y_0 + 2 \, \frac{A}{\pi b} \, \frac{b^2}{4(u - u_c)^2 + b^2}, \tag{3.10}$$

where $y(u; A, u_c, b, y_0)$ is the population density of samples of variable u, A is its integral over all possible values of u, u_c is the position of its maximum where y takes the value $2A/(\pi b)$, with b being the width between its half maximums. Parameter y_0 is just an offset value, which allows for a non zero asymptotic limit of the Cauchy-Lorentz distribution. In the distribution of u, Figure 3.13(c,d), a Lorentzian trend is observed in the intermediate range, which corresponds to the boundary layer and to the region external to the wake. An increase in $N(u)$ is observed with increasing Reynolds numbers, indicating an increase in the dimensionless kinetic energy in this region. The out of plane tilting induced by the oblique wake at $Re = 275$ produces small spikes on top of an overall Lorentzian trend of the sample population along the (y, x) plane, as seen in Figure 3.13(d). However, the oblique wake regime retains a symmetric structure along the (z, x) plane in our simulations in Figure 3.13(c) but the out of plane tilting impacts the sample population. Therefore, $N(u)$ in Figure 3.13(c) for $Re = 275$ only indicates a lower yet a smooth Lorentzian trend.

The existence of such a trend in the distribution of a variable indicates the existence of a matching region where the variable shows an algebraic variation from the values in the wake to the values in the external ambient. If the flow is axisymmetric and the flow structures are elongated in the streamwise direction, this variation is in the radial direction proportional to $(y^2 + z^2)^{-1}$ (inverse of the square of the lateral distance from the axis). This algebraic matching region is not only present in the longitudinal velocity field, but also in the associated pressure field and in the passively transported scalars. In case of a purely diffusive scalar transport by a heated sphere, the one dimensional radial temperature profile decreases proportional to r^{-1} (r being the radial distance) away from the sphere surface. The temperature population in this case, therefore, would show a Lorentzian trend proportional to

the T^{-2} (T being the dimensionless temperature). Since in our low Re studies, the $\mathbf{u} \cdot \nabla\theta$ term in the NS equation is negligible outside the recirculating zone, the sample population shows almost a purely diffusive behavior. Therefore, this scalar distribution behavior is manifested as the Lorentzian trend proportional to θ^{-2} in the density distribution of the scalar θ population, which will be discussed later.
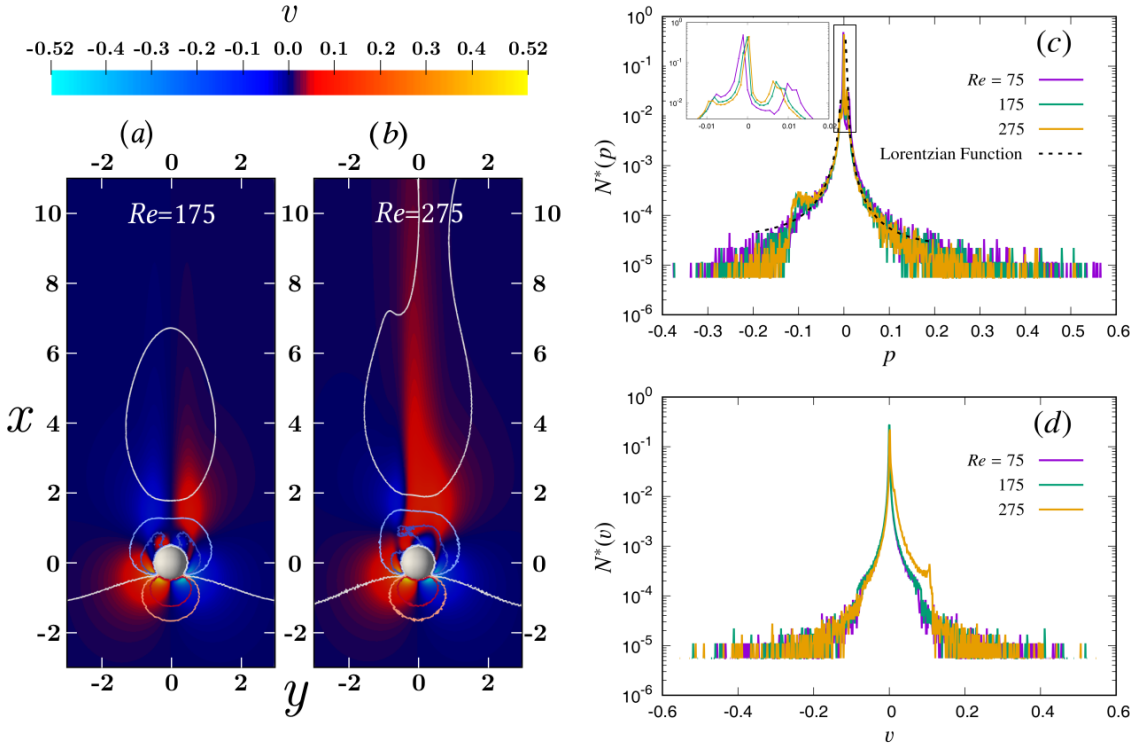
Figure 3.14: Distribution of the pressure p and velocity component v for various Re. Spatial distribution of v in color along with the contour lines of p at 0.1, 0.05, 0.0, -0.05, -0.1 magnitudes respectively in red, orange, white, cyan, and blue solid lines along the orthogonal (y, x) plane for the axisymmetric $Re = 175$ in (a) and for the oblique $Re = 275$ in (b). Normalized population density of pressure $N^*(p)$ across the entire orthogonal (y, x) central plane is plotted in (c), whereas $N^*(v)$ is plotted in (d). The sample extent is similar to Figure 3.13.

Figure 3.14 presents the spatial distribution of the pressure p and the transversal component of velocity v along the orthogonal (y, x) plane for various Re. In the axisymmetric regime, in Figure 3.14(a), the modulus of v is symmetric across the $y = 0$ plane but not the v. Similarly the modulus of w is also symmetric across the $z = 0$ plane in the axisymmetric regime, but not w. Complexity arises in the oblique regime, as neither p nor the modulus of v remains symmetric in the Figure 3.14(b). This is also seen in the population density distribution of v in Figure 3.14(d), where the positive magnitudes of v show dominance similar to

65

Figure 3.14(b). The transversal components of velocity v and w, however, do not show a Lorentzian distribution in its number density. It can be seen in Figure 3.14(a,b) that the population of v for the similar magnitudes is present in three different locations which resulted in non-Lorentzian evolution in the number density of the v and w (shown in Figure 3.14(c) for v). In contrast to v, the positive and negative magnitudes of p are rather concentrated near the sphere respectively in the upstream and the downstream zones as in Figure 3.14(a,b). Similar to Figure 3.13(c,d), the $N(p)$ of the upstream zone ($p \geq 0$ population) does not show significant variability with Re and exhibits a Lorentzian distribution. The $N(p)$ of the downstream zone however shows local peaks at around $p = -0.1$, which marks the discontinuity in the sample population in Figure 3.14(a,b).
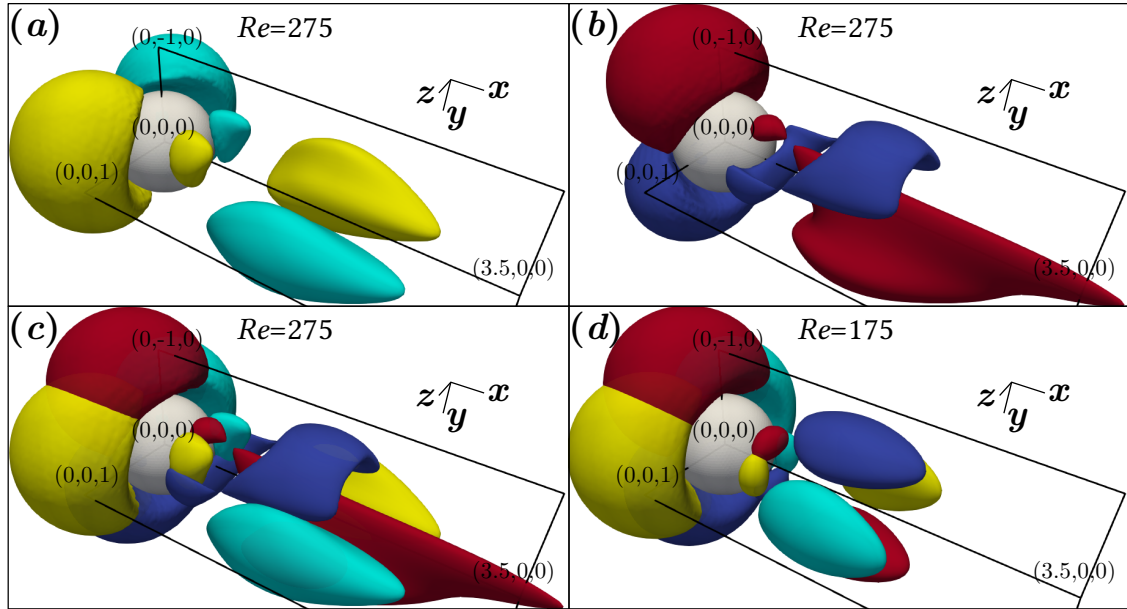
Figure 3.15: Three dimensional spatial structure of velocity components, v and w. The surface contours of $w = -0.06$ and 0.06 are plotted respectively in cyan and yellow in (a), and $v = -0.06$ and 0.06 contours are plotted respectively in blue and red in (b). (c) and (d) present both the v and w contours for the oblique $Re = 275$ and axisymmetric $Re = 175$ flow fields respectively.

A three dimensional spatial structure of the velocity components v and w for the oblique $Re = 275$ and the axisymmetric $Re = 175$ cases are shown in Figure 3.15, where the complexity in the oblique wake flow structure can be appreciated. The previously mentioned symmetry in the modulus of v and w is confirmed in Figure 3.15(d) for the steady axisymmetric flow with $Re = 175$; and the three different zones with similar magnitudes of v and w, both positive and negative, can also be seen. The transition to a complex flow structure for the steady oblique $Re = 275$ case is seen in Figure 3.15(a-c), where the spatial distributions of v and w show

differences. Despite the structural differences, both the v and w populations are symmetric along the (z, x) planes but non-symmetric along the (y, x) planes, which is typical of the steady oblique regime.

3.3.2   Spatial Structure of the Transported Scalars
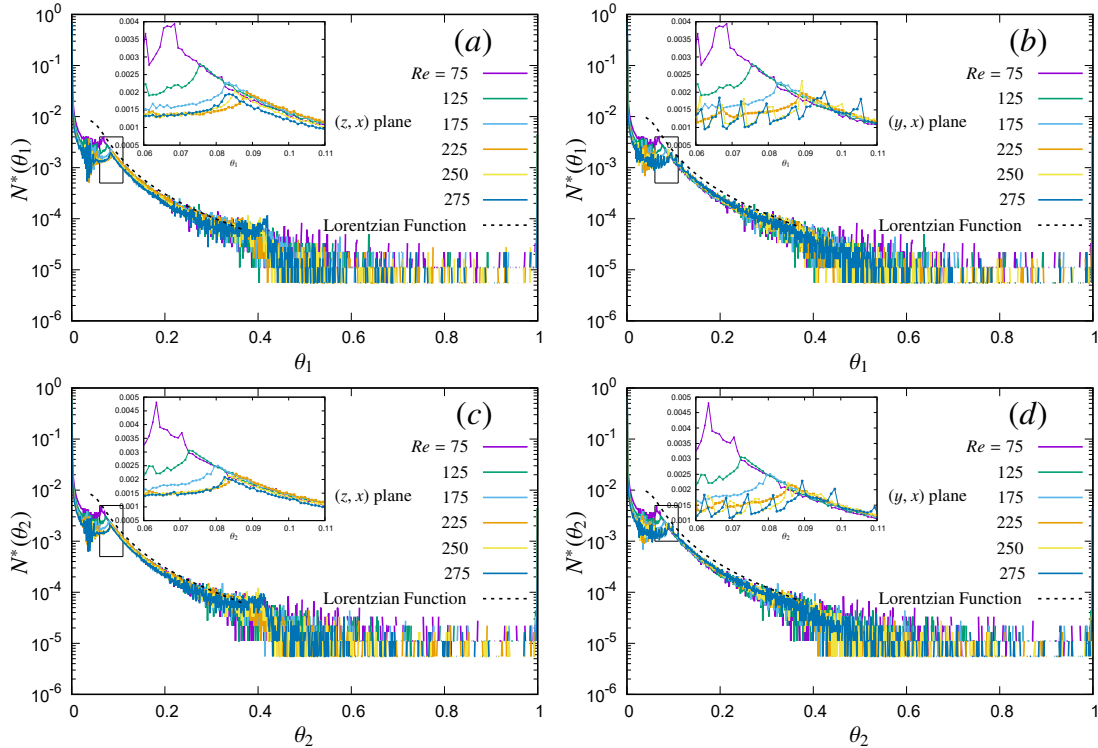
Figure 3.16: Spatial evolution of the normalized population density of scalar $N^*(\theta_1)$ along the (z, x) plane is presented in (a) and along the (y, x) plane in (b). Evolution $N^*(\theta_2)$ along the (z, x) plane is plotted in (c) and along the (y, x) plane in (d). These orthogonal planes pass through the center of the sphere and extends to the entire simulated domain of $[-3.5, 3.5]d_p$ in the horizontal y, z, and $[-5, 20]d_p$ in the streamwise x directions.

Figure 3.16 presents the population density distribution of the scalar fields $N(\theta_1)$ and $N(\theta_2)$ across two central orthogonal planes (z, x) and (y, x) (similar to the previous Figures). Since the boundary conditions for the dimensionless scalars have a zero value in the ambient and a unit value on the sphere surface, their population density distribution shows the highest population around zero in Figure 3.16, followed by a domain induced crescent zone, and then a Lorentzian distribution in the intermediate values gradually approaching the surface unit value. The Lorentzian trend is again visible in the scalar population density, due to the similitude of

67

the advection-diffusion equation for the scalars to the dynamics of momentum in regions with small pressure gradients. In the upstream region, the behaviour of velocity and scalars is very different due to the strong pressure gradient, while in the downstream region the difference is much milder. A closer look to the density distributions in the insets show that the steady axisymmetric cases do not show a well distinguishable difference in the number density at different scalar magnitudes with the increase in Re, but only the threshold magnitude for the start of the Lorentzian trend increases. The shift in the threshold of Lorentzian trend is attributed due to the finite and a similar size of the simulation domain for all the Re cases and due to the shrink in the lateral extent of the wake but a stretch in the streamwise direction with increasing Re. The similar Lorentzian trend however for different Re indicates that the integral of the scalar concentration does not significantly change irrespective of its Re in an infinitely large domain. The decrease in the sample population for the oblique cases in the left panel of Figure 3.16 for the orthogonal (z,x) plane is however due to the out of plane tilt of the wake which reduces the sample population. Whereas in the right panel for the orthogonal (y,x) plane, a step-wise perturbation on top of an overall Lorentzian trend is seen in the oblique wake regime as a result of its tilt in this plane.

In order to understand further the descriptive statistics of the transported fluid and the scalar populations in the steady wake of the sphere, a comparison in the quartiles of the population is presented in Figure 3.17. Since the ambient population dilutes such statistics, the sampling volume is chosen to confine near the wake zone with a volume of $[-1,10]d_p \times [-1,1]d_p \times [-1,1]d_p$. All the quartiles for the flow and the scalars are normalized with its value at the $Re = 25$. For example, the Q3 of $\tilde{u}$ is the ratio of the Q3 of u and the Q3 of u for $Re = 25$. The plots of $\tilde{u}$, $\tilde{\theta}_1$ and $\tilde{\theta}_2$ in Figure 3.17(a,c,d) do not show a minimum, since the minimum of these quantities goes to zero. From Figure 3.17(a), it is seen that the quartiles increases with the Re. This is in line with the thinning of the boundary layer, the shrinking of the wake in the lateral extent, and an elongation in the streamwise extent with Re, which increases the fluid velocity inside the sampling volume with an increment in Re. The change from the steady axisymmetric to the steady oblique regime is only witnessed in the trend of the maximum of $\tilde{u}$ in Figure 3.17(a). In regards to the other quantities in Figure 3.17(b,c,d), overall a decrease is observed in all the quartiles. This is also typical since the ambient magnitudes for all these quantities are zero, which increase in number density inside the sample volume when Re increases. Therefore, for the $\tilde{\theta}_1$ and $\tilde{\theta}_2$ quartiles in Figure 3.17(c,d), the ambient flow is observed to play a higher amount of influence in the sample populations with the increment in Re.

Figure 3.18 presents the spatial distribution of the convective scalar flux $\dot{Q}$ in the streamwise direction x. $\dot{Q}$ is a product between θ and u. Spatial distribution of $\dot{Q}$ along the orthogonal (y,x) plane in Figure 3.18(a,b) is someway different from the other flow quantities, since it shows highest positive $\dot{Q}$ in the boundary layers
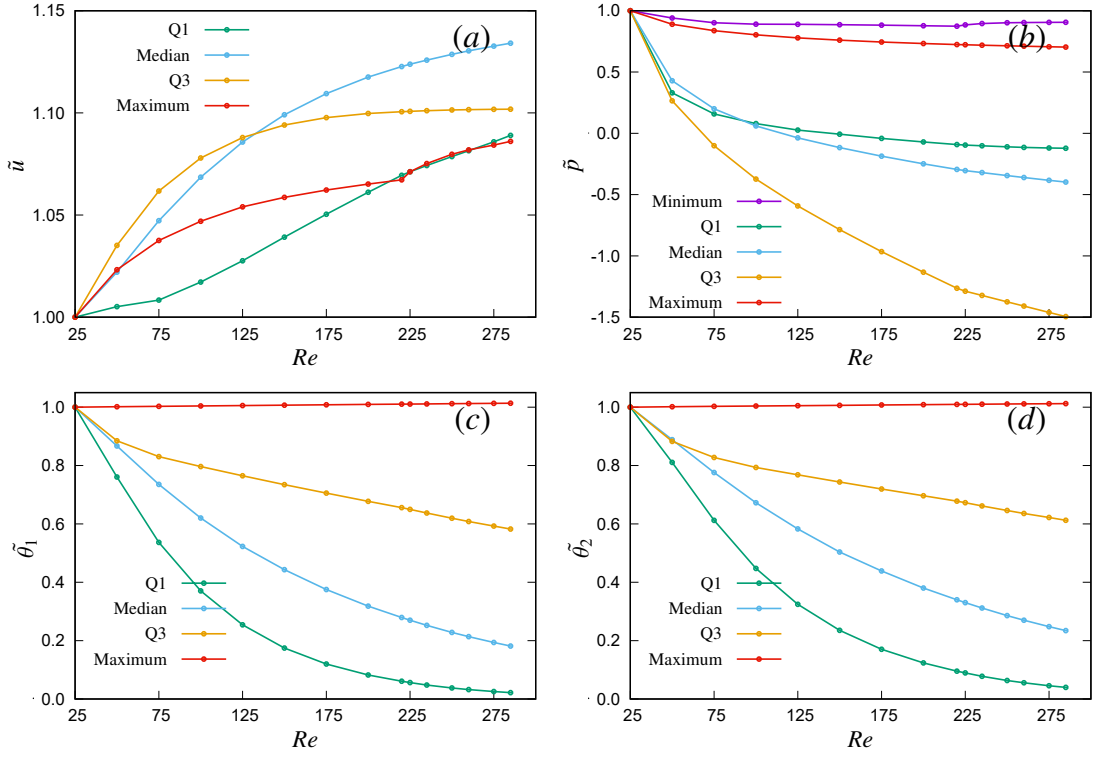
Figure 3.17: Evolution of the fluid and scalar quantities for various steady Re in a $[-1,10]d_p \times [-1,1]d_p \times [-1,1]d_p$ sampling volume. The box plot quantities, such as, minimum, Q1, median, Q3, and maximum, are presented for the streamwise component of fluid velocity u, pressure p and the scalars θ_1 and θ_2. A normalization ($\sim$) is done on each quantity by its magnitude at $Re = 25$, so that all the quantities are 1.0 at the $Re = 25$.

and a negative $\dot{Q}$ in the recirculating zone due to negative u. The non-symmetric spatial structure of the oblique ($Re = 275$) scalar flux is visible in Figure 3.18(b). The population density distribution $N(\dot{Q})$ along the orthogonal (z, x) and (y, x) planes shows a different structure as expected. A Lorentzian trend is observed for a few limited sample populations, for example, for the samples between the white and pink contour lines in Figure 3.18(a) and (b) respectively for $Re = 175$ and 275. These two contour lines correspond to the $\dot{Q}$ magnitudes from Figure 3.18(d) marking the beginning and the end of the Lorentzian trend for each individual Re. Overall an increase in the sample population of $\dot{Q}$ is observed with increasing Re within the zone with Lorentzian distribution. This indicates the expected increase in the dimensionless convective transport with higher Re.
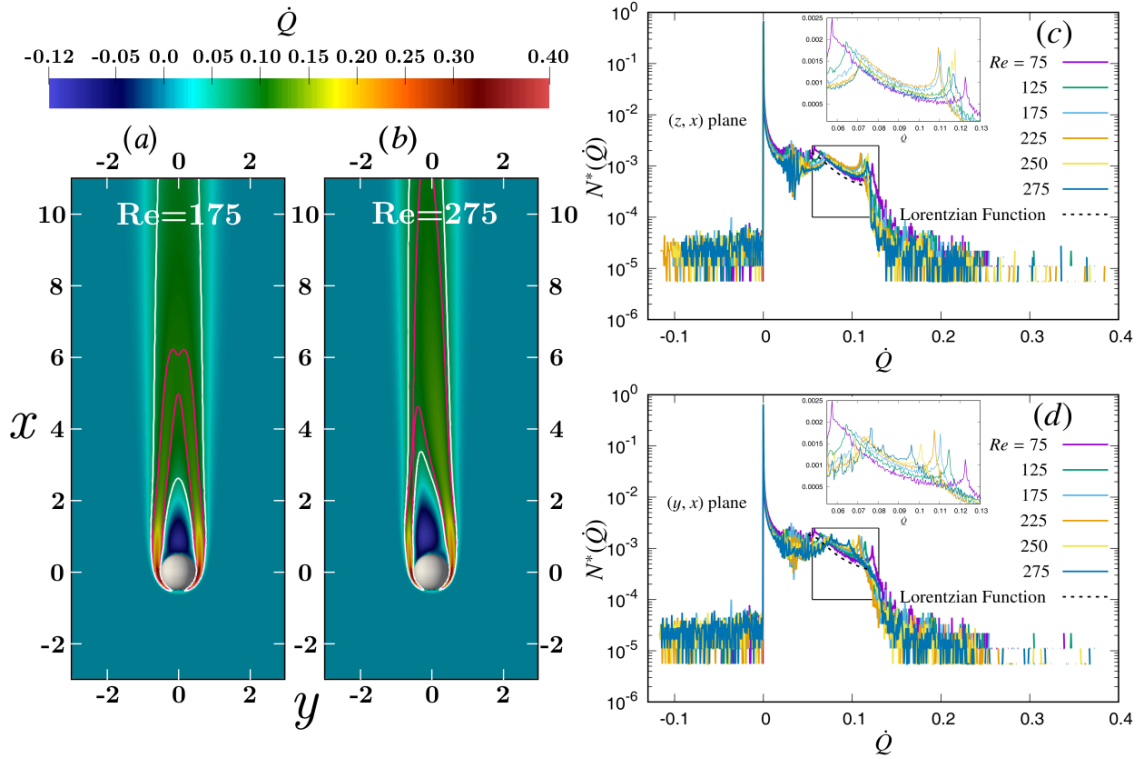
Figure 3.18: Spatial distribution of convective scalar flux $\dot{Q} = u \cdot \theta_1$ for various Re. Spatial distribution of $\dot{Q}$ in color along the orthogonal (y, x) plane for the axisymmetric $Re = 175$ in (a) and for the oblique $Re = 275$ in (b). The white contour lines represent $\dot{Q} = 0.069$ in (a) and $\dot{Q} = 0.077$ in (b), while the pink contour lines are at $\dot{Q} = 0.11$ in (a) and $\dot{Q} = 0.096$ in (b) respectively. Normalized population density of convective scalar flux $N^*(\dot{Q})$ across the entire orthogonal (z, x) and (y, x) central planes are plotted respectively in (c) and (d). The sample extent is similar to Figure 3.13.

3.4   Summary and Conclusions

A detailed numerical analysis on the spatial structure of the wake flow using population density distribution is presented for the various Reynolds number in the steady wake regime. The incompressible Navier-Stokes equation is solved for the flow velocity and the one-way coupled advection-diffusion equations are solved for the scalars using the Lattice Boltzmann Method (LBM). The spatial evolution of various flow quantities, such as, longitudinal velocity component u, pressure p, passive scalar θ, convective scalar flux $\dot{Q}$ in the wake of the steady axisymmetric regime ($Re \leq 220$) and the oblique regime ($225 \leq Re \leq 285$) using a population distribution function N, shows a Lorentzian distribution which is proportional to the inverse of the square of the flow quantity (for example, $N(p) \propto p^{-2}$). This

Lorentzian trend exhibits an algebraic decay in the number density of populations with different magnitudes of fluid quantities from the external ambient to the boundary layer in the wake and dominates the spatial distribution of the flow quantities outside the recirculating region. However, the transversal components of fluid velocity, v and w, show a different spatial distribution, which is not attributable to a Lorentzian one. Transition to the oblique wake regime at $Re \geq 225$ in our simulations shows a complex three dimensional spatial evolution of the flow quantities, which also shows a Lorentzian trend. The population density distribution for the longitudinal velocity component u, shows an increase in its number density with increasing Re, evidencing an increase in the dimensionless kinetic energy. Whereas the number density of the scalar populations remains the same for various steady axisymmetric Re. This feature however changes in case of the convective scalar flux, where an increase is observed in its number density with the increase in Re.

Descriptive statistics in the form of population density distribution of the fluid velocity and the transported scalar quantities in the wake of a sphere is important for understanding the transport and local reaction processes in specific regions of the wake. This will be used in the next Chapter 4 for understanding the microphysics of precipitating large cloud hydrometeors and the cloud aerosol interactions in the wake of such hydrometeors. However, this approach should also find applications in engineering flows e.g. in which droplets interact with their environment.

End of Chapter 3

Chapter 4

Aerosol Activation by Precipitating Hydrometeors

A part of this chapter is already published in Bhowmick, T., Wang, Y., Iovieno, M., Bagheri, G. and Bodenschatz, E. (2020), "Supersaturation in the Wake of a Precipitating Hydrometeor and Its Impact on Aerosol Activation", Geophysical Research Letters, volume 47, issue 22, article number e2020GL091179 [11]. Whether the large precipitating cloud hydrometeors activate cloud aerosols in its wake, and how does such activation happen and whether this process impacts the cloud life cycle, are the three open scientific questions which are investigated in this chapter. An in-depth and comprehensive numerical study is conducted for this purpose, which varies over a wide range of parameter space relevant for the atmospheric cloud conditions. The influences of the ambient humidity and the ambient/hydrometeor temperatures on the supersaturation within the wake for different sizes and phases of spherical hydrometeors are investigated. Then, with the Lagrangian tracking of aerosols as passive tracers around such sedimenting hydrometeors, the residence time and the supersaturation experienced by individual aerosols as a function of the governing parameters are also quantified. Finally, these results are used to approximate the likelihood and the significance of heterogeneous wake-induced nucleation in the atmospheric clouds. An adaptation of the numerical methods and computational details from the Chapter 3 are described in Section 4.1 along with the basic underlying hypothesis. Results are presented and discussed in Section 4.2, which includes the visualization and quantification of the wake-induced supersaturation behind cloud hydrometeors varying over a large range of parameter space. Then a quantitative investigation is conducted using the Lagrangian tracers to compute the residence time and the supersaturation experience of each aerosols for the same range of parameters. Based on the quantitative results, in section 4.3, whether and when an aerosol can activate in the wake-induced supersaturation is approximated and its impact on the cloud life cycle is assessed. A summary and conclusions is provided in Section 4.4.

4.1   Basic Hypothesis and Numerical Details

In this section, an overview of the basic hypothesis is detailed, which are important for the selection of the physical model and the numerical setup for the simulations. Furthermore, an adaptation of the numerical methods from the Chapter 3 section 3.2 is also presented for understanding the aerosol activation in the wake of the precipitating hydrometeors.

4.1.1   Hypothesis on Hydrometeor Size and Temperature

In a supersaturated or subsaturated ambient, a hydrometeor changes its size due to evaporation/condensation. The mass change of a spherical hydrometeor due water vapor diffusion on its surface is given as:

$$\frac{\mathrm{d}m_p}{\mathrm{d}t} = 4\pi r_p^2 \rho_w \frac{\mathrm{d}r_p}{\mathrm{d}t} = \int_p \kappa_v \nabla \rho_v \cdot \mathbf{n}\, \mathrm{d}\sigma, \tag{4.1}$$

where, m_p is the mass of the hydrometeor, r_p is its radius, ρ_w is the density of liquid water, κ_v is the diffusivity of water vapor in air, ρ_v is the density of water vapor, $\mathbf{n}$ is the unit normal vector to the hydrometeor surface, and the integral is over the surface p of the hydrometeor and $\mathrm{d}\sigma$ is the infinitesimal surface area.

The evaporation/condensation of water vapor leads to the absorption/release of the latent heat due to phase change. Therefore, the enthalpy of the hydrometeor changes according to the following equation:

$$m_p c_{p,w} \frac{\mathrm{d}T_p}{\mathrm{d}t} = -L\frac{\mathrm{d}m_p}{\mathrm{d}t} + c_{p,w}(T_p - T_0)\frac{\mathrm{d}m_p}{\mathrm{d}t} + \int_p \lambda_T \nabla T \cdot \mathbf{n}\, \mathrm{d}\sigma, \tag{4.2}$$

where, $c_{p,w}$ is the specific heat of water at constant pressure, T_p is the hydrometeor surface temperature, L is the latent heat for phase change, T_0 is a reference temperature (here assumed to be $0\,°\mathrm{C}$), $\lambda_T = \kappa \rho_a c_{p,a}$ is the thermal conductivity of air, κ is the thermal diffusivity, ρ_a is the density of air, $c_{p,a}$ is the specific heat of air at constant pressure. The first term on the right hand side of the equation (4.2) represents the heat released or absorbed by the water undergoing phase change. The second term represents the change in the hydrometeor enthalpy due to its size variation. And the third term is due to the diffusive heat transfer. Since our aim is to estimate the timescales of the hydrometeor size and temperature variation, one can ignore the second term in the right hand side by considering $L \gg c_{p,w}(T_p - T_0)$. The remaining two terms will be called $m_p c_{p,w}(\mathrm{d}T_p/\mathrm{d}t)_L$ and $m_p c_{p,w}(\mathrm{d}T_p/\mathrm{d}t)_{\dot{Q}}$, respectively for the latent and diffusive heat transfer in the process of condensation/evaporation of water mass.

One can evaluate the diffusion of water vapor and heat (the last terms in equations (4.1) and (4.2)) from a precipitating hydrometeor, from its dimensionless

Reynolds Re, Prandtl Pr, Schmidt Sc, and Nußelt Nu numbers,

$$Re = \frac{d_p U_p}{\nu}, \qquad Pr = \frac{\nu}{\kappa}, \qquad Sc = \frac{\nu}{\kappa_v}, \qquad Nu = \frac{\dot{Q}}{4\pi\lambda_T(T_\infty - T_p)r_p}.$$

Here, d_p is the hydrometeor diameter, ν is the kinematic viscosity, U_p is the terminal velocity and $\dot{Q}$ is the convective heat flux at the hydrometeor surface. In the range of the simulated Reynolds and Prandtl numbers of this chapter, the Nu can be estimated from the empirical equations in Michaelides (2006) [96] as:

$$Nu(Re, Pr) = 1 + 0.752 \left(1 + \frac{1}{Re\,Pr}\right)^{1/3} Re^{0.472} Pr^{1/3}.$$

Therefore, that one can write the heat flux as:

$$\dot{Q} \simeq \int_p \lambda_T \nabla T \cdot \mathbf{n}\,\mathrm{d}\sigma = 4\pi Nu(Re, Pr)\lambda_T(T_\infty - T_p)r_p. \tag{4.3}$$

Since both temperature and water vapor are governed by the same passive scalar equations (4.13) and (4.14), the only difference lays in their diffusivities, i.e. Pr is replace by Sc. Since $Pr \sim Sc$, one can use the same correlation between the vapor mass flow and Reynolds number, so that:

$$\frac{\mathrm{d}m_p}{dt} = \int_p \kappa_v \nabla\rho_v \cdot \mathbf{n}\,\mathrm{d}\sigma \simeq 4\pi Nu(Re, Sc)\kappa_v(\rho_{v,\infty} - \rho_{v,p})r_p, \tag{4.4}$$

where, $\rho_{v,p}$ is the saturated vapor density at the hydrometeor surface at temperature T_p. And the T_∞ and $\rho_{v,\infty}$ are the ambient temperature and ambient water vapor density respectively.

Therefore, the timescale τ_R for changes in the size and the timescales $\tau_{\dot{Q}}$ and τ_L of the surface temperature change due to the convective heat transfer and due to the latent heat release/absorption can be estimated as:

$$\tau_R \sim \frac{r_p}{\mathrm{d}r_p/\mathrm{d}t} \sim \frac{\rho_w r_p^2}{Nu(Re, Sc)\kappa_v(\rho_{v,\infty} - \rho_{v,p})}, \tag{4.5}$$

$$\tau_{\dot{Q}} \sim \frac{T_p - T_\infty}{(\mathrm{d}T_p/\mathrm{d}t)_{\dot{Q}}} \sim \frac{\rho_w c_{p,w} r_p^2}{3Nu(Re, Pr)\lambda_T}, \tag{4.6}$$

$$\tau_L \sim \frac{T_p - T_\infty}{(\mathrm{d}T_p/\mathrm{d}t)_L} \sim \frac{\rho_w c_{p,w}(T_p - T_\infty)r_p^2}{3Nu(Re, Sc)L\kappa_v(\rho_{v,\infty} - \rho_{v,p})}. \tag{4.7}$$

These scale should be compared with the pass-through time τ_A of an aerosol around the hydrometeor, which is given by:

$$\tau_A \sim \frac{\pi r_p}{U_{avg}} \sim \frac{2\pi r_p}{U_p}. \tag{4.8}$$
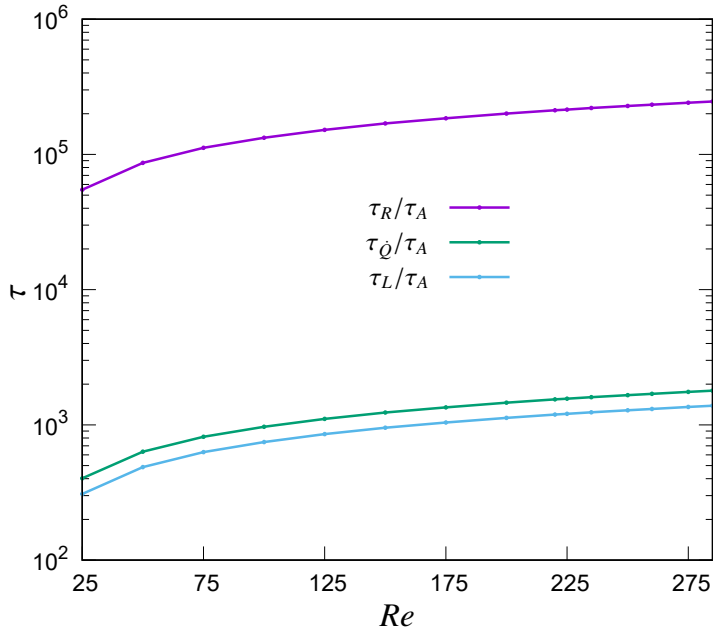
Figure 4.1: Evolution of various normalized timescales (normalized with τ_A) with respect to the hydrometeor Re, considering water droplets are settling down at its terminal velocity.

This gives a measure of the time span in which an aerosol interacts with the vapor and temperature fields, that are perturbed by the hydrometeor. The ratios τ_R/τ_A, $\tau_{\dot{Q}}/\tau_A$ and τ_L/τ_A depend on the Reynolds, Prandtl and Schmidt numbers, and the ratios of the density and specific heats only.

The evolution of these timescales in Figure 4.1 shows such ratios as a function of the Reynolds number. The atmospheric conditions are represented with $Pr = 0.71$, $Sc = 0.61$, $\rho_w = 10^3 \, \text{kg m}^{-3}$, $\kappa_v = 2.394 \times 10^{-5} \, \text{m}^2 \, \text{s}^{-1}$, $\lambda_T = 2.44 \times 10^{-2} \, \text{J K}^{-1} \, \text{m}^{-1} \, \text{s}^{-1}$, $L = 2.5 \times 10^6 \, \text{J kg}^{-1}$, $c_{p,w} = 4217.6 \, \text{J kg}^{-1} \, \text{K}^{-1}$ [9]. The velocity U_p of the hydrometeor is chosen to match the asymptotic free fall velocity, given by the equilibrium between its weight and the drag. For this timescale analysis, the cloud droplets of size up to $1 \, \text{mm}$ is chosen, which is the typical size of large rain drops [116]. Therefore, the resulting Reynolds numbers is up to around 300. For this timescale analysis, a water hydrometeor with a surface temperature T_p equal to $10\,°\text{C}$ is considered in an ambient with a temperature T_∞ equal to $0\,°\text{C}$ and with an ambient relative humidity equal to 80% with respect to the liquid water phase.

It can be seen that all the timescales are several order of magnitude larger than τ_A, so that the variation of the hydrometeor size and temperature is negligible during the pass-through time of an aerosol. It should also be noticed that this conclusion does not change for the trapping of the 'lucky' aerosols in the supersaturated wake, which will be discussed later in this chapter. This is due to the

fact that their residence time is in the order of $10^2\tau_A$, while τ_R, $\tau_{\dot{Q}}$ and τ_L are all in excess of $10^3\tau_A$. This implies that it is possible to neglect the variation of the hydrometeor diameter and its surface temperature in the solution of the Navier-Stokes equations together with the one-way coupled advection-diffusion equations for the temperature and the density of water vapor.

4.1.2   Impact of Buoyancy on Momentum Balance

The relative significance of the buoyancy force in the momentum balance equation is governed by another non-dimensional number, the Richardson number Ri, which can be decomposed into two parts as reported by Chouippe et al. (2019) [20]: a temperature Richardson number Ri_T and a vapor density Richardson number Ri_{ρ_v}, defined as

$$Ri_T = \frac{T_p - T_\infty}{T_\infty + 273.15} \frac{1}{\rho_p/\rho_f - 1}, \tag{4.9}$$

$$Ri_{\rho_v} = \frac{\rho_{v,p} - \rho_{v,\infty}}{\rho_f} \frac{\mathcal{M}_p - \mathcal{M}_f}{\mathcal{M}_p} \frac{1}{\rho_p/\rho_f - 1}. \tag{4.10}$$

Here ρ_p is the density of the hydrometeors which is water in this case, and ρ_f is the density of the ambient fluid which is air in this case. $\mathcal{M}_p$ is the molar mass of the constituent fluid of the hydrometeor which is water in our case, and $\mathcal{M}_f$ is the molar mass of the fluid which is air.

For the assumed 10°C temperature difference as specified previously, and for the ambient at a 20% subsaturation condition, one gets $Ri_T = \mathcal{O}(10^{-5})$ and $Ri_{\rho_v} = \mathcal{O}(10^{-6})$. Therefore, the buoyancy force $B = g\,Ri \simeq \mathcal{O}(10^{-5})g$, which leaves negligible impact on the momentum balance equation (see also Kotouč et al. (2009) [70] and Chouippe et al. (2019) [20] for details).

4.1.3   Equations for Solving the Flow Field

The flow around a falling spherical hydrometeor is resolved numerically. Since the timescales of temperature and size variation of the hydrometeor are much larger than the flow timescales, the temperature and the radius of the hydrometeor are assumed constant. Therefore, the hydrometeor is modeled in our setup as a sphere of constant diameter d_p at temperature T_p. While the ambient air is flowing around it at the terminal velocity U_p of the hydrometeor. The deformation in the shape of the hydrometeor is also ignored in our simulations as a result of the aerodynamic forces, which do not deform the cloud droplets of $\sim 1\,\mathrm{mm}$ size range significantly [116]. If one uses d_p as a length scale, U_p as a velocity scale, and the differences in the temperature and the vapor density between the sphere and its surroundings as a scale for the variations in the temperature and the water vapor density, one

obtains the following dimensionless quantities:

$$\mathbf{x}^* = \frac{\mathbf{x}}{d_p}, \quad t^* = \frac{tU_p}{d_p}, \quad \mathbf{u}^* = \frac{\mathbf{u}}{U_p}, \quad T^* = \frac{T - T_\infty}{T_p - T_\infty}, \quad \rho_v^* = \frac{\rho_v - \rho_{v,\infty}}{\rho_{v,p} - \rho_{v,\infty}}.$$

The dimensionless incompressible Navier-Stokes equations and the one-way coupled Advection-Diffusion (AD) equations for the temperature and water vapor density are, therefore (see also the Section 3.2 in Chapter 3 for details):

$$\nabla \cdot \mathbf{u} = 0, \tag{4.11}$$

$$\frac{\partial \mathbf{u}}{\partial t} + \mathbf{u} \cdot \nabla \mathbf{u} = -\nabla p + \frac{1}{Re}\nabla^2 \mathbf{u},, \tag{4.12}$$

$$\frac{\partial T}{\partial t} + \mathbf{u} \cdot \nabla T = \frac{1}{Re\,Pr}\nabla^2 T, \tag{4.13}$$

$$\frac{\partial \rho_v}{\partial t} + \mathbf{u} \cdot \nabla \rho_v = \frac{1}{Re\,Sc}\nabla^2 \rho_v. \tag{4.14}$$

The * symbol has been omitted from all dimensionless variables for the sake of clarity. Here p is the dimensionless pressure $(p - p_\infty)/\rho_a U_p^2$, $Re = U_p d_p/\nu$ is the Reynolds number (with ν being the kinematic viscosity of air), $Pr = \nu/\kappa$ is the Prandtl number (with κ being the thermal diffusivity of air), $Sc = \nu/\kappa_v$ is the Schmidt number (with κ_v being the water vapor diffusivity). Neither the buoyancy feedback nor the influence of the temperature, the water vapor density and the humid air on the wake [70] are considered, as this is also modeled by Krayer et al. (2020) [72].

These model equations are solved with the lattice Boltzmann method (LBM) [136, 74, 141], which is implemented by the open-source LBM library Palabos [83], using the BGK collision operator [117]. For solving the fluid velocity field, the D3Q19 lattice is chosen because non-linear momentum advection corrections are not very significant for steady axisymmetric or oblique wake flows [133] with low Reynolds number. The scalar fields T and ρ_v are resolved with the D3Q7 lattice, since only the zeroth and the first moments of the discrete scalar concentrations at the lattice nodes are important for recovering the AD equations from the LBM equation [74].

The reference frame has its origin in the center of the spherical hydrometeor. Three-dimensional computational domain extends 5 diameters upstream and 20 diameters downstream, while in the transversal directions it is 7 diameters wide, i.e. the domain is $[-5,20]d_p \times [-3.5,3.5]d_p \times [-3.5,3.5]d_p$ in size. The domain is discretized with a uniform Cartesian mesh with a grid size equal to $d_p/32$ (i.e. for each length of d_p, 32 lattices are assigned in each direction). Tests in Chapter 3 have shown the mesh and domain independence for the flow around the hydrometeor. Dirichlet and Neumann conditions are considered for the inlet and outlet boundaries, respectively. For the lateral boundaries in transversal directions, periodic boundary conditions are applied. The surface of the hydrometeor is no-slip

at zero velocity and with a constant T and ρ_v at a fixed temperature ($T = \rho_v = 1$ in dimensionless form). According to the Maxwell diffusion model, the vapor density ρ_v adjacent to the solid or liquid surface layer of the hydrometeor is always saturated at the hydrometeor surface temperature T_p. The empirical equations of Huang (2018) [57] are used to determine the saturated vapor density $\rho_{vs}(T)$,

$$
\rho_{vs}(T) = \begin{cases} \dfrac{1}{R_v(T+273.15)} \dfrac{\exp(34.494 - 4924.99/(T+237.1))}{(T+105)^{1.57}}, & \text{if } T > 0\,^{\circ}\text{C} \\ \dfrac{1}{R_v(T+273.15)} \dfrac{\exp(43.494 - 6545.8/(T+278))}{(T+868)^2}. & \text{if } T \le 0\,^{\circ}\text{C} \end{cases}
$$

(4.15)

A second order extrapolation scheme [48] is adopted for the boundary conditions on the curved boundary of the hydrometeor. The numerical setup was validated by comparing the drag coefficient, the length of the recirculating zone and the angle of separation with existing researches, e.g. [66], for the fluid velocity field, as detailed in Chapter 3. For example, the drag coefficient deviates from the empirical equations [23] the maximum at $Re = 25$, which is 3.5%, and is reduced with higher Re, so that at $Re = 200$ it is less than 1% . The temperature field was validated by comparing the normalized temperature profiles with similar Pr simulation results, e.g. [20], for various Re. Equations (4.15) are used to reconstruct the supersaturation field $S = RH - 1 = \rho_v/\rho_{vs}(T) - 1$ around the sphere from the solution of the AD equations.

4.2 Supersaturation in the Wake and Its Impact

The flow at different Reynolds numbers in the steady axisymmetric wake ($0 \le Re \le 220$) and in the steady oblique wake ($225 \le Re \le 285$) (see [66], and [142]), with $Pr = 0.71$ and $Sc = 0.61$ according to the values of the atmospheric standard conditions [100, 96] is analyzed. In the case of a liquid hydrometeor of density $10^3\,\text{kg}\,\text{m}^{-3}$, this corresponds to a particle with a diameter between $3 \times 10^{-4}\,\text{m}$ and $1.03 \times 10^{-3}\,\text{m}$ falling with terminal velocities between $1.21\,\text{m}\,\text{s}^{-1}$ and $4.03\,\text{m}\,\text{s}^{-1}$. The ambient relative humidity RH_∞ is varied from nearly saturated ($RH_\infty \sim 100\%$) within the cloud [128] to a highly subsaturated in the open atmosphere [115]. The supersaturation $S = RH - 1 = \rho_v/\rho_{vs}(T) - 1$ is computed with respect to the water phase when $T > 0\,^{\circ}\text{C}$ and with respect to the ice phase when $T \le 0\,^{\circ}\text{C}$ by using the empirical equations (4.15) for liquid and frozen hydrometeors respectively [57].

One can identify each simulations with a defined nomenclature, like for example, 'LC 0 15 90'. Here the first letter indicates the hydrometeor phase (L liquid or I ice), the second letter indicates the sign of the temperature difference between the hydrometeor and the ambient (W warmer hydrometeor or C colder hydrometeor), and the three following numbers give the hydrometeor temperature T_p (in degrees
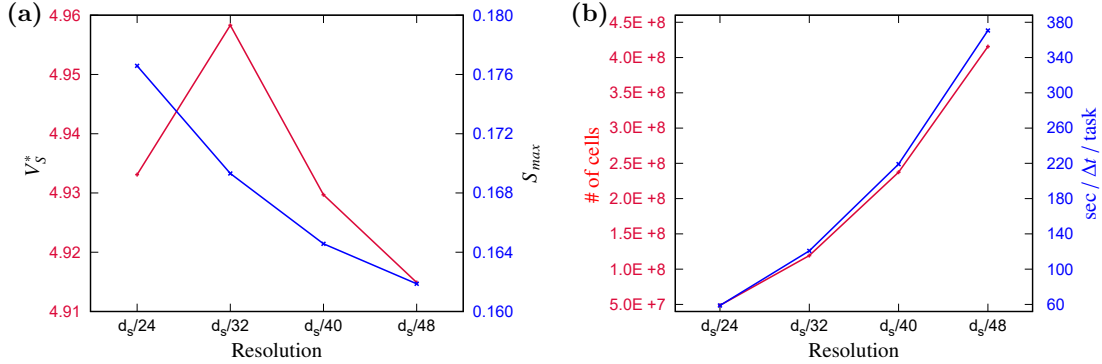
Figure 4.2: Mesh independence test: (a) Normalized supersaturated volume $V_S^* = V_S/(\pi d_p^3/6)$ and the supersaturation maximum S_{max}, and (b) the total number of lattice nodes and the computational time for the various spatial resolutions of the mesh at $Re = 200$ for the thermodynamics setup of 'LW 4 19 90'. 'LW 4 19 90' represents a (L) liquid but (W) warmer hydrometeor with a surface temperature (4) $T_p = 4\,°C$ in an ambient at $T_\infty = -15\,°C$, which gives a (19) $\Delta T = 19\,°C$ of temperature difference. And the (60) indicates the ambient RH condition $RH_\infty = 60\%$ with respect to the ice phase.

Celsius), the modulus of $T_p - T_\infty$ referred as ΔT (in degrees Celsius) and the ambient relative humidity RH_∞ (in %). Thus, 'LC 0 15 90' is a liquid hydrometeor colder than the ambient, with a surface temperature of $0\,°C$ in an ambient air with a temperature of $15\,°C$ and a relative humidity equal to 90%.

Figure 4.2(a) presents the mesh independence test considering the supersaturation parameters, such as, the supersaturated volume V_S, which is the measure of the volume with $S > 0$ and the maximum supersaturation S_{max}, which are computed with respect to the ice phase in this case of 'LW 4 19 90', obtained with different mesh spatial resolutions, including $d_p/24$, $d_p/32$, $d_p/40$ and $d_p/48$, in a simulation domain size of $[-5,35]d_p \times [-5,5]d_p \times [-5,5]d_p$ for the $Re = 200$ simulation. A comparison in the total number of lattice nodes and the computational time is also provided in Figure 4.2(b). It can be seen that the V_S and the S_{max} show negligible difference for the grid size of $d_p/32$ and lower, with a variation up to 1% for the V_S and up to 4% for the S_{max}. Therefore, considering a non-linear increase in the computational load due to the higher resolution with respect to the negligible gain in the accuracy, the resolution with $d_p/32$ grid size is chosen for this study.

Figure 4.3 presents the domain lateral extent independence test, where the lateral extent of the domain is varied from $[-5,5]d_p \times [-5,5]d_p$ to $[-3.5,3.5]d_p \times [-3.5,3.5]d_p$ keeping the streamwise extent a constant at $[-5,35]d_p$ in length. In the plot of V_S and S_{max} in Figure 4.3(a), a negligible variation up to 1.7% is visible, which proves that the transversal extent independence in the computation of the supersaturaion quantities for a domain with lateral extent of $[-3.5,3.5]d_p \times$
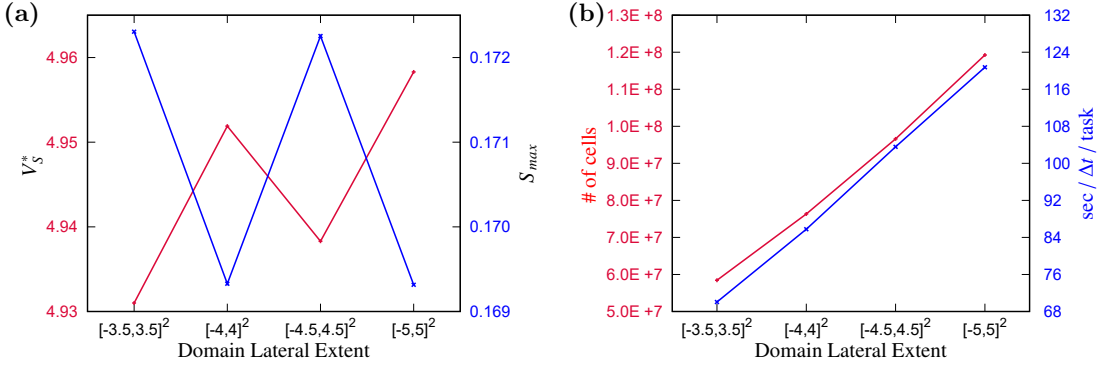
Figure 4.3: Domain lateral extent independence test: (a) Normalized supersaturated volume $V_S^* = V_S/(\pi d_p^3/6)$ and the supersaturation maximum S_{max}, and (b) the total number of lattice nodes and the computational time for the various lateral extents of the domain, while keeping the streamwise extent fixed at $[-5,35]d_p$ and with a constant spatial resolutions of $d_p/32$ at $Re = 200$. The thermodynamic condition of the domain is the same like in Figure 4.2.

$[-3.5,3.5]d_p$ or higher. In Figure 4.3(b), the comparison on the computational load indicates that there is almost a linear increase in the computational time requirement for each Δt. Since, the gain in the accuracy with wider domain is not significant, a domain with $[-3.5,3.5]d_p \times [-3.5,3.5]d_p$ lateral extent is chosen for the next stage of the streamwise extent independence test.
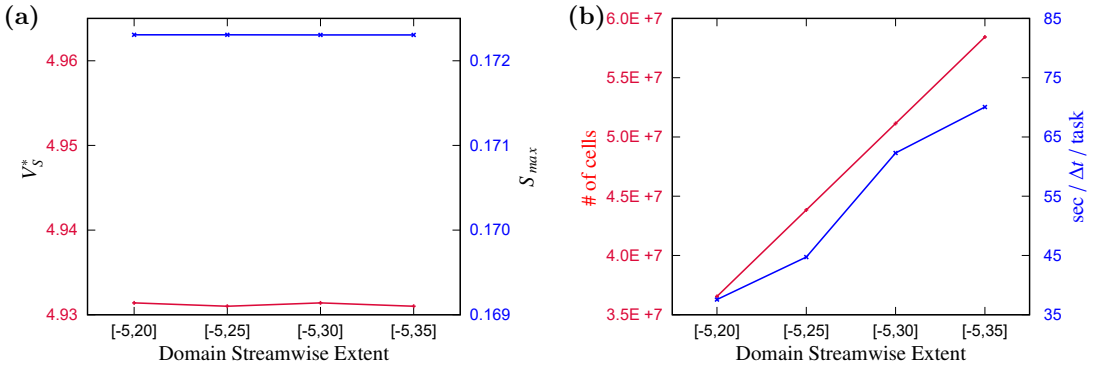
Figure 4.4: Domain streamwise extent independence test: (a) Normalized supersaturated volume $V_S^* = V_S/(\pi d_p^3/6)$ and the supersaturation maximum S_{max}, and (b) the total number of lattice nodes and the computational time for the various streamwise extents of the domain, while keeping the transversal/lateral extent fixed at $[-3.5,3.5]d_p \times [-3.5,3.5]d_p$ and with a constant spatial resolutions of $d_p/32$ at $Re = 200$. The thermodynamic condition of the domain is the same like in Figure 4.2.

Figure 4.4 presents the domain streamwise extent independence test by varying the streamwise extent from $[-5,35]d_p$ to $[-5,20]d_p$, while keeping the lateral extent fixed at $[-3.5,3.5]d_p \times [-3.5,3.5]d_p$ and the grid size fixed at $d_p/32$. In the Figure 4.4(a), the axes for the V_S and the S_{max} are kept the same like in Figure 4.3(a). Here it can be seen, that the longer streamwise extent in the domain do not change the results in the supersaturation quantities at all. In Figure 4.4(b), it further can be seen that there is some increase in the computational load for the longer domain. However, since there is not any significant improvement in the computation of the supersaturation quantities with the longer/wider/fine resolution domain with respect to the inherent computational cost, the domain with the $[-5,20]d_p \times [-3.5,3.5]d_p \times [-3.5,3.5]d_p$ extent with a grid size of $d_p/32$ is chosen for this study.

4.2.1 Structure of Hydrometeor Wake Supersaturation
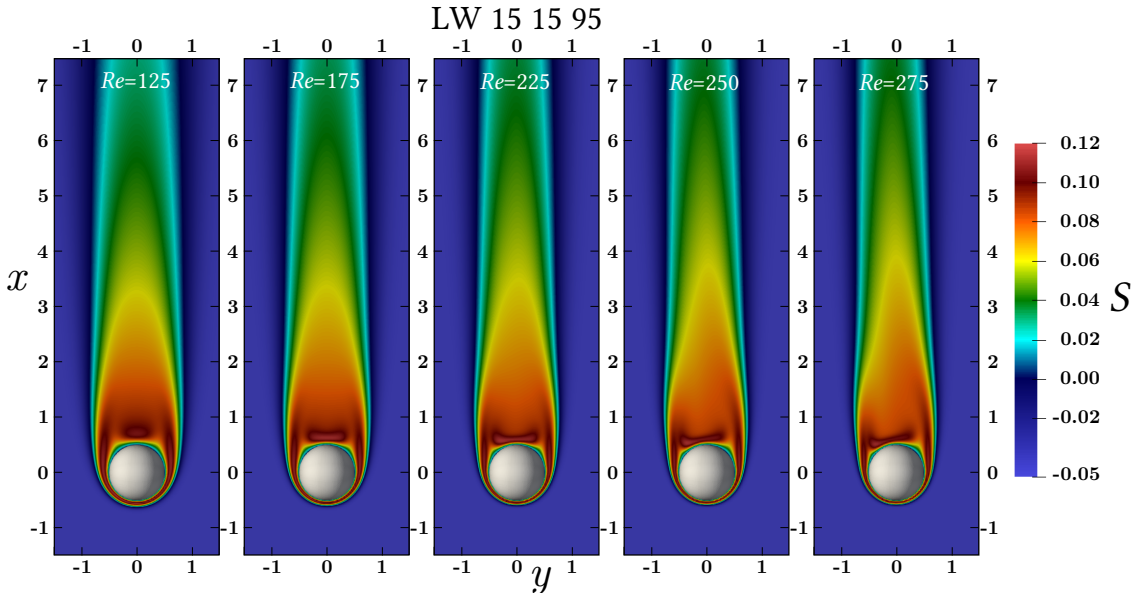
Figure 4.5: Spatial distribution of the supersaturation S in the wake of (L) liquid (W) warm droplets at (15) 15 °C temperature and with a (15) $\Delta T = 15$ °C temperature difference from the ambient which have (95) 95% relative humidity condition. The visualization is across the central orthogonal plane (y, x) passing through the center of the sphere with an extent of $[-1.5,1.5]d_p$ along the horizontal and $[-1.5,7.5]d_p$ along the vertical axes.

Figure 4.5 presents the spatial distribution of S for various Re in the 'LW 15 15 95' thermodynamic condition. This temperature difference can be observed during precipitation from a deep convective cloud containing various phases of hydrometeors [156]. A supersaturated volume in the wake of the sphere is observed for various

Re in Figure 4.5, resembling that various sizes of spheres precipitating at their free fall velocities can produce supersaturation in their wake. Special distribution of S in Figure 4.5 shows that the highest magnitudes of the supersaturation is rather concentrated near the rear stagnation zone of the hydrometeor, inside the recirculating region of the wake. Similar to the previously detailed flow quantities, an increase in *Re* results in a shrink in the lateral extent of the supersaturated region, but simultaneously stretch it in the downstream direction. Tilt in the wake of the oblique *Re* also creates an oblique supersaturated volume as shown in Figure 4.5. It is however observed that despite a change in the supersaturated volume with *Re*, the supersaturation maximum obtained in the wake remains almost independent of *Re* for the same thermodynamic condition.

In Figure 4.6, the population density distribution of supersaturation $N(S)$ for the sample population combined along the two central orthogonal planes (z, x) and (y, x) in the wake of the frozen (I) hydrometeors are presented for the $Re = 175$ case. Supersaturation is computed with respect to the ice phase for these $\leq 0\,^{\circ}\text{C}$ temperatures. The top two panels, Figure 4.6(a,b), present the $N(S)$ for the frozen warmer (IW) hydrometeors than the ambient, which shows a larger supersaturated volume V_S as well as the supersaturation maximum S_{max} than the bottom two panels, Figure 4.6(c,d), which represent frozen colder (IC) hydrometeors. $V_S = \int_{S_0}^{S_{max}} N(S)\mathrm{d}S$ is an integral of $N(S)$, where a three dimensional supersaturated population distribution is considered. To avoid numerical round-off errors around the surface of the hydrometeor, where $S = 0$ as the surface is just saturated, the supersaturation threshold S_0 is defined as 1×10^{-4}, with S_{max} being the maximum supersaturation obtained in a simulation. Colors are the same in the top and the bottom panels for the cases of a specific ΔT and RH_∞ condition. The peak at $S = 0.0$ is due to the numerical artifact that the entire volume of the hydrometeor is modeled with saturated condition. Similar to the statistics of other fluid quantities, S sample populations evolve following a Lorentzian function (unless it is influenced by the simulation domain extent). In a fixed $RH_\infty = 90\%$ condition, as in Figure 4.6(a,c), the larger temperature differences ΔT produces larger V_S in the wake and the S_{max} within it, and shows that $\Delta T = 5\,^{\circ}\text{C}$ does not produce any V_S. In a fixed $\Delta T = 15\,^{\circ}\text{C}$ condition in Figure 4.6(b,d) instead, a larger V_S is obtained when RH_∞ approaches a nearly saturation condition.

In order to understand why warmer hydrometeors produce larger V_S and S_{max} for the same phase, ΔT and RH_∞, one needs to consider the physical processes influencing the saturation condition in the wake. Firstly, a hydrometeor warmer than the ambient diffuses heat in the wake and hence increases the temperature in it, while the colder droplet does the opposite. This results in an increase in the saturation vapor pressure for the warmer hydrometeors in its wake, while a decrease for the colder ones. However the second process, which is the diffusion of water vapor, plays a dominant role for the warmer hydrometeors when the minimum ΔT condition that is required to produce some V_s is satisfied. With higher
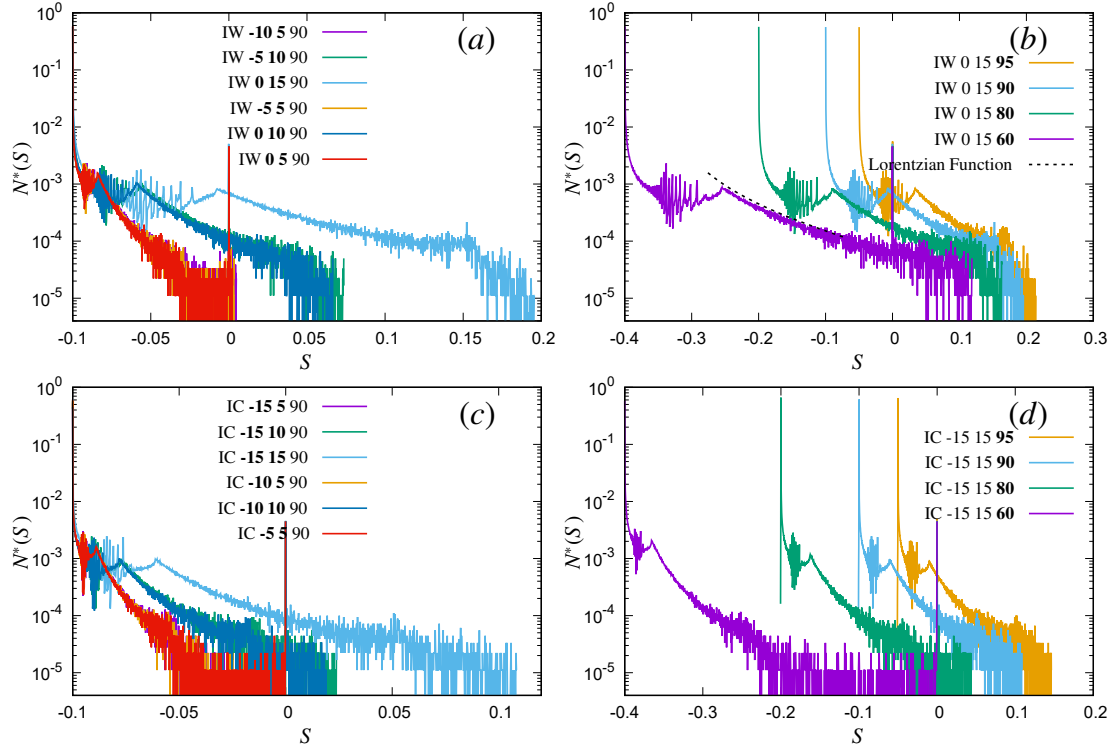
Figure 4.6: Normalized Population density distribution for supersaturation $N^*(S)$ for $Re = 175$ considering frozen ice spheres in various thermodynamic conditions. $N^*(S)$ for various (IW) frozen warm spheres with various ΔT but $RH_\infty = 90\%$ is presented in (a); and with a constant $\Delta T = 15\,°C$ but variable RH_∞ is shown in (b). Similar $N^*(S)$ for various (IC) frozen cold spheres with various ΔT but $RH_\infty = 90\%$ is presented in (c); and with a constant $\Delta T = 15\,°C$ but variable RH_∞ is shown in (d). The samples are from both the central orthogonal (z, x) and (y, x) planes with an extent of $[-3.5, 3.5]d_p$ in horizontal and $[-5, 20]d_p$ in vertical directions, and the population density distributions are normalized with the cumulative area of the sample planes.

ΔT, the warm hydrometeor becomes the source for the diffusion of water vapor which diffuses more when the gradient between the ambient and the hydrometeor surface water vapor density increases exponentially with an increase in temperature gradient. Due to the dominance of water vapor diffusion for the warmer hydrometeor case, supersaturated volume is produced despite the simultaneously warming in the wake. From equations (4.15), one can deduce that the change in the saturated water vapor density $\mathrm{d}\rho_{vs}$ for dT change in the temperature, is proportional to $\exp(\mathrm{dT}/\mathrm{T}^2)$. Therefore, an increase in the ΔT for the warmer hydrometeor case produces an exponential increase in the gradient of the water vapor density, facilitating higher amount of water vapor diffusion from the warmer hydrometeor in

form of the evaporation of liquid water. Whereas for the colder hydrometeor case, cooling in the wake is the only process facilitating a growth in supersaturation while due to a lower water vapor density at the hydrometeor surface than the ambient, the colder hydrometeor condenses water vapor on it as a sink. An interplay of these two processes reduces the V_S production potential of a colder hydrometeor compared to the warmer one.
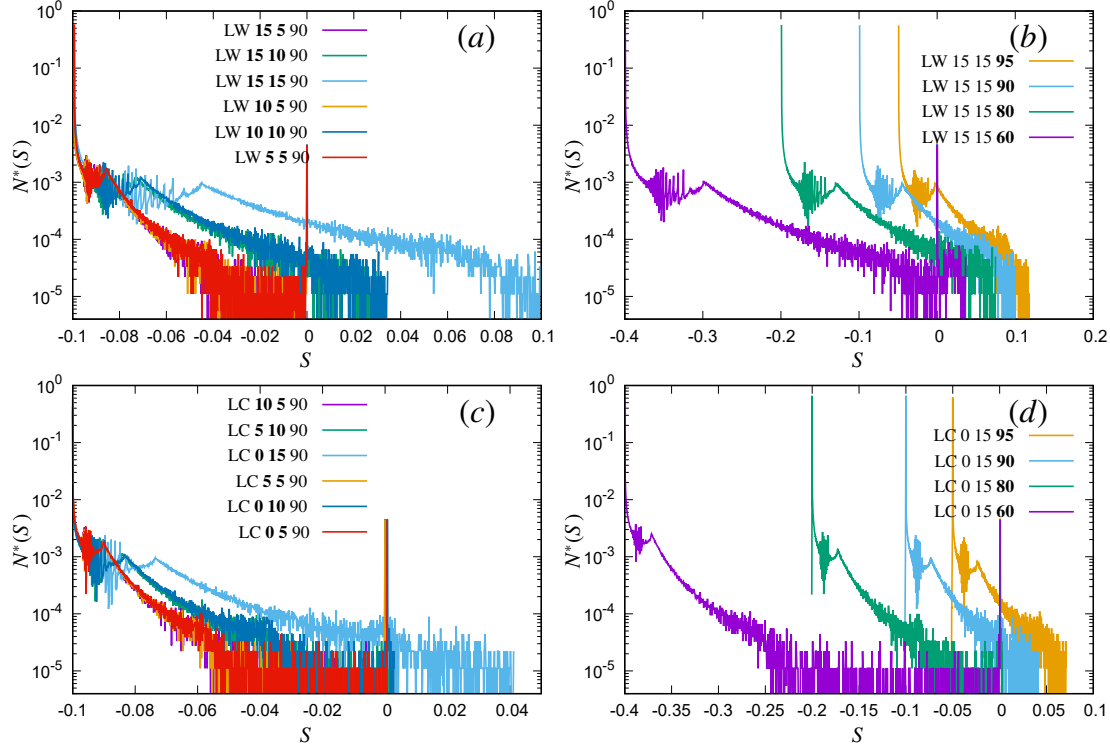
Figure 4.7: Normalized Population density distribution for supersaturation $N^*(S)$ for $Re = 175$ considering liquid droplets in various thermodynamic conditions. $N^*(S)$ for various (LW) liquid warm droplets with various ΔT but $RH_\infty = 90\%$ is presented in (a); and with a constant $\Delta T = 15\,°C$ but variable RH_∞ is shown in (b). Similar $N^*(S)$ for various (LC) liquid cold droplets with various ΔT but $RH_\infty = 90\%$ is presented in (c); and with a constant $\Delta T = 15\,°C$ but variable RH_∞ is shown in (d). The samples are from the same planes as in Figure 4.6.

Figure 4.7 presents the population density function of supersaturation $N(S)$ for the sample population in the wake of the liquid (L) water droplets for the same $Re = 175$ case. An overall comparison between the Figure 4.6 and Figure 4.7 evidences that the V_S and S_{max} produced with respect to the ice phase for the same ΔT and RH_∞ is larger in Figure 4.6 than it is in the Figure 4.7 with respect to the water phase. Since the saturation vapor pressure with respect to the ice phase at temperatures of $< 0\,°C$ is lower than it is with respect to the water phase, V_S

and S_{max} is higher. This indicates that growth of a particle at $< 0\,°C$ temperature is favored higher by the deposition of ice than water in a supersaturated $< 0\,°C$ ambient. Similar to Figure 4.7, the liquid water droplets also produces larger V_S and S_{max} when it is warmer than the ambient in comparison to the cooler droplets. In case of a colder droplet than the ambient, even a ΔT of $10\,°C$ did not produce any V_S in Figure 4.7(c) in contrast to the Figure 4.6(c).

Figure 4.8(a) shows an example of a visualization of the supersaturation field at $Re = 275$ in an ambient relative humidity of 90% with respect to ice phase for a warm hydrometeor (IW 0 15 90). High supersaturation is clearly visible in the boundary layer of the hydrometeor and in the near wake, as well as, in the large region downstream of the hydrometeor. In this oblique regime, some streamlines pass through the wake's vortices, a feature consistent with the results of [66] for the oblique wake vortex structures. The overall distribution of supersaturation in the entire three dimensional domain above a supersaturation threshold of $S_0 > 1 \times 10^{-4}$ is shown in Figure 4.8(b). The statistics of the bright colored supersaturated region in Figure 4.8(a) shows the evolution in the number density of the S population following a Lorentzian trend, similar to Chapter 3 which is $\propto S^{-2}$ in Figure 4.8(b). The trend of S^{-2} ceases around $S \geq 0.13$, which is the highest magnitude of S reached within the boundary layer and in the recirculating zone behind the hydrometeor in Figure 4.8(a). $N(S)$ decreases slightly with increasing Reynolds number, which implies a reduction in the volume of the supersaturated region with respect to the hydrometeor volume, due to gradual thinning of the boundary layer and a correlated shrinking of the lateral extent of the wake. Although a volumetric change in V_S is observed with different Re, the magnitudes of S_{max} remain almost constant for a specific thermodynamic state, independent of Re.

The evolution of V_S as a function of Re and other thermodynamic parameters is shown in Figure 4.9(a) for exemplary cases presenting a temperature difference ΔT of $15\,°C$ and $RH_\infty = 95\%$. In general, a frozen hydrometeor (solid lines) produces a significantly larger supersaturated region than a liquid hydrometeor (dashed lines). This is partly due to the lower magnitude of the saturation vapor pressure in the ice phase compared to its magnitude in the liquid water phase at temperatures of $< 0\,°C$ (e.g., 13.7% lower at $-15\,°C$). The evolution of V_S, as shown in Figure 4.9(a), with respect to the hydrometeor phase and its warmer or colder state also applies to all other ΔT and RH_∞, as detailed later. Figure 4.9(a) also shows that warmer liquid droplets, as for example, 'LW 15 15 95' in $T_\infty = 0\,°C$ produce almost $2.3 - 2.5$ times larger V_S than ice hydrometeors like 'IC -15 15 95'. This is generally true also for other ΔT and RH_∞. This signifies that the warmer hydrometeors produce larger V_S than the colder ones for similar T_∞, ΔT and RH_∞. This phenomenon can be further explained by analytically solving the normalized T and ρ_v equations, presented below, for the $Re \sim 0$. It is further observed that a minimum of $\Delta T = 4 - 10\,°C$ is necessary to produce $V_S \sim \mathcal{O}(1) \times \pi d_p^3/6$, which are merely thin supersaturated boundary layers around
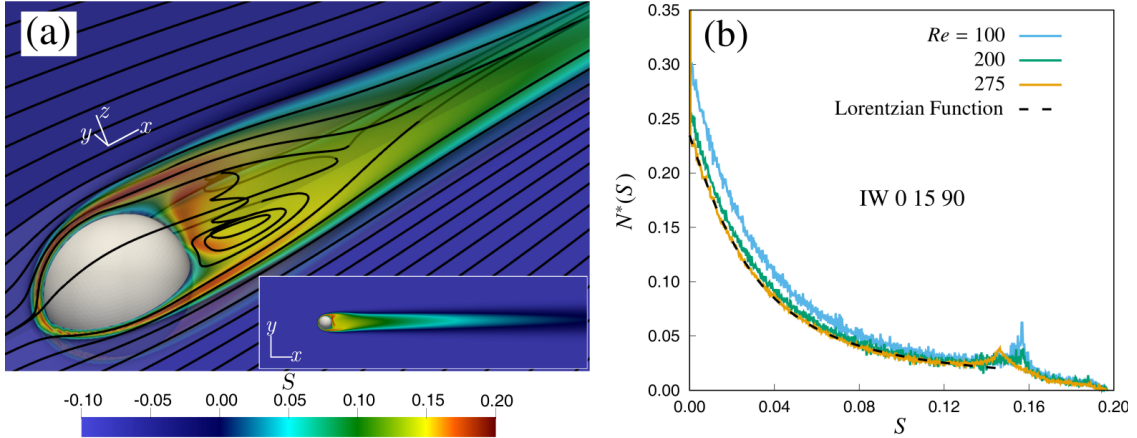
Figure 4.8: Spatial distribution of S. (a) Contours of S in two orthogonal central planes and complex streamlines for $Re = 275$. Only the region near the hydrometeor is plotted, while the entire two dimensional domain along the orthogonal (x, y) plane is in the inset. (b) Normalized sample population distribution $N^*(S) = N(S)/(\pi d_p^3/6)$ for various magnitudes of supersaturation $(S > 0)$ over the entire three dimensional domain for the case 'IW 0 15 90' for the $Re = 100$, 200 and 275. 'IW 0 15 90' represents an (I) frozen but (W) warmer hydrometeor with (0) $T_p = 0\,°\text{C}$ in an ambient at $T_\infty = -15\,°\text{C}$, which gives (15) $\Delta T = 15\,°\text{C}$ and (90) $RH_\infty = 90\%$ with respect to the (I) ice phase.

the hydrometeor. For hydrometeors that are colder than the ambient, ΔT needs to be at least $6 - 12\,°\text{C}$ to produce a similar volume of V_S.

Figure 4.10 presents the extent of the supersaturated volume V_S for all the simulated Reynolds number Re, temperature difference ΔT, ambient humidity RH_∞, and hydrometeor phase ((I) frozen or (L) liquid), and (W) warmer or (C) colder hydrometeor setup than the ambient. The left panel shows the extent of the supersaturated volume V_S with respect to the ice phase for the freezing temperatures below up to $-15\,°\text{C}$. The right panel presents the similar evolution but for positive temperatures up to $15\,°\text{C}$ with respect to the water phase. The simulation results (dots) of V_S in Figure 4.10 agree very well with the fitting model $C_0(1 + C_1 Re^\alpha)$, which are lines in this figure. The values of the fitting coefficients C_0, C_1 and α for each case can be found in Table 4.1. It should be noticed also that this fitting cannot be extended to $Re \to 0$ because the simulated supersaturated volume has a finite limit, which is discussed below.

In the limit of vanishing Reynolds number $Re \to 0$, convection is negligible and therefore the distribution of the scalars is governed by diffusion. One can solve the diffusion equations for the temperature T and the water vapor density ρ_v as an analytical function of the radial distance r from the center of the hydrometeor (see
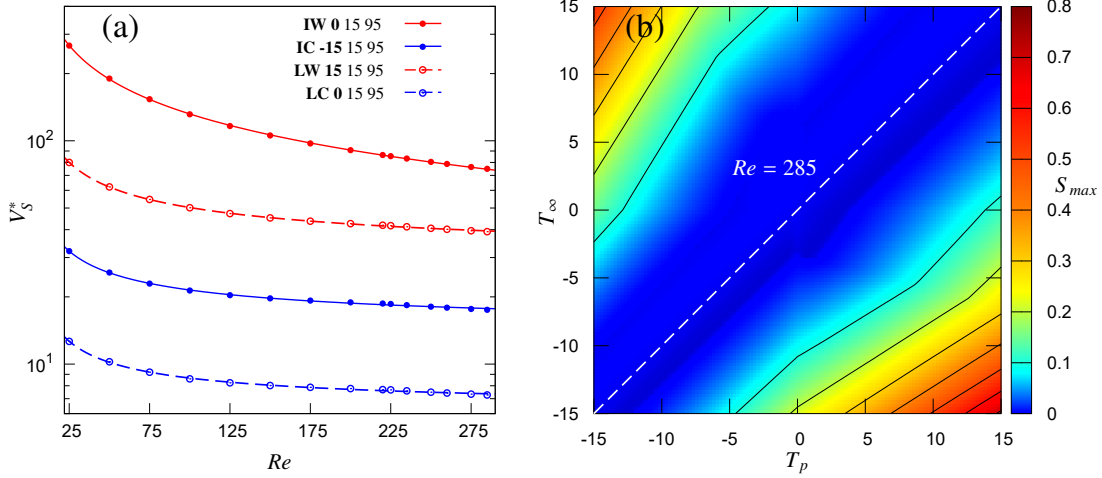
Figure 4.9: The evolution of supersaturation in the wake. (a) The supersaturated volume $V_S^* = V_S/(\pi d_p^3/6)$ is plotted against different Re, considering both (I) frozen and (L) liquid hydrometeors with both (W) warmer or (C) colder temperature than the ambient, while maintaining $\Delta T = 15\,°C$ and $RH_\infty = 95\%$. The dots are simulation results, while the lines correspond to the $C_0(1 + C_1 Re^\alpha)$ fitting model. Solid dots/lines represent frozen hydrometeors and the empty dots/dashed lines represent liquid hydrometeors, with red and blue color for warmer and colder hydrometeors respectively. (b) Supersaturation maximum S_{max} for different values of T_p and T_∞ varying from -15 to $15\,°C$ for $Re = 285$ keeping $RH_\infty = 95\%$. Black contour lines are drawn for each 0.1 increase in S_{max}.

also Baker (1991) [7]),

$$\frac{T - T_\infty}{T_p - T_\infty} = \frac{r_p}{r}, \tag{4.16}$$

$$\frac{\rho_v - \rho_{v,\infty}}{\rho_{v,p} - \rho_{v,\infty}} = \frac{r_p}{r}. \tag{4.17}$$

The consequent supersaturation field in Figure 4.11 presents the analytical solution of S for different ambient relative humidity and a fixed ambient temperature equal to $T_\infty = 0\,°C$. This analytical solution verifies the nature of the supersaturation in the wake of a hydrometeor as seen in the the simulation results. In this case also, the warmer liquid droplets like 'LW 15 15 RH_∞' produce larger V_S than the colder frozen hydrometeors as 'IC -15 15 RH_∞' for various RH_∞ conditions. Moreover, even without any convection (i.e. without relevant Prandtl Pr or Schmidt Sc numbers), supersaturation would happen around a stationary hydrometeor with presence of higher ΔT and gradient of water vapor.

In all $Re >> 0$ cases, the supersatured volume can be fitted by the following scaling function (goodness of fit 99.8%) for the whole range of the Reynolds number,
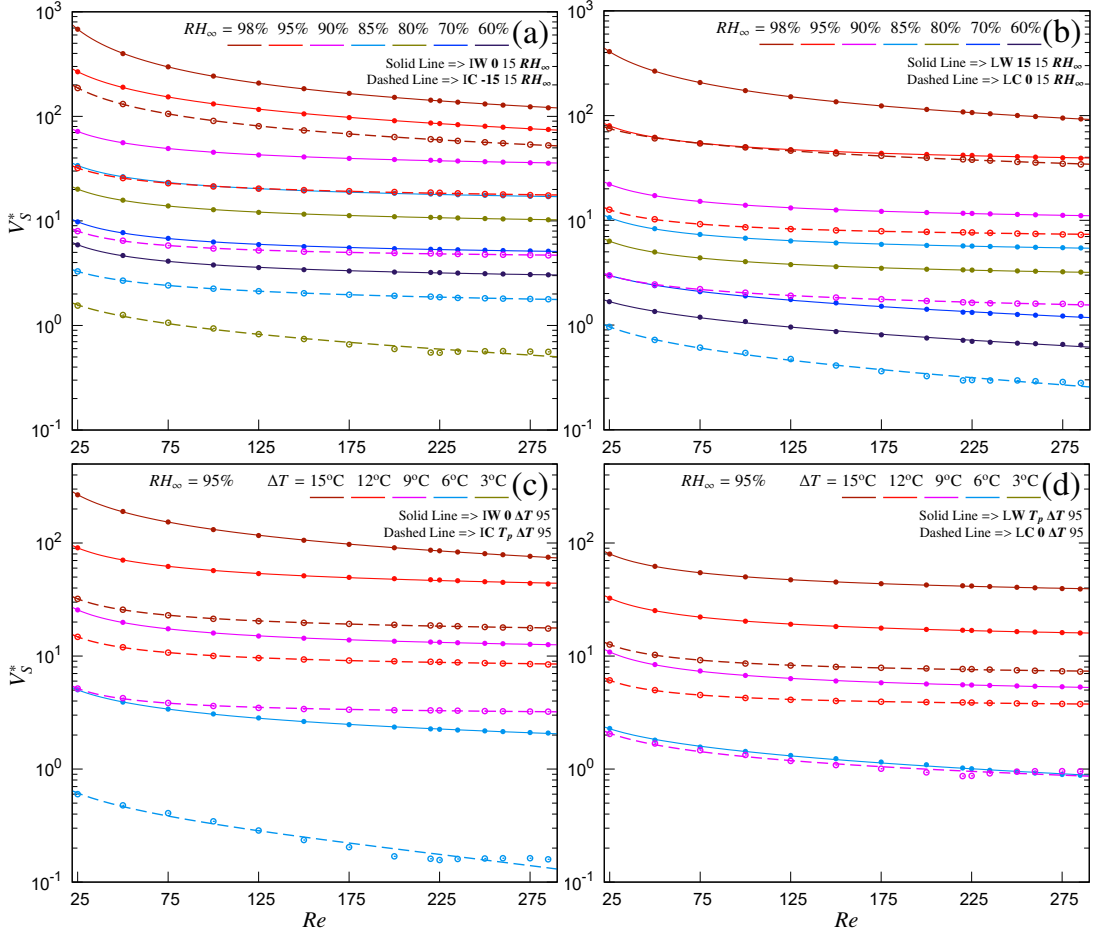
Figure 4.10: Evolution of the supersaturated volume $V_S^* = V_S/(\pi d_p^3/6)$ against various Re: (a) (I) frozen and (b) (L) liquid hydrometeors for various RH_∞ values but keeping $\Delta T = 15\,°C$. (c) (I) frozen and (d) (L) liquid hydrometeors for various ΔT values but keeping $RH_\infty = 95\%$. Both (W) warmer in solid dots/lines and (C) colder hydrometeors in empty dots/dashed lines are considered with respect to the ambient. Dots are simulation results while lines correspond to fitting model $C_0(1 + C_1 Re^\alpha)$. T_p in abbreviated legends of (c,d) represent cases where $T_\infty = 0\,°C$ and T_p varies according to ΔT. Changing parameters are boldfaced in the legends.

despite the change in the wake structure around $Re = 220$.

$$V_S = C_0(1 + C_1 Re^\alpha) \tag{4.18}$$

The fitting coefficient C_0 represents an asymptotic value, which depends on the thermodynamic parameters of the ambient and the hydrometeor, i.e., ΔT, RH_∞, (I) ice or (L) liquid, (W) warm or (C) colder temperature than the ambient. The coefficient C_1 and the exponent α show a minor sensitivity to the thermodynamic

Table 4.1: C_0, C_1 and α for various thermodynamic conditions.

Simulation setup	C_0	C_1	α
IW 0 15 60	2.2199	11.9851	0.6132
IW 0 15 70	3.932	12.3555	0.6563
IW 0 15 80	7.5023	12.4841	0.6223
IW 0 15 85	12.1885	12.6701	0.6093
IW 0 15 90	25.0411	12.814	0.5986
IW 0 9 95	8.8808	13.661	0.6155
IW 0 12 95	27.3538	13.2627	0.5426
IC -15 15 90	4.04226	10.263	0.7301
IC -15 15 95	13.6526	9.8533	0.618
IC -9 9 95	2.8984	10.5247	0.8073
IC -12 12 95	6.9673	9.5231	0.6641
LW 15 15 80	2.23164	12.5049	0.5953
LW 15 15 85	4.04434	12.7813	0.6399
LW 15 15 90	7.96581	13.0352	0.6192
LW 15 15 95	27.1115	13.29	0.5962
LW 9 9 95	3.6999	14.1781	0.6184
LW 12 12 95	11.1848	13.5777	0.6095
LC 0 15 95	6.1379	9.6301	0.6853
LC 0 12 95	3.3626	10.2981	0.7875

parameters, as, C_1 is between $10-13$ and α is -0.63 ± 0.02 for our simulations. The data only deviates significantly when the supersaturated region is not completely within the computational domain (e.g., the case of warmer ice hydrometeors at higher Reynolds number and in almost saturated ambient) and thus considered as a numerical artifact. One can observed that the $Re^{-0.63}$ scaling of the supersaturated volume closely follows the scaling of the drag coefficient with the Reynolds number in the investigated range of Re [23]. Thus the decrease in V_S follows the dynamics of the wake, as also Figure 4.8(a) suggests. This aspect requires, however, further quantitative investigation.

Figure 4.9(b) shows the development of the maximum supersaturation S_{max} over a wide range of hydrometeor temperature T_p and ambient temperature T_∞ at a fixed Reynolds number $Re = 285$ and an ambient relative humidity $RH_\infty = 95\%$ for both (I) frozen and (L) liquid hydrometeors with both (W) warmer or (C) colder temperature than the ambient. The diagonal in white dashed line corresponds to $T_p = T_\infty$ and divides the plane into the colder hydrometeor case (top left) and the warmer hydrometeor case (bottom right). The temperature difference ΔT plays a crucial role, since S_{max} increases almost exponentially with it at constant RH_∞. Similar to V_S, warmer hydrometeors generally produce a higher supersaturation
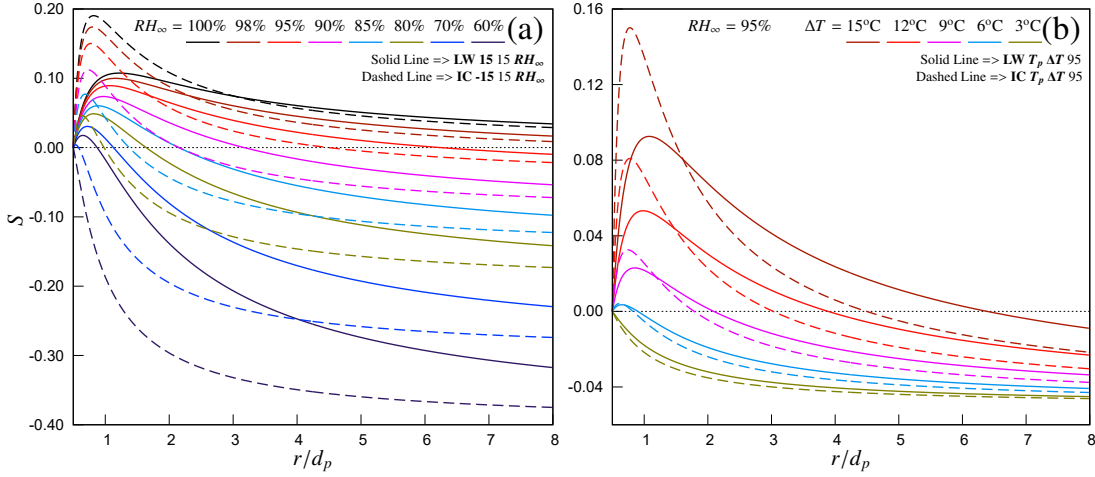
Figure 4.11: Analytical solution of S at $Re \sim 0$ resembling a purely diffusive process. The evolution of S as a function of the normalized radial distance r/d_p is presented (a) for various RH_∞ setup keeping $\Delta T = 15\,°C$, and (b) for various ΔT setup keeping $RH_\infty = 95\%$ considering both (I) icy frozen and (L) water phased hydrometeors for both (W) warmer and (C) colder temperatures than the ambient. The ambient temperature is kept constant at $T_\infty = 0\,°C$.

maximum than colder hydrometeors at the same ΔT, regardless of their frozen or liquid state. The only exception happens in a nearly saturated ambient at $T_\infty = 0\,°C$, because the warmer hydrometeor is a liquid one while the colder one is frozen. In addition, S_{max} evolves almost independently of Re for various thermodynamic conditions.

Figure 4.12 presents the details of the dependence of the maximum supersaturation S_{max} from Re, ΔT, RH_∞, considering both (I) frozen and (L) liquid hydrometeors with both (W) warmer or (C) cooler temperatures than the ambient. S_{max} is almost independent of Re for a specific thermodynamic condition.

4.2.2 Cloud Aerosols in the Wake-Induced Supersaturation

Atmospheric aerosols, which can be activated as CCN or INP, behave as passive tracers due to their negligible Stokes number. The momentum relaxation time of a small particle moving in a fluid, which is the time necessary for a particle to reach its asymptotic velocity, is normally referred to as the Stokes timescale. It is proportional to the square of the size of the particle, i.e. $\tau_a = (2/9)\rho_a r_a^2/\mu$ for a small spherical particle, where ρ_a and r_a are the density and radius of the particle respectively and μ is the viscosity of air. The terminal asymptotic velocity relative to the fluid is then $v_a = \tau_a g$, with g the gravity acceleration. When the Stokes timescale is much smaller of the carrier flow timescale and the asymptotic relative
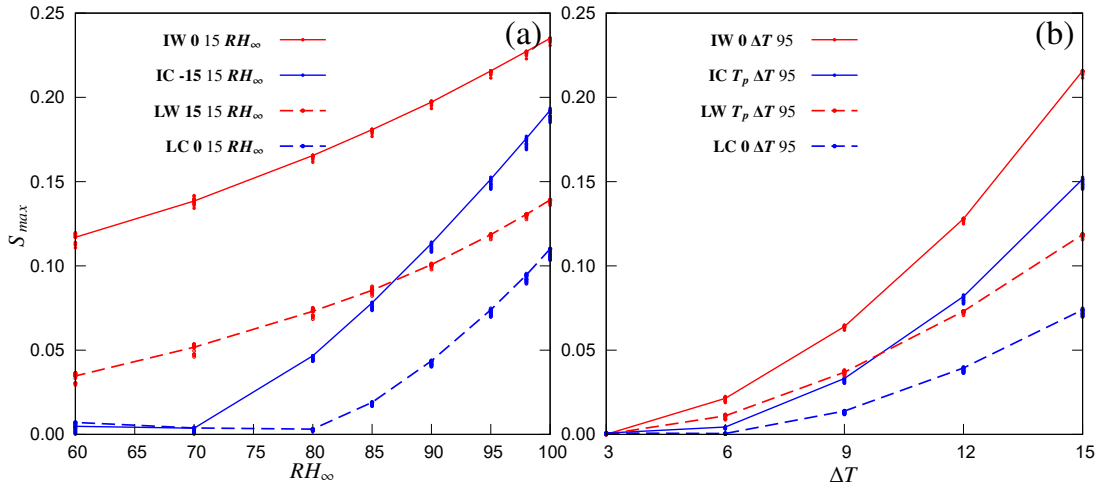
Figure 4.12: Evolution of supersaturation maximum S_{max} for various Re, considering (a) various RH_∞ keeping $\Delta T = 15\,°\mathrm{C}$, and (b) various values of ΔT while keeping $RH_\infty = 95\%$. Both (I) frozen and (L) liquid hydrometeors with both (W) warmer or (C) cooler temperatures than the ambient are considered. Solid line and dashed lines resemble the data of $Re = 285$ case, while, the dots clustered together around the $Re = 285$ case are the results for other axisymmetric or oblique Re. T_p in (b) denotes variation in hydrometeor temperature, such that T_∞ remains $0\,°\mathrm{C}$ for a specific ΔT.

velocity is much smaller than the flow velocity, a particle tends to move as a fluid element. This is the typical situation of a particle with a small inertia. When these conditions are satisfied, particles can be treated as passive tracers. The latter condition is usually described in terms of the Stokes number, defined as the ratio between the particle relaxation time and the flow timescale. It had been verified that inertial effect begin to have a role only when the Stokes number is higher than 0.1 (see, e.g. Boffetta et al. (2007) [17]). This is the situation of aerosols: their very small size and inertia make them to have a negligible terminal (settling) velocity relative to the air (of the order of 10^{-7} m/s) and a very small relaxation time (of the order of 10^{-8} s), so that the time necessary to adapt to changes in the air velocity is very small, much smaller than the flow timescale. In this specific problem, the timescale of the air flow around the falling hydrometeor is given by $\tau = d/u_\infty$, so that the Stokes number is $\tau_a/\tau \sim 10^{-5} \ll 1$ and $v_a/u_\infty \sim 10^{-7} \ll 1$. In general, the smallest dynamically active scale in a turbulent cloud is the Kolmogorov microscale, which has much larger time scale than the aerosol response time (typically around 10^{-1} to 10^{-2} s). Therefore even globally inside a cloud, aerosols behave as passive tracers following the turbulent flow field. In our previous publication, Bhowmick and Iovieno (2019) [9], it can be seen that even 6 μm radius droplets, much larger than aerosols, behave almost as passive tracers.
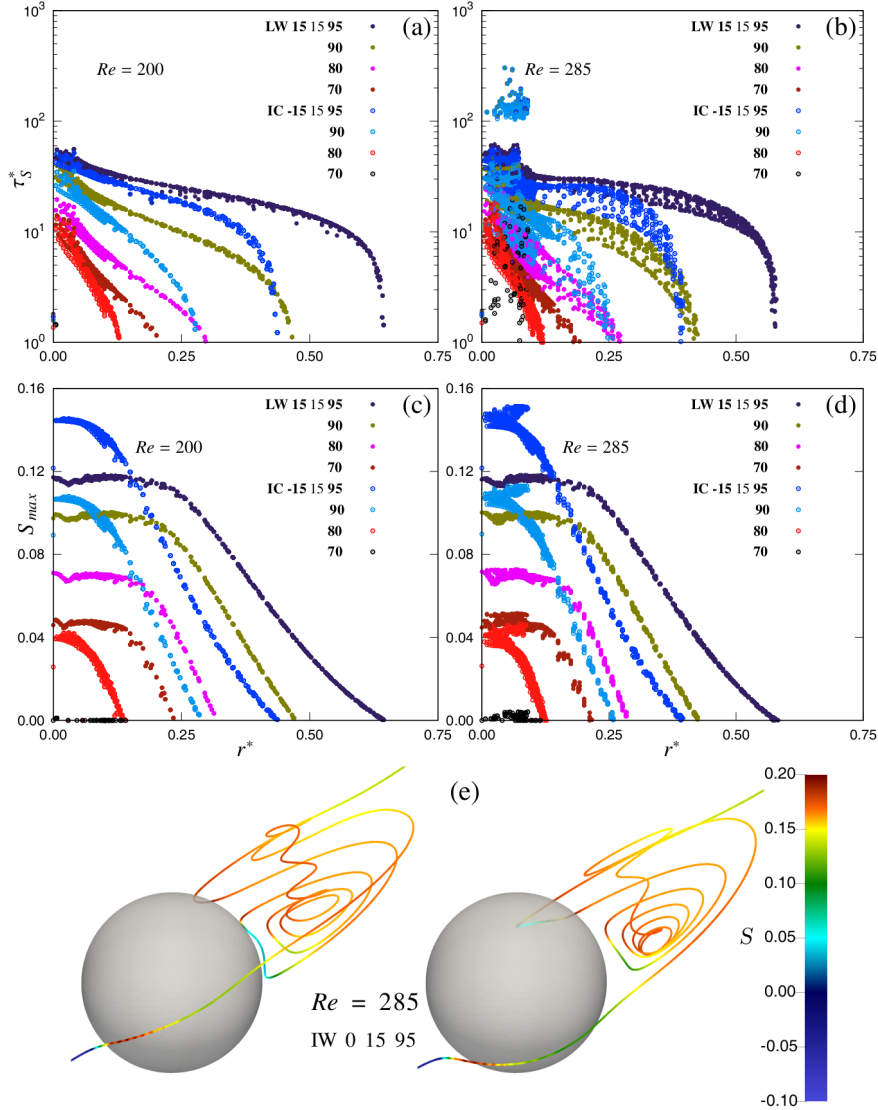
Figure 4.13: The residence time $\tau_S^* = \tau_S/(d_p/U_p)$ of a tracer within the supersaturated zone and the maximum supersaturation S_{max} experienced by a tracer are plotted as a function of the initial radial distance $r^* = r/d_p$ from the hydrometeor center line ($y = z = 0$). The evolution of τ_S^* within the $S > 1 \times 10^{-4}$ zone is plotted for $Re = 200$ in (a) and for $Re = 285$ in (b), while S_{max} is plotted for $Re = 200$ in (c) and for $Re = 285$ in (d). Various hydrometeor phases and RH_∞ conditions are considered keeping $\Delta T = 15\,°\mathrm{C}$ and $T_\infty = 0\,°\mathrm{C}$. Solid and empty dots represent the liquid warm and frozen cold hydrometeor conditions, respectively. In (e), two example tracer trajectories for $Re = 285$ are shown, colored according to the instantaneous S it experiences in an 'IW 0 15 95' setup, resulting in $\tau_S^* = 151\,\mathrm{s}$ (left) and $\tau_S^* = 145.4\,\mathrm{s}$ (right).

93

To understand the possible role of the supersaturated hydrometeor wake on the aerosol activation, the trajectories of passive tracers injected upstream of the hydrometeor are analyzed. Since only tracers starting their motion near the center line $y = z = 0$ can enter the supersaturated regions, two injection patterns are used: a coarse pattern where 2601 tracers are injected uniformly over an area of $[1.5d_p \times 1.5d_p]$ and a fine pattern where 1681 tracers are injected uniformly over an area of $[0.2d_p \times 0.2d_p]$ in the inlet around the hydrometeor center line. An adaptive Runge-Kutta 4-5 method is used for time integration of the trajectories. Velocity, temperature and vapor density at the tracer position are obtained by tri-linear interpolation.

The possibility of an aerosol being activated as a CCN depends both on the instantaneous supersaturation it experiences and on the time it spends in highly supersaturated regions (residence time), so that it reaches a critical size that prevents its complete evaporation/sublimation according to the Köhler curve [126]. The activation of an aerosol as an INP depends on many physical and chemical parameters but, even for initiations of the INPs, a sufficient long residence time in a supersaturated region is required. Moreover, the activated CCNs can also grow to be INPs, through immersion freezing or contact freezing or homogeneous freezing of the liquid water [55]. In Figure 4.13, therefore, the residence time τ_S that a tracer spends within the supersaturated wake in panels (a) and (b), and S_{max} that it sees in (c) and (d) as a function of the initial radial distance r of the tracer from the hydrometeor center line for axisymmetric ($Re = 200$) and oblique ($Re = 285$) wakes are plotted respectively. The different structure of the wake creates clearly visible differences in the supersaturation experienced by the tracers. The tracers, which stay for the longer time in the supersaturated region of axisymmetric $Re = 200$ wake, are introduced near the center line as shown in Figure 4.13(a), so that they move through the supersaturated boundary layer and along the border of the wake. However, no tracers could enter the closed recirculating region, resulting τ_S at most in the order of $10^1 d_p/U_p$ for $Re = 200$.

In the oblique wake regime of $Re = 285$, shown exemplary in Figure 4.13(b), tracers injected far from the axis show no significant qualitative difference in τ_S and they experience lower S_{max} in Figure 4.13(d) for a short time. However, 'lucky tracers' injected near the center line can enter the near wake vortical region and therefore remain trapped in the supersaturated recirculating zone for a longer time before moving downstream. This increases τ_S by a factor between 2.5 to 9 with respect to the bulk of the tracers injected from the same radial distance in the symmetric or oblique wake regimes. One can quantify the extent of the injection region of lucky tracers with $\tau_S \geq 10^2 d_p/U_p$, which is confined to a radial distance of $r/d_p \leq 0.09$.

The capture frontal area A_F, as shown in the schematic Figure 4.14, is defined as the asymptotic area of origin of the trajectories of the entrained "lucky" aerosols out of all the finely introduced aerosols (i.e., the intersection of a plane normal to

94

the asymptotic velocity with the trajectories of the "lucky" aerosols). The 'capture efficiency' E, which is defined as the ratio between the total frontal area A_F of the tracers with $\tau_S \geq 10^2 d_p/U_p$ and the frontal area of the hydrometeor $\pi d_p^2/4$, is about 5×10^{-3} for $Re = 285$, while it is almost zero in the steady axisymmetric regime.
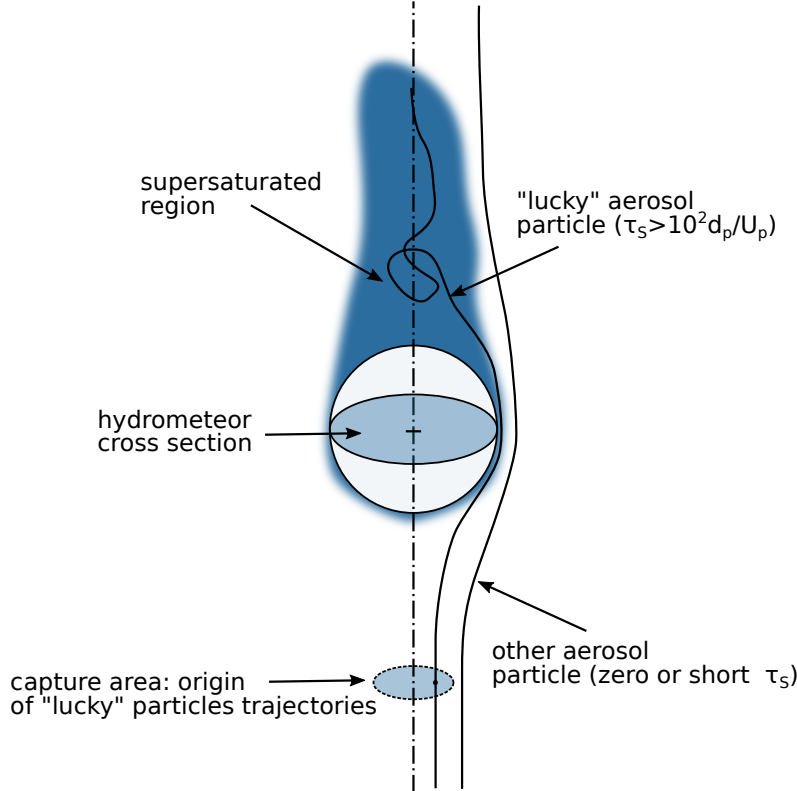
Figure 4.14: A schematic diagram on the definition of capture frontal area A_F.

The scatter in Figure 4.13(b) for $Re = 285$, which produces petal-like patterns at low r/d_p, is due to the lack of axial symmetry in the oblique wake regime. The larger extent of the supersaturated region generated by a warmer hydrometeor (solid dots) compared to a colder hydrometeor (empty dots) for the same ΔT and RH_∞ is also visible in Figure 4.13. This is evident from the lower decay of τ_S and S_{max} with r/d_p for warmer hydrometeors.

The mechanism allowing long residence times in the case of an oblique wake can be inferred from Figure 4.13(e), which shows two sample tracer trajectories with $r/d_p = 0.078$ and 0.066, respectively, each of which enter the vortical oblique wake region at $Re = 285$. The colors of the trajectories represent the instantaneous supersaturation that the tracers experience. Such lucky tracers, introduced very near the hydrometeor center line, experience a sudden maximum of supersaturation $S \sim 20\%$, for a short time as they move through the boundary layer on the front of the sphere. Then the supersaturation gradually decreases along the trajectory

to about 10%. Later, when the tracer is entrained within the recirculating oblique wake zone, it experiences higher supersaturation again, but for a longer time due to the low velocity and complex three dimensional flow structures of this region. However, such entrainment phenomenon is only observed when the wake loses its symmetry, i.e. in the oblique wake regime from $Re = 225$ in our simulations.

4.3 Aerosol Activation in Wake Supersaturation

4.3.1 Rate of Aerosol Entrainment in Oblique Wake

The extent of the supersaturated volume, the maximum supersaturation and the residence time of an aerosol in the supersaturated wake of precipitating hydrometeors provide important insights on aerosol activation in the atmosphere. For the aerosol entrainment in the wake, the precipitating hydrometeor has to generate an oblique wake, which occurs for a precipitating spherical raindrop when the diameter is at least $1\,\mathrm{mm}$. Since raindrops exceeding a diameter of 2 to $3\,\mathrm{mm}$ are very rare and occur mostly in thunderstorms [116], and also to satisfy the need for higher temperature difference; it is evident that wake-induced supersaturation can happen mainly in deep convective clouds with fully glaciated, mixed phased as well as various liquid phase hydrometeors due to a large temperature variation [156]. From the results of the previous section, the entertainment rate of 'lucky aerosols', which enter per unit time into the frontal capture area A_F of a hydrometeor and thus experience a long residence time inside the supersaturated wake, is estimated as

$$N = N_a U_p A_F = N_a U_p E \pi d_p^2 / 4.$$

Here E is the capture efficacy, which is about 5×10^{-3} for $Re = 285$ and almost zero in the steady axisymmetric regime. N_a is the typical aerosol concentration, which varies from $\mathcal{O}(10^8)$ to $\mathcal{O}(10^9)\mathrm{m}^{-3}$ within the continental clouds, and from $\mathcal{O}(10^7)$ to $\mathcal{O}(10^8)\mathrm{m}^{-3}$ within the remote marine clouds [116]. Therefore, $\mathcal{O}(10^0)\mathrm{s}^{-1} \leq N \leq \mathcal{O}(10^1)\mathrm{s}^{-1}$ aerosols in continental clouds and $\mathcal{O}(10^{-1})\mathrm{s}^{-1} \leq N \leq \mathcal{O}(10^0)\mathrm{s}^{-1}$ aerosols in remote marine clouds experience a higher residence time and higher supersaturation in the wake when a raindrop of at least $1\,\mathrm{mm}$ diameter settles at its terminal velocity ($Re \simeq 285$). Measurements of the number density of raindrops above $1\,\mathrm{mm}$ show a wide variability, which can be estimated to be in the range of $\mathcal{O}(10^1) - \mathcal{O}(10^2)$ drops per cubic meter [150, 1]. This leads to an entrainment rate of aerosols in the drop wakes between $\mathcal{O}(10^0)$ and $\mathcal{O}(10^3)\mathrm{m}^{-3}\,\mathrm{s}^{-1}$. Since the capture efficiency E increases with the Reynolds number (here the E of $Re = 285$ is used), this could be considered a conservative estimate.

4.3.2   Aerosol Activating Potential of Wake Supersaturation

The critical supersaturation required for the activation of aerosols as a CCN is achieved by solving the Köhler equation for its chemical compositions and size [126, 93, 87]. Since the critical supersaturation needed for the heterogeneous nucleation of common atmospheric aerosols rarely exceed $1-2\%$ in a uniform environment, we may estimate the aerosol growth during its residence time within the supersaturated wake by considering the average supersaturation, which is much higher than 2% for a temperature difference of $15\,^\circ\mathrm{C}$ between the hydrometeor and the ambient.

The order of magnitude of the total vapor mass inside the supersaturated wake region can be estimated as

$$m_v = \int_{V_S} \rho_v \mathrm{d}V = \int_{V_S} \rho_{vs}(1 + S)\mathrm{d}V \sim \rho_{vs}(T_m)(1 + S_m)V_S,$$

where V_S is the superaturated volume, $\rho_{vs}(T_m)$ is the density of saturated vapor at the mean temperature T_m, and S_m is the mean supersaturation within V_S. This mass is available for condensation on the trapped 'lucky' aerosol particles.

The condensational growth on an aerosol particle with an initial radius of r_0 in a supersaturated ambient of S can be described by the following equation approximately (see the book by Pruppacher and Klett (2010) [116], Chapter 13),

$$\frac{\mathrm{d}r}{\mathrm{d}t} \simeq C\frac{S}{r},$$

where r is the instantaneous radius of the forming droplet and the coefficient C is given by $C \simeq \kappa_v \rho_{vs}/\rho_w$ (as usual, ρ_w is the liquid water density). By assuming that the mean ambient conditions seen by an aerosol does not change significantly (see discussion in section 4.1.1), one may integrate this equation to estimate that, after having spent its residence time τ_S within V_S, its size becomes

$$r^2 \sim r_0^2 + 2CS_m\tau_S. \tag{4.19}$$

The activation of the trapped aerosol as a condensation nucleus depletes the vapor mass of the supersaturated wake. The change in the vapor mass due to condensation on a single trapped aerosol is therefore

$$\Delta m_v = \frac{4}{3}\pi\rho_w(r^3 - r_0^3) \simeq \frac{4}{3}\pi\rho_w r_0^3\left[(1 + 2CS_m r_0^{-2}\tau_S)^{3/2} - 1\right]. \tag{4.20}$$

Therefore, the ratio between the amount of condensed mass on an aerosol and the total available vapor mass within the supersaturated region is of the order of

$$\frac{\Delta m_v}{m_v} \sim \frac{4\pi}{3}\frac{r_0^3}{V_S}\frac{\rho_w}{\rho_{vs}(T_m)}\frac{(1 + 2CS_m r_0^{-2}\tau_S)^{3/2} - 1}{1 + S_m}. \tag{4.21}$$

One can express this ratio as a function of the two dimensionless quantities used in this chapter, the dimensionless supersaturated volume V_S^* and the dimensionless residence time τ_S^*:

$$V_S^* = \frac{V_S}{\pi d_p^3/6}, \qquad \tau_S^* = \frac{\tau_S}{d_p/U_p},$$

where, $\pi d_p^3/6 = 4\pi r_p^3/3$ is the volume of the hydrometeor ($d_p = 2r_p$ is its diameter) and U_p is its settling velocity. Therefore, Equation (4.21) can be simply rewritten as

$$\frac{\Delta m_v}{m_v} \sim \frac{1}{V_S^*} \frac{r_0^3}{r_p^3} \frac{\rho_w}{\rho_{vs}(T_m)} \left[\left(1 + 2\frac{CS_m d_p}{r_0^2 U_p}\tau_S^* \right)^{3/2} - 1 \right] \frac{1}{1+S_m}. \qquad (4.22)$$

One can consider a few extreme cases among our simulations, which show that the residence time of the 'lucky' aerosols is long enough to allow the condensational growth which can overcome the supersaturation barrier of the Köhler curves [93] and the vapor mass present inside the supersaturated wake can support such a growth. Here below are the results.

Case 1a: Aerosol of $r_0 = 10\,\text{nm}$ in 'LW 15 15 95' wake

From simulation results of $Re = 285$: $T_m = 2.2\,°\text{C}$, $S_m = 2.75\%$, $V_S^* \sim 39.2$ and lucky particles have $\tau_s^* \sim 150$. Therefore, considering,

$\rho_{vs}(T_m) \sim 5.63 \times 10^{-3}\,\text{kg m}^{-3}$
$\rho_w \sim 1 \times 10^3\,\text{kg m}^{-3}$
$\kappa_v \sim 2.394 \times 10^{-5}\,\text{m}^2\,\text{s}^{-1}$
$r_0 \sim 1 \times 10^{-8}\,\text{m}$
$d_p \sim 1 \times 10^{-3}\,\text{m}$
$U_p \sim 4\,\text{m s}^{-1}$

one gets,

$r \sim 5.27 \times 10^{-7}\,\text{m}$ Final radius of the nucleated aerosol
$m_v \sim 1.19 \times 10^{-10}\,\text{kg}$ Total vapor mass inside supersaturated wake
$\Delta m_v \sim 6.14 \times 10^{-16}\,\text{kg}$ Condensed mass on the aerosol during τ_S
$\Delta m_v/m_v \simeq 5.18 \times 10^{-6}$ Ratio of the condensed vapor to the total vapor

Case 1b: Aerosol of $r_0 = 100\,\text{nm}$ in 'LW 15 15 95' wake

Based on the previous parameters of Case 1a, one gets,

$r \sim 5.37 \times 10^{-7}\,\mathrm{m}$ Final radius of the nucleated aerosol

$m_v \sim 1.19 \times 10^{-10}\,\mathrm{kg}$ Total vapor mass inside supersaturated wake

$\Delta m_v \sim 6.43 \times 10^{-16}\,\mathrm{kg}$ Condensed mass on the aerosol during τ_S

$\Delta m_v/m_v \simeq 5.42 \times 10^{-6}$ Ratio of the condensed vapor to the total vapor

Case 2a: Aerosol of $r_0 = 10\,\mathrm{nm}$ in 'IW 0 15 90' wake

From simulation results of $Re = 285$: $T_m = -12.68\,^{\circ}\mathrm{C}$, $S_m = 5.11\%$, $V_S^* \sim 35.6$ and lucky particles have $\tau_s^* \sim 150$. Therefore, considering,

$\rho_{vs}(T_m) \sim 1.7 \times 10^{-3}\,\mathrm{kg\,m^{-3}}$

$\rho_w \sim 1 \times 10^{3}\,\mathrm{kg\,m^{-3}}$

$\kappa_v \sim 2.394 \times 10^{-5}\,\mathrm{m^2\,s^{-1}}$

$r_0 \sim 1 \times 10^{-8}\,\mathrm{m}$

$d_p \sim 1 \times 10^{-3}\,\mathrm{m}$

$U_p \sim 4\,\mathrm{m\,s^{-1}}$

one gets,

$r \sim 3.95 \times 10^{-7}\,\mathrm{m}$ Final radius of the nucleated aerosol

$m_v \sim 3.41 \times 10^{-11}\,\mathrm{kg}$ Total vapor mass inside supersaturated wake

$\Delta m_v \sim 2.58 \times 10^{-16}\,\mathrm{kg}$ Condensed mass on the aerosol during τ_S

$\Delta m_v/m_v \simeq 7.56 \times 10^{-6}$ Ratio of the condensed vapor to the total vapor

Case 2b: Aerosol of $r_0 = 100\,\mathrm{nm}$ in 'IW 0 15 90' wake

Based on the previous parameters of Case 2a, one gets,

$r \sim 4.07 \times 10^{-7}\,\mathrm{m}$ Final radius of the nucleated aerosol

$m_v \sim 3.41 \times 10^{-11}\,\mathrm{kg}$ Total vapor mass inside supersaturated wake

$\Delta m_v \sim 2.79 \times 10^{-16}\,\mathrm{kg}$ Condensed mass on the aerosol during τ_S

$\Delta m_v/m_v \simeq 8.17 \times 10^{-6}$ Ratio of the condensed vapor to the total vapor

Therefore, inside such a supersaturated wake, an aerosol can grow well above its critical radius by deposition of water vapor and therefore be activated as a CCN. During a convective precipitation process of typically 20 minutes, $\mathcal{O}(10^3) - \mathcal{O}(10^6)\mathrm{m^{-3}}$ new aerosols can therefore be activated in the wake of the precipitating hydrometeors, which replenish the activated particle concentration in clouds that typically vary in $\mathcal{O}(10^8) - \mathcal{O}(10^9)\mathrm{m^{-3}}$ [124, 59]. The cloud ambient temperature considered in this study is between $-15\,^{\circ}\mathrm{C}$ to $15\,^{\circ}\mathrm{C}$, a range where the concentration of INPs is much smaller than the concentration of CCNs inside the clouds [111, 55]. Moreover, since we have shown that warmer hydrometeors produce a larger

supersaturated volume than the colder hydrometeors, CCN activation will likely dominate over direct INP nucleation. However, considering the deduced entrainment rate of the aerosols in the wake of the hydrometeors, it is expected that also at lower cloud temperatures ($\leq 20\,°C$ where a significant concentration of INPs are detected [102]), still a significant fraction of cloud aerosols may activate in the wake initially as CCNs (depending on the temperature, supersaturation, aerosol chemical composition, and other physical parameters) and then part of such activated CCNs may produce INPs through condensation or immersion freezing [102], or by contact freezing [55], which cannot be inferred from this study because we cannot distinguish between CCN and INP activation.

On the other hand, some CCNs may grow into supercooled cloud droplets that are also detected at very low cloud temperatures [54] at which homogeneous freezing is observed in the laboratory experiments. Therefore, from this study, the relative importance of secondary aerosol activation as INPs can not be estimated due to the vast parameter space influencing it. However, we have obtained a quantification on the rate of aerosol entrainment in the wake-induced supersaturation and its activation potential as CCNs. It should be noted that this rate of activation of aerosols, either as CCNs or both as CCNs and INPs altogether during the process of convective precipitation, is comparable with the experiments of [101] on secondary ice production during the growth of a graupel by rime splintering, and the in field measurements of ice particle production rate by [50], and the in cloud measurements of secondary ice particles by [51]. Whereas, an explicit rate of CCN production inside the clouds is not found that the results from this study can be compared to. For an explicit quantification of wake-induced nucleation, a detailed microphysical study is required taking into account the full details of the changing atmospheric conditions and the particle evolution while falling through the convective clouds. In addition, the effects of other influencing factors, such as cloud free stream turbulence [6], strong convective motions like central updraft or entrainment induced mixing [46, 103, 9], or strong downdraft during precipitation [151] may further influence this nucleation and activation rate, which needs to be carefully investigated.

4.4   Summary and Conclusions

In this chapter a detailed analysis of the supersaturation field and aerosol activation around a spherical hydrometeor, which settles at its terminal velocity, for different atmospheric conditions is presented. The Navier-Stokes equation for the flow velocity and the one-way coupled advection-diffusion equations for temperature and density of water vapor are solved with the lattice Boltzmann method. The supersaturated volume V_S in the wake of steady axisymmetric regime ($Re \leq 220$)

and oblique regime ($225 \leq Re \leq 285$) shows a $Re^{-0.63}$ decrease for the same thermodynamic conditions. Whereas, V_S is very sensitive to the temperature difference ΔT between the hydrometeor and the ambient and its relative humidity condition RH_∞, so that V_S at constant ΔT increases as RH_∞ increases, which means that a small amount of vapor diffusion from a warmer hydrometeor or cooling by a colder hydrometeor can easily supersaturate an almost saturated wake volume. However, when RH_∞ is fixed, ΔT plays a crucial role in V_S, since without an adequate ΔT a negligible supersaturated volume is generated. In addition, persistently warmer hydrometeors than the ambient produced larger V_S than the colder ones. The supersaturation maximum S_{max} behaves qualitatively similar to V_S.

Lagrangian tracking of aerosols as passive tracers shows how the complex flow pattern of the oblique wake allows some lucky aerosols to be entrained within the recirculating wake, resulting in a higher residence time within the highly supersaturated vortical zone. Quantitatively within the supersaturated oblique wake of $Re = 285$, about 158 of finely introduced 977 tracers at a radial distance up to $r/d_p = 0.09$ showed residence time grater than $10^2 d_p/U_p$. Importantly, it is found that such a long residence time within the highly supersaturated wake not only exposes the aerosols to a higher level of supersaturation compared to its nucleation barrier, but also provides enough time for the growth by deposition of water vapor to exceed its critical size, and therefore to be activated potentially as a CCN and sometimes possibly as an INP. The frontal area of these lucky tracers entering the vortical but highly supersaturated oblique wake has a capture efficiency of $\sim 5 \times 10^{-3}$ with respect to the hydrometeor frontal area at $Re = 285$. Our analysis shows that wake-induced nucleation of aerosols during a convective precipitation of 20 minutes can generate $\mathcal{O}(10^3) - \mathcal{O}(10^6)\mathrm{m}^{-3}$ new CCNs and some fraction as INPs, which is in order of magnitude comparable to other secondary ice production mechanisms, and thus contribute to the life cycle of clouds.

End of Chapter 4

Chapter 5

Conclusions

In this thesis, various open scientific questions regarding the dynamical processes inside atmospheric clouds are investigated. The atmospheric clouds play a significant role in the evolution of weather and climate by impacting the energy and the hydrological cycle, incoming and outgoing solar radiations, and the local/global precipitation. However, there still exists many scientific questions regarding the initiation and the interactions in between the cloud particles themselves and with the in-cloud dynamical processes. In order to understand the growth of the inertial cloud droplets in the cloud edge mixing through the interface, which is an important process controlling the life cycle of the clouds, in the Chapter 2 a detailed investigation on the condensational/collisional growth of cloud droplets is presented using the pseudo-spectral direct numerical simulations. The initiation of the cloud particles/hydrometeors inside mature clouds is also a vast area of research, where the processes behind the activation or initiation of the cloud aerosols are also required to be investigated and parameterized. In the Chapter 3 of this thesis, a detailed investigation is conducted to understand the transport of fluid and scalar quantities in the wake of the large precipitating cloud hydrometeors using the direct numerical simulations, with application of the lattice Boltzmann method. Then in the Chapter 4, the methodology for the investigation of scalar transport in the wake of the hydrometeors is extended to understand the parameter space of the wake-induced supersaturation behind large precipitating hydrometeors. A detailed quantitative analysis on the Lagrangian trajectories of the aerosols is detailed also in the Chapter 4 to find the aerosol activation potential of these wake-induced supersauration behind the precipitating hydrometeors, and to investigate whether, this process can produce new particles at such an extent, which is important for the cloud life cycle. The detailed conclusions of the chapters are given below.

In the Chapter 2, the understanding regarding the growth of the inertial cloud droplets in the transient mixing of horizontal cloud top interface is extended by the inclusion of gravitational sedimentation and a collision module for droplet-droplet collision together with the condensational/evaporative growth/shrink in size. Three

different mono-disperse initial cloud water droplet populations (25, 18 and 6 μm initial radius) have been simulated with the same initial background airflow conditions. A transient initial value problem is simulated, where the turbulent kinetic energy TKE inside the domain was initialized following the infield measurements of the TKE spectra in the ranges of the inertial sub-range and the dissipation range. The in-cloud measurements of the temperature and the water vapor density is replicated in the initial conditions of the same quantities. Although initialized with the same background flow condition, the droplet population are observed to undergo different transients, depending on their initial size. This chapter elaborates the differences in between the cloud droplet growth in the size gap from 15 μm to 40 μm of radius, and for the droplets smaller than 15 μm of radius. The results show that the small 6 μm radius droplets do not grow by collision. However, in the larger droplet populations of both the 25 μm and 18 μm radii, the collisional growth becomes important. Multiple collisions have occurred in between the different sizes of the droplets. The mixing in the cloud top and the adjacent clear air interface produced a size broadening of the initial mono-disperse population due to the supersaturation fluctuations. These local supersaturation fluctuations are more influential for the smaller population. Since the flow was decaying with time, the gravitational settling became more and more important for the larger population as the simulation evolved, leading to a gradual removal of the falling droplets from the simulation domain. On the contrary, the reduction in total droplet count for the 6 μm initial size population happened mostly due to the complete evaporation of the sub-micron sized droplets of this population. These droplets were very sensitive to local subsaturation due their very small size.

In order to find the impact of the stable, unstable or neutrally stratified airflow conditions on the transient evolution of the initial mono-disperse cloud droplet populations, 9 simulations are conducted with the same initial mono-disperse 20 μm radius droplet populations in the same initial flow conditions for the gradient of turbulent kinetic energy across the interface. However, the initial temperature and the density of water vapor conditions are varied to create three different initial stratification profiles and three different initial supersaturation profiles. The initial supersaturation conditions are varied as strong ($RH_{cloud} = 110\%$ and $RH_{air} = 40\%$), moderate ($RH_{cloud} = 110\%$ and $RH_{air} = 60\%$) and mild ($RH_{cloud} = 105\%$ and $RH_{air} = 85\%$). The probability distribution of the droplet sizes shows that the widening in the initial droplet size increases with the increase in the supersaturation gradient between the cloud and the clear air. Whereas, the temperature stratification profile has significant influence on the droplet size broadening. The unstably stratified airflow conditions result in increased mixing across the initial interface, which widens the droplet size distribution at the highest amount for all the supersaturation gradients. On the contrary, the stably stratified conditions inhibit the mixing across the interface, and therefore, are observed to result in the least broadening in the droplet size distribution. The neutrally stratified condition,

whereas, produces a moderate broadening in between the limits of the droplet size ranges observed for the stable and the unstably stratified airflow conditions.

It must be noted that vertical extents of the simulated domains are $0.5\,\mathrm{m}$ and $1\,\mathrm{m}$, which is one order of magnitude smaller than the actual cloud interface observed by the in-cloud measurements. Whereas, the initial interface region of the simulation domain is $6 \times 10^{-3}\,\mathrm{m}$, which is $\sim 10^3$ times smaller than the actual cloud interfaces. Therefore, the numerical simulations at present is far from simulating actual cloud interfaces. However, numerical simulations still give important insights on the dynamical and thermodynamical evolution of the cloud droplets, that are important for understanding the cloud behavior. To extend this research, studies using the direct numerical simulations with various initial polydisperse droplet population representative of the in-cloud droplet measurements are foreseen. This will help to understand the process of rapid broadening of the droplets inside the size gap due to collisional growth. Similar to cloud top interfaces, simulations are foreseen to study the droplet dynamics in the horizontal cloud interfaces where gravitational force and buoyancy plays a different role on cloud droplet evolution. Also an innovative model in the simulation setup for such interface mixing simulations must be introduced to take care of the removal of the larger size droplets from the lower boundary of the domain due to the gravitational settling, in order to avoid the reduction of droplet samples near the lower domain boundary. A further analysis could also introduce a constant rate of TKE inflow inside both the cloudy region as well as the clear air region of the domain, so that the total TKE inside the simulation domain remains a constant, which could be used to simulate the precipitating clouds.

On the other hand, to understand the transport of the fluids and scalars in the wake of the cloud hydrometeors, a detailed numerical analysis is presented in the Chapter 3 on the spatial structure of the wake flow. A novel population density distribution approach is presented for the various Reynolds number in the steady wake regime. The incompressible Navier-Stokes equation is solved for the flow velocity and the one-way coupled advection-diffusion equations are solved for the scalars using the lattice Boltzmann method. The spatial evolution of various flow quantities, such as, longitudinal velocity component u, pressure p, passive scalar θ, convective scalar flux $\dot{Q}$ in the wake of the steady axisymmetric regime ($Re \leq 220$) and the oblique regime ($225 \leq Re \leq 285$) using a population distribution function N, shows a Lorentzian distribution which is proportional to the inverse of the square of the flow quantity (for example, $N(\dot{Q}) \propto \dot{Q}^{-2}$). This Lorentzian trend exhibits an algebraic decay in the number density of populations with different magnitudes of fluid quantities from the external ambient to the boundary layer in the wake and dominates the spatial distribution of the flow quantities outside the recirculating region. Transition to the oblique wake regime at $Re \geq 225$ in the simulations shows a complex three dimensional spatial evolution of the flow quantities, which also shows an overall Lorentzian trend. The population density distribution for

105

the longitudinal velocity component u, shows an increase in its number density with the increasing Re, evidencing an increase in the dimensionless kinetic energy. Whereas the number density of the scalar populations remains the same for various Re, which produces a steady axisymmetric wake. This feature however changes in case of the convective scalar flux, where an increase is observed in its number density with the increase in Re.

Descriptive statistics in the form of population density distribution of the fluid velocity and the transported scalar quantities in the wake of a sphere is important for understanding the transport and local reaction processes in specific regions of the wake. This is used in the Chapter 4 for understanding the microphysics of cloud droplets and aerosol interactions. A detailed analysis of the supersaturation field and aerosol activation around a spherical hydrometeor, which settles at its terminal velocity, for different atmospheric conditions is presented in the Chapter 4. The supersaturated volume V_S in the wake of a hydrometeor in the steady axisymmetric regime ($Re \leq 220$) and the oblique regime ($225 \leq Re \leq 285$) showed a $Re^{-0.63}$ decrease for the same thermodynamic conditions. V_S is seen to be very sensitive to the temperature difference ΔT between the hydrometeor and the ambient and its relative humidity condition RH_∞, so that V_S at constant ΔT increases as RH_∞ increases. However, when RH_∞ is fixed, ΔT plays a crucial role in V_S, since without an adequate ΔT a negligible supersaturated volume is generated. In addition, the warmer hydrometeors are observed to produce larger V_S than the colder ones.

The Lagrangian tracking of aerosols is also reported in the Chapter 4 to show how the complex flow pattern of the oblique wake allows some lucky aerosols to entrain within the recirculating wake. This phenomena resulted in a higher residence time for the entrained aerosols within the highly supersaturated vortical zone. Quantitatively within the supersaturated oblique wake of $Re = 285$, about 158 of finely introduced 977 tracers at a radial distance up to $r/d_p = 0.09$ showed residence time grater than $10^2 d_p/U_p$. Importantly, it is also estimated that such a long residence time within the highly supersaturated wake not only exposes the aerosols to a higher level of supersaturation compared to its nucleation barrier, but also provides enough time for the growth of the aerosol by deposition of water vapor to exceed its critical size, and therefore to be activated as a CCN and also sometimes as an INP, depending on various parameters. It is approximated that the wake-induced nucleation of aerosols during a convective precipitation of 20 minutes can generate $\mathcal{O}(10^3) - \mathcal{O}(10^6)\mathrm{m}^{-3}$ potentially new CCNs and possibly some fraction of aerosols can activate as INPs or become ice particles from the activated CCNs. This is in order of magnitude comparable to other secondary ice production mechanisms [51], and thus contribute to the life cycle of clouds.

To extend this research, direct numerical simulations with a comprehensive and integral incorporation of different interconnected physical and chemical in-cloud processes contributing to the activation of aerosols must be conducted. To quantify the impact of this wake-induced aerosol activation process on the life

cycle of a cloud, a rigorously intensive investigation should be conducted with the consideration of the chemical composition of the aerosols and its microphysical growth, together with the presence of the in-cloud turbulence and the models of the cloud scale updrafts.

End of Chapter 5

Appendix A

The Point Particle Model and the Dimensionless Parameters

The content of this appendix is adapted from the notes on the pseudo-spectral direct numerical simulations code (Iovieno, M., Personal Communication, December 11, 2017). In this physical model, the cloud droplets are considered as point-particles, with variable mass as one of its attributes. This simplification avoids the necessity to solve the details of the fluid flow around each single droplet, which makes this approach feasible for the simulations of more than a few droplets. However, there are justifications associated to it. 1.) One has to assume that the sizes of the particles are much smaller than the smallest flow scale which is the Kolmogorov scale in a turbulent flow. In this study, the diameter of the cloud droplets are in μm range, while the Kolmogorov scale is in mm range, and therefore it is justified to use the point-particles model. 2.) Also the concentration of the particles must be small in the ambient fluid, so that one particle does not interact directly with another neighboring particle. This means that the regions perturbed by the different particles do not overlap, so that each particle does not directly see the perturbation in the flow, which is induced by other particles. Basically, as shown in the Figure A.1, in case of a volume fraction of the particles $\leq 10^{-6}$ of the ambient fluid, the point-particles with one-way coupling is a valid model according to Elghobashi (1991) [31] for any range of particle Stokes number St, where fluids only perturb the particle trajectories but particles give negligible feedback to fluid. Whereas, for a volume fraction $\leq 10^{-3}$ but $> 10^{-6}$, one should consider point-particles with two-way coupling, where particles modify the structure of the turbulent flow field [33]. As shown in Figure A.1, in this regime, the particles can enhance kinetic energy production or dissipation, depending on its St. For a volume fraction $> 10^{-3}$, one should consider four-way coupling [31], where not only the feedback from the particles to the fluid counts, but also the particle to particle interaction should also be considered.
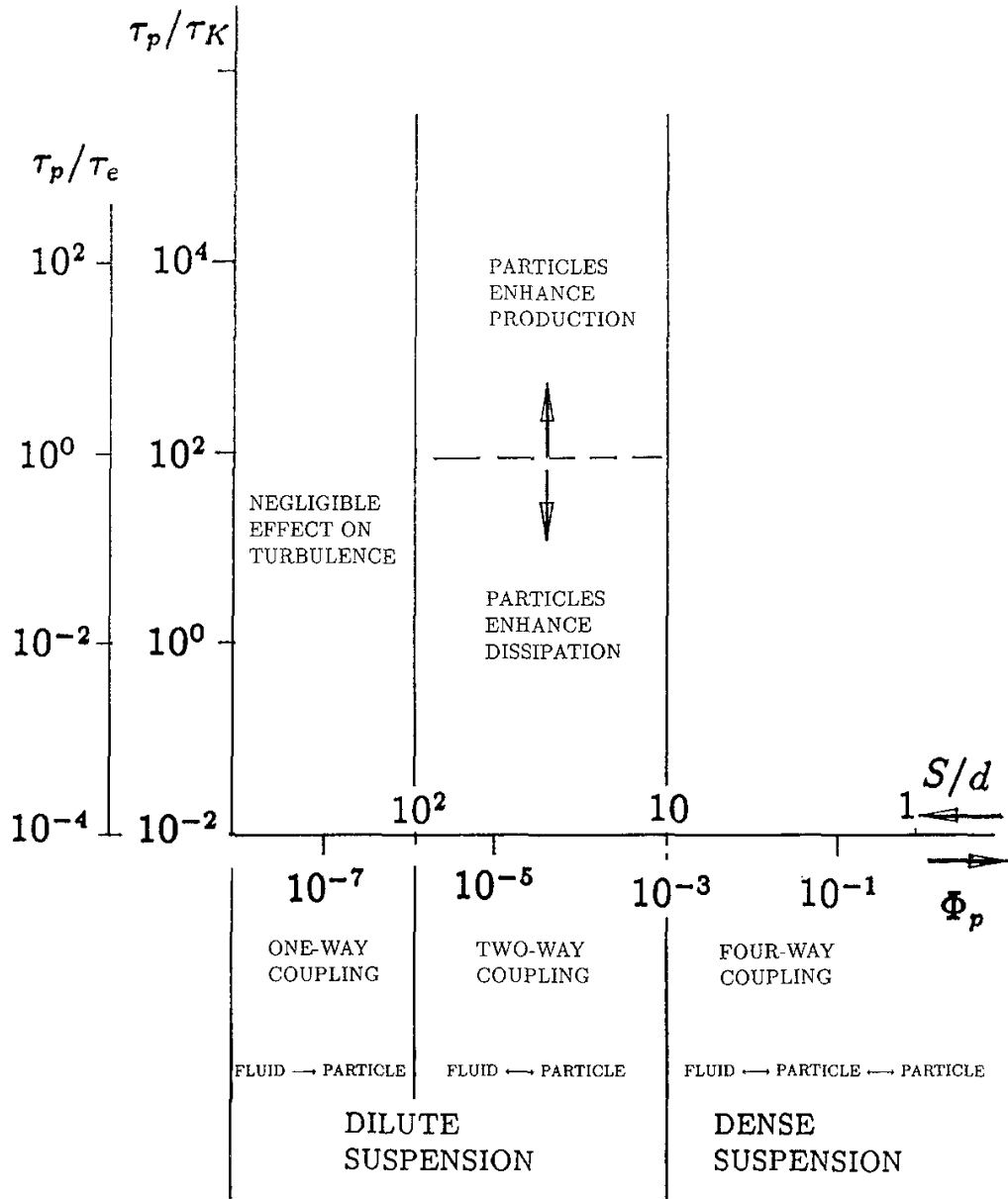
Figure A.1: Source: Elghobashi (1991) [31]. Various particle and fluid interaction regimes, depending on the volume fraction of the particles Φ_p, distance between the centers of the neighboring particles S, particle diameter d, particle response time τ_p, Kolmogorov time scale τ_K and the large eddy turnover time τ_e. This notation system is from the Elghobashi (1991) article [31] and only used for this figure.

A.1 Equation on the Diffusive Growth of Cloud Droplets

In order to find an equation for the diffusive growth of a cloud droplet, let us consider a water droplet to have a radius $r_p(t)$ and a temperature $T_p(t)$, which changes over time t. Also let us assume that the ambient around this droplet is supersaturated at temperature T_∞ and have a density of water vapor $\rho_{v,\infty}$. Since that droplet has a radius much smaller than the Kolmogorov microscale η, one can assume that the droplet sees a uniform environment. If the difference of velocity between the droplet and the surrounding air is negligible (which is true for the μm size droplets with negligible Stokes number St with respect to the cloudy ambient), one can write the energy balance equation and the water vapor transport equations in a frame moving with the droplet and the surrounding air is still, as:

$$\frac{\partial T}{\partial t} = \kappa \nabla^2 T, \text{ where } \begin{cases} T = T_p(t), & \text{when } r = r_p(t) \\ T = T_\infty, & \text{when } r \to \infty \end{cases}$$

$$\frac{\partial \rho_v}{\partial t} = \kappa_v \nabla^2 \rho_v, \text{ where } \begin{cases} \rho_v = \rho_{vs}(T_p(t)), & \text{when } r = r_p(t) \\ \rho_v = \rho_{v,\infty}, & \text{when } r \to \infty. \end{cases}$$

Here, r is the radial distance from the center of the droplet and $\rho_{vs}(T_p)$ is the density of saturated water vapor at the surface of the droplet which is considered to be saturated at temperature T_p according the Maxwell diffusion model (also described in the Chapter 4). κ and κ_v are the thermal diffusivity and the water vapor diffusivity of air respectively.

Since the characteristic time of diffusion on scales of order r_p is much smaller than the characteristic time of the droplet growth by the condensation of water vapor, the ambient temperature and vapor density fields adjust almost instantaneously to the size/temperature variations of the droplet. Therefore, one can consider a quasi–steady evolution in the temperature and vapor density fields, as:

$$\nabla^2 T = 0, \text{ where } \begin{cases} T = T_p(t), & \text{when } r = r_p(t) \\ T = T_\infty, & \text{when } r \to \infty \end{cases}$$

$$\nabla^2 \rho_v = 0, \text{ where } \begin{cases} \rho_v = \rho_{vs}(T_p(t)), & \text{when } r = r_p(t) \\ \rho_v = \rho_{v,\infty}, & \text{when } r \to \infty. \end{cases}$$

The solutions of these equations can be written as:

$$\frac{T(r,t) - T_\infty}{T_p(t) - T_\infty} = \frac{r_p(t)}{r},$$

$$\frac{\rho_v(r,t) - \rho_{v,\infty}}{\rho_{vs}(T_p(t)) - \rho_{v,\infty}} = \frac{r_p(t)}{r}.$$

Now, if we consider the mass flux around the droplet as $\mathrm{d}m_p/\mathrm{d}t$, it should be equal to the change in the liquid water content of this droplet and will be equal to the vapor mass flow with the ambient. Therefore, one can write:

$$\frac{\mathrm{d}m_p}{\mathrm{d}t} = 4\pi r_p^2 \rho_L \frac{\mathrm{d}r_p}{\mathrm{d}t} = 4\pi r^2 \kappa_v \frac{\partial \rho_v}{\partial r}$$
$$\Rightarrow r_p^2 \frac{\mathrm{d}r_p}{\mathrm{d}t} = \frac{\kappa_v}{\rho_L} \partial \rho_v \frac{r^2}{\partial r}.$$

Here, ρ_L is the density of liquid water. After integrating this equation from $r \to \infty$ to $r = r_p$, one gets:

$$r_p^2 \frac{\mathrm{d}r_p}{\mathrm{d}t} = \frac{\kappa_v}{\rho_L}(\rho_{v,\infty} - \rho_{vs}(T_p))r_p$$
$$\Rightarrow r_p \frac{\mathrm{d}r_p}{\mathrm{d}t} = \frac{\kappa_v}{\rho_L}(\rho_{v,\infty} - \rho_{vs}(T_p)). \tag{A.1}$$

Now one has to consider the variation in the internal energy of the droplet, which is contributed due to the conductive heat flow through the droplet surface and the latent heat release by the condensating vapor. Therefore, considering the conductive heat flux as $\lambda_T \partial T / \partial r$ and the latent heat release equal to the latent heat for the phase change L times the amount of the condensating mass on the droplet, one can write:

$$m_p c_{p,w} \frac{\mathrm{d}T_p}{\mathrm{d}t} = 4\pi r^2 \left(\lambda_T \frac{\partial T}{\partial r} + L\kappa_v \frac{\partial \rho_v}{\partial r} \right).$$

Here, $c_{p,w}$ is the specific heat of water at constant pressure, L is the latent heat for phase change, $\lambda_T = \kappa \rho_a c_{p,a}$ is the thermal conductivity of air, κ is the thermal diffusivity, ρ_a is the density of air, $c_{p,a}$ is the specific heat of air at constant pressure. Now considering the thermal capacity of the droplet very small (the left hand side), compared to the latent heat release term in the right hand size, one can write:

$$\lambda_T \frac{\partial T}{\partial r} + L\kappa_v \frac{\partial \rho_v}{\partial r} = 0.$$

After integrating this equation from $r \to \infty$ to $r = r_p$, one gets:

$$\lambda_T(T_\infty - T_p)\frac{1}{r_p} = -L\kappa_v(\rho_{v,\infty} - \rho_{vs}(T_p))\frac{1}{r_p}$$
$$\Rightarrow (T_p - T_\infty) = \frac{L\kappa_v}{\lambda_T}(\rho_{v,\infty} - \rho_{vs}(T_p)).$$

We need to find a derivation for $(\rho_{v,\infty} - \rho_{vs}(T_\infty))$ so that one can write the Equation A.1 as a function of the ambient relative humidity $\varphi_\infty = \rho_{v,\infty}/\rho_{vs}(T_\infty)$.

In order to do this, the Clausius-Clapeyron equation will be used to find an approximate solution of $\rho_{vs}(T_\infty)$. If the partial pressure of the saturated water vapor in the air is $p_{vs}(T_p)$, exerted due to the density of saturated water vapor $\rho_{vs}(T_p)$ at the T_p temperature of the droplet, one can write from the ideal gas law that:

$$\rho_{vs}(T_p) = \frac{p_{vs}(T_p)}{R_v T_p},$$

where, R_v is the specific gas constant for water vapor. According to the Clausius-Clapeyron equation, the saturated vapor pressure p_{vs} is only a function of the temperature, and the tangent of the pressure-temperature diagram can be deduced as:

$$\frac{\mathrm{d}p_{vs}}{\mathrm{d}T} = \frac{L}{T\Delta v} \simeq \frac{L\rho_{vs}}{T} = \frac{Lp_{vs}}{R_v T^2}.$$

Here, Δv is the specific volume change due to the phase transition, which is approximated as $1/\rho_{vs}$.

In order to find an equation for $\rho_{vs}(T_\infty)$, one can linearize the partial vapor pressure $p_{vs}(T_\infty)$ considering that $(T_p - T_\infty)/T_\infty << 1$. Therefore, one can write:

$$p_{vs}(T_p) \simeq p_{vs}(T_\infty) + \left.\frac{\mathrm{d}p_{vs}}{\mathrm{d}T}\right|_{T_\infty}(T_p - T_\infty)$$

$$= p_{vs}(T_\infty) + \frac{Lp_{vs}(T_\infty)}{R_v T_\infty^2}(T_p - T_\infty)$$

$$\Rightarrow \rho_{vs}(T_p) = \frac{p_{vs}(T_p)}{R_v T_p} \simeq \frac{p_{vs}(T_p)}{R_v T_\infty}$$

$$= \frac{1}{R_v T_\infty}\left[p_{vs}(T_\infty) + \frac{Lp_{vs}(T_\infty)}{R_v T_\infty^2}(T_p - T_\infty)\right]$$

$$= \rho_{vs}(T_\infty) + \frac{L\rho_{vs}(T_\infty)}{R_v T_\infty^2}(T_p - T_\infty)$$

$$= \rho_{vs}(T_\infty) + \frac{L\rho_{vs}(T_\infty)}{R_v T_\infty^2}\frac{L\kappa_v}{\lambda_T}(\rho_{v,\infty} - \rho_{vs}(T_p))$$

$$\Rightarrow \rho_{vs}(T_p) = \left[\rho_{vs}(T_\infty) + \frac{L\rho_{vs}(T_\infty)}{R_v T_\infty^2}\frac{L\kappa_v}{\lambda_T}\rho_{v,\infty}\right]\left(1 + \frac{L^2\rho_{vs}(T_\infty)}{R_v T_\infty^2}\frac{\kappa_v}{\lambda_T}\right)^{-1}$$

Therefore, using the Clausius-Clapeyron equation, one can approximate that:

$$(\rho_{v,\infty} - \rho_{vs}(T_p)) = \rho_{v,\infty} - \left[\rho_{vs}(T_\infty) + \frac{L\rho_{vs}(T_\infty)}{R_v T_\infty^2}\frac{L\kappa_v}{\lambda_T}\rho_{v,\infty}\right]\left(1 + \frac{L^2\rho_{vs}(T_\infty)}{R_v T_\infty^2}\frac{\kappa_v}{\lambda_T}\right)^{-1}$$

$$= \left[\rho_{v,\infty} + \frac{L\rho_{vs}(T_\infty)}{R_v T_\infty^2}\frac{L\kappa_v}{\lambda_T}\rho_{v,\infty} - \rho_{vs}(T_\infty) - \frac{L\rho_{vs}(T_\infty)}{R_v T_\infty^2}\frac{L\kappa_v}{\lambda_T}\rho_{v,\infty}\right]\left(1 + \frac{L^2\rho_{vs}(T_\infty)}{R_v T_\infty^2}\frac{\kappa_v}{\lambda_T}\right)^{-1}$$

Therefore, one gets a derivation for $(\rho_{v,\infty} - \rho_{vs}(T_p))$ as a function of $(\rho_{v,\infty} - \rho_{vs}(T_\infty))$:

$$(\rho_{v,\infty} - \rho_{vs}(T_p)) = (\rho_{v,\infty} - \rho_{vs}(T_\infty)) \left(1 + \frac{L^2 \rho_{vs}(T_\infty)}{R_v T_\infty^2} \frac{\kappa_v}{\lambda_T}\right)^{-1}.$$

Therefore, the Equation A.1, can be re-written as:

$$r_p \frac{\mathrm{d}r_p}{\mathrm{d}t} = \kappa_v \frac{\rho_{vs}(T_\infty)}{\rho_L} \left(\frac{\rho_{v,\infty}}{\rho_{vs}(T_\infty)} - 1\right) \left(1 + \frac{L^2 \rho_{vs}(T_\infty)}{R_v T_\infty^2} \frac{\kappa_v}{\lambda_T}\right)^{-1}$$

$$\Rightarrow r_p \frac{\mathrm{d}r_p}{\mathrm{d}t} = C(\varphi_\infty - 1) \tag{A.2}$$

$$\text{where, } C = \kappa_v \frac{\rho_{vs}(T_\infty)}{\rho_L} \left(1 + \frac{L^2 \rho_{vs}(T_\infty)}{R_v T_\infty^2} \frac{\kappa_v}{\lambda_T}\right)^{-1}$$

$$\text{and, } \varphi_\infty = \frac{\rho_{v,\infty}}{\rho_{vs}(T_\infty)}, \text{ is the ambient relative humidity.}$$

A.2 The Navier-Stokes Equations with Boussinesq approximation

Boussinesq approximation is applicable only in the case of natural convection, when the modulus of density variation $\Delta\rho/\rho_0$ is negligible ($\Delta\rho/\rho_0 << 1$) [145, 86]. The Navier-Stokes (NS) equations for the motion of the compressibe fluid is written as:

$$\rho \left(\frac{\partial \mathbf{u}}{\partial t} + \mathbf{u} \cdot \nabla \mathbf{u}\right) = -\nabla p + \nabla \cdot \left(\mu \left(\nabla \mathbf{u} + (\nabla \mathbf{u})^T\right) - \frac{2}{3}\mu \left(\nabla \cdot \mathbf{u}\right) \mathbf{I}\right) + \rho \mathbf{g}, \tag{A.3}$$

where, $\mathbf{I}$ is the identity matrix. This NS equations are complemented with the continuity equation, as:

$$\frac{1}{\rho} \frac{D\rho}{Dt} + \nabla \cdot \mathbf{u} = 0 \tag{A.4}$$

According to the Boussinesq approximation, the variation in density is only considered when it is multiplied with the gravitational acceleration. Therefore, in the continuity equation, the density variation term is neglected, considering it is negligible than the $\nabla \cdot \mathbf{u}$. Also the $-2/3\mu(\nabla \cdot \mathbf{u})\mathbf{I}$ term is also zero for the incompressible fluid, and the diffusion term $\nabla \cdot (\mu(\nabla \mathbf{u} + (\nabla \mathbf{u})^T))$ turns into $\mu\nabla^2\mathbf{u}$. As a result, the continuity and the NS equations for the incompressible fluid motion are written as:

$$\nabla \cdot \mathbf{u} = 0, \tag{A.5}$$

$$\rho_0 \left(\frac{\partial \mathbf{u}}{\partial t} + \mathbf{u} \cdot \nabla \mathbf{u}\right) = -\nabla p + \mu\nabla^2\mathbf{u} + (\rho_0 + \Delta\rho)\,\mathbf{g}, \tag{A.6}$$

where, the density variation $\Delta\rho$, which is defined in the equation A.12 for humid air, is only used in the buoyancy term in multiplication with **g**. Whereas, for the all other terms, instead of $\rho = \rho_0 + \Delta\rho$, only ρ_0 is considered. Considering the hydrostatic pressure is $\rho_0 g h$, where h is the elevation of the air parcle, the $-\nabla p + \rho_0 g$ is replaced with only $-\nabla p$, where p is the atmospheric pressure at the elevation of the air parcel. Therefore, by considering that the buoyancy term $B = -\Delta\rho/\rho_0$ and the kinamatic viscosity $\nu = \mu/\rho_0$, one can write the NS equations as:

$$\frac{\partial \mathbf{u}}{\partial t} + \mathbf{u} \cdot \nabla \mathbf{u} = -\frac{1}{\rho_0}\nabla p + \nu \nabla^2 \mathbf{u} - B\mathbf{g} \tag{A.7}$$

A.3 The Buoyancy Term in the Navier-Stokes equations

Here the state of equation for humid air is presented. If ρ is the humid air density, p is its pressure, $\mathcal{M}$ is the molar mass, and q is the mixing ratio, then:

$$\begin{aligned}
\rho = \rho_a + \rho_v &= \frac{p_a}{R_a T} + \frac{p_v}{R_v T} \\
&= \frac{p - p_v}{R_a T} + \frac{p_v}{R_v T} = \frac{p}{R_a T} - \frac{p_v}{R_a T} + \frac{p_v}{R_v T} \\
&= \frac{p}{R_a T}\left[1 - \frac{p_v}{p}\left(1 - \frac{R_a}{R_v}\right)\right].
\end{aligned} \tag{A.8}$$

Where, ρ_a is the density of the dry air, ρ_v is the density of the water vapor, p_a and p_v are respectively the partial pressure due to dry air and the water vapor, R_a and R_v are respectively the gas constants for the dry air and the water vapor.

Now considering that $q = \rho_v/\rho_a$, $R_a = R/\mathcal{M}_a$, $R_v = R/\mathcal{M}_v$ (where $\mathcal{M}_a$ and $\mathcal{M}_v$ are the molar mass of the dry air and water vapor/water respectively, and R is the universal gas constant), $p_a = \rho_a R_a T$ and $p_v = \rho_v R_v T$, one gets:

$$\frac{p_v}{p} \simeq \frac{p_v}{p_a} = \frac{\rho_v R_v}{\rho_a R_a} = \frac{\rho_v}{\rho_a}\frac{\mathcal{M}_a}{\mathcal{M}_v} = q\frac{\mathcal{M}_a}{\mathcal{M}_v},$$

which is replaced in the equation A.8. Therefore, one gets:

$$\begin{aligned}
\rho &= \frac{p}{R_a T}\left[1 - q\frac{\mathcal{M}_a}{\mathcal{M}_v}\left(1 - \frac{\mathcal{M}_v}{\mathcal{M}_a}\right)\right] \\
&= \frac{p}{R_a T}\left[1 - q\left(\frac{\mathcal{M}_a}{\mathcal{M}_v} - 1\right)\right] \\
&= \frac{p}{R_a T}\left[1 - q\epsilon\right].
\end{aligned} \tag{A.9}$$

Here $\epsilon = \mathcal{M}_a/\mathcal{M}_v - 1 = R_v/R_a - 1 = 0.608$ is the constant defined above. The equation A.9 is the state of equation for humid air.

If one take partial derivative of ρ with respect to T and q, it is:

$$\frac{\partial \rho}{\partial T} = -\frac{p}{R_a T^2}\left[1 - q\epsilon\right] = -\frac{\rho}{T} \tag{A.10}$$

$$\frac{\partial \rho}{\partial q} = \frac{p}{R_a T}(-\epsilon) = -\rho\frac{\epsilon}{1 - q\epsilon} \simeq -q\epsilon \tag{A.11}$$

The buoyancy B term models the impact of density variation as $-\Delta\rho/\rho_0$ according to the Boussinesq approximation. In this approximation, any variations in the fluid properties are ignored, but only the density variation is considered when it is multiplied with the gravitational acceleration g [145]. The variation in ρ is considered due to the fluctuations in T and ρ_v, as $\rho(T, \rho_v)$ or $\rho(T, q)$. Therefore, the Taylor expansion of $\Delta\rho$ is:

$$\begin{aligned}
\Delta\rho &= \left.\frac{\partial\rho}{\partial T}\right|_0 \Delta T + \left.\frac{\partial\rho}{\partial q}\right|_0 \Delta q \\
&= -\frac{\rho_0}{T_0}\Delta T + (-\rho_0\epsilon)\Delta q \\
\frac{\Delta\rho}{\rho_0} &= -\left[\frac{\Delta T}{T_0} + \epsilon\,(q - q_0)\right] \\
B &= -\frac{\Delta\rho}{\rho_0} = \frac{T - T_0}{T_0} + \epsilon\frac{\rho_v - \rho_{v,e}}{\rho_0}.
\end{aligned} \tag{A.12}$$

Here, ρ_0 and T_0 are the reference air density and reference air temperature respectively. While $q_0 = \rho_{v,e}/\rho_0$ is the reference mixing ratio, where $\rho_{v,e}$ is the reference density of the water vapor which is the saturated density of water vapor at T_0, later mentioned as $\rho_{vs}(T_0)$.

A.4   The Vaillancourt model

The numerical model used in the Chapter 2 is the standard model, which is described by Vaillancourt et al. (2001) [148], and is later used by almost all the recent numerical simulation on the cloud microphysics of the cloud droplets [77, 78, 110, 43, 80]. In the following, along with the dimensional model, the dimensionless/normalized equations are also deduced which are used in the numerical code. For the solution of the fluid flow, the Vaillancourt model considers the Navier-Stokes (NS) equations for the humid air, coupled with the Lagrangian tracking of every cloud droplets.

A.4.1   The Governing Equations for Fluid Flow

The air phase equation use a Boussinesq-like approximation for the fluid velocity $\mathbf{u} = (u_1, u_2, u_3)$ and include the equations for the temperature T and the vapor density ρ_v which are essentially considered the active scalars. The governing equations for the airflow representing the cloudy air as the carrier fluid are presented below.

$$\nabla \cdot \mathbf{u} = 0, \tag{A.13}$$

$$\frac{\partial \mathbf{u}}{\partial t} + \mathbf{u} \cdot \nabla \mathbf{u} = -\frac{1}{\rho_0} \nabla p + \nu \nabla^2 \mathbf{u} - B\mathbf{g}, \tag{A.14}$$

$$\frac{\partial T}{\partial t} + \mathbf{u} \cdot \nabla T = \kappa \nabla^2 T + \frac{L}{\rho_0 c_p} C_d, \tag{A.15}$$

$$\frac{\partial \rho_v}{\partial t} + \mathbf{u} \cdot \nabla \rho_v = \kappa_v \nabla^2 \rho_v - C_d. \tag{A.16}$$

Here, ρ_0 is reference mass density of air at temperature T_0 and pressure p_0, ∇p is the pressure gradient, ν is the kinematic viscosity, $\mathbf{g} = (0,0,-g)$ is the gravitational acceleration, κ is the thermal diffusivity of air, L is the latent heat for condensation of water vapor, c_p is the specific heat at constant pressure, and κ_v is the water vapor diffusivity.

The 'source' terms in the temperature (enthalpy) and humidity equations are:

C_d = condensation rate (condensating mass per unit time and volume),

B = buoyancy term, i.e. $B\mathbf{g}$ is the buoyancy force per unit mass.

The B term includes the effects of 1.) temperature perturbation, 2.) perturbation in the density of the water vapor, and 3.) the drag of the droplets on the flow.

These feedback terms are expressed as:

$$C_d = \frac{1}{V} \sum_i \frac{\mathrm{d}m_i}{\mathrm{d}t} = \frac{1}{V} \sum_i 4\pi \rho_L r_i^2 \frac{\mathrm{d}r_i}{\mathrm{d}t}$$

$$B = \frac{T - T_0}{T_0} + \epsilon \frac{\rho_v - \rho_{v,e}}{\rho_0}$$

where, the sum in C_d is only on all particles within the (small) volume V (in practice a computational grid cell). T_0 is the reference temperature, $\rho_{v,e}$ is the reference density of the water vapor, $\epsilon = R_v/R_a - 1 = 0.608$ is a constant dependent on the gas constants R_v and R_a of the water vapor and the air respectively, ρ_L is the density of liquid water, and r_i is the radius of the i-th cloud droplet.

A.4.2   The Point Particle Equations

The governing equations for the cloud droplets in the ambient cloudy air are presented below. The equations for the i-th particle are:

$$\frac{\mathrm{d}\mathbf{x}_i}{\mathrm{d}t} = \mathbf{v}_i, \tag{A.17}$$

$$\frac{\mathrm{d}\mathbf{v}_i}{\mathrm{d}t} = -\frac{\mathbf{v}_i - \mathbf{u}(\mathbf{x}_i, t)}{\tau_i} + \mathbf{g}, \tag{A.18}$$

$$\frac{\mathrm{d}r_i}{\mathrm{d}t} = C \frac{\varphi(\mathbf{x}_i, t) - 1}{r_i}, \quad \varphi(\mathbf{x}_i, t) = \frac{\rho_v(\mathbf{x}_i, t)}{\rho_{vs}(T)(\mathbf{x}_i, t)}, \tag{A.19}$$

where $\mathbf{x}_i$ is the droplet position, $\mathbf{v}_i$ is the droplet velocity, φ is the local relative humidity, ρ_{vs} is the density of saturation vapor. Coefficient τ_i is the is the response time for the i-th droplet, which is:

$$\tau_i = \frac{2}{9} \frac{\rho_L}{\rho_0} \frac{r_i^2}{\nu}. \tag{A.20}$$

Therefore, τ_i changes if the droplet grows or evaporates. And the C is a model coefficient, actually a function for the flow around the particle and it is defined as:

$$C = \kappa_v \frac{\rho_{vs}(T_0)}{\rho_L} \left(1 + \frac{L^2 \rho_{vs}(T_0)}{R_v T_0^2} \frac{\kappa_v}{\lambda_T} \right)^{-1}, \tag{A.21}$$

where λ_T is the thermal conductivity of the air.

A.5 The Dimensionless equations

In order to non-dimensionalize the physical model, various reference quantities are introduced. A reference length L_R, and a reference velocity U_R is chosen, from which the reference time $T_R = L_R/U_R$ is deduced. The reference thermodynamic quantities are T_0, p_0 and ρ_0, respectively for the temperature, pressure and the density of the ambient. The reference quantity in the density of water vapor $\rho_{v,e}$ for the ambient is chosen to be the saturated vapor density at ambient temperature T_0; that is $\rho_{v,e} = \rho_{vs}(T_0)$. An index '0' will refer to the ambient reference conditions, unless specified as something different. Therefore, here are the dimensionless quantities:

$$\tilde{\mathbf{x}} = \frac{\mathbf{x}}{L_R}, \qquad\qquad \tilde{\mathbf{u}} = \frac{\mathbf{u}}{U_R} \quad \text{and analogously} \quad \tilde{\mathbf{v}} = \frac{\mathbf{v}}{U_R},$$

$$\tilde{T} = \frac{T - T_0}{T_0}, \qquad \tilde{p} = \frac{p - p_0}{\rho_0 U_R^2}, \qquad \tilde{r} = \frac{r}{L_R}, \qquad \tilde{\rho}_v = \frac{\rho_v}{\rho_{vs}(T_0)}.$$

Therefore the equations (A.13-A.16) will become:

$$\tilde{\nabla} \cdot \tilde{\mathbf{u}} = 0, \tag{A.22}$$

$$\frac{\partial \tilde{\mathbf{u}}}{\partial \tilde{t}} + \tilde{\mathbf{u}} \cdot \tilde{\nabla}\tilde{\mathbf{u}} = -\tilde{\nabla}\tilde{p} + \frac{\nu}{U_R L_R}\tilde{\nabla}^2\tilde{\mathbf{u}} + \frac{g L_R}{U_R^2}\tilde{B}\mathbf{e}_z, \tag{A.23}$$

$$\frac{\partial \tilde{T}}{\partial \tilde{t}} + \tilde{\mathbf{u}} \cdot \tilde{\nabla}\tilde{T} = \frac{\kappa}{U_R L_R}\tilde{\nabla}^2\tilde{T} + \frac{L}{c_p T_0}\frac{\rho_L}{\rho_0}\tilde{C}_d, \tag{A.24}$$

$$\frac{\partial \tilde{\rho}_v}{\partial \tilde{t}} + \tilde{\mathbf{u}} \cdot \tilde{\nabla}\tilde{\rho}_v = \frac{\kappa_v}{U_R L_R}\tilde{\nabla}^2\tilde{\rho}_v - \frac{\rho_L}{\rho_{vs}(T_0)}\tilde{C}_d. \tag{A.25}$$

Here the dimensionless buoyancy term $\tilde{B}$, condensation rate $\tilde{C}_d$ and the unit vector $\mathbf{e}_z$ are written as:

$$\tilde{B} = \tilde{T} + \epsilon\frac{\rho_{vs}(T_0)}{\rho_0}\left(\tilde{\rho}_v - 1\right),$$

$$\tilde{C}_d = \frac{1}{\tilde{V}}\sum_i 4\pi\tilde{r}_i^2\frac{\mathrm{d}\tilde{r}_i}{\mathrm{d}\tilde{t}},$$

$$\mathbf{e}_z = (0,0,1).$$

Also the dimensionless equations for each particle will become:

$$\frac{\mathrm{d}\tilde{\mathbf{x}}_i}{\mathrm{d}\tilde{t}} = \tilde{\mathbf{v}}_i, \tag{A.26}$$

$$\frac{\mathrm{d}\tilde{\mathbf{v}}_i}{\mathrm{d}\tilde{t}} = -\frac{\tilde{\mathbf{v}}_i - \tilde{\mathbf{u}}(\tilde{\mathbf{x}}_i, \tilde{t})}{\tilde{\tau}_i} - \frac{g L_R}{U_R^2}\mathbf{e}_z, \tag{A.27}$$

$$\frac{\mathrm{d}\tilde{r}_i}{\mathrm{d}\tilde{t}} = \frac{C}{U_R L_R}\frac{\varphi(\tilde{\mathbf{x}}_i, \tilde{t}) - 1}{\tilde{r}_i}, \qquad \varphi(\tilde{\mathbf{x}}_i, \tilde{t}) = \frac{\tilde{\rho}_v(\tilde{\mathbf{x}}_i, \tilde{t})}{\tilde{\rho}_{vs}(\tilde{T})(\tilde{\mathbf{x}}_i, \tilde{t})}. \tag{A.28}$$

Here $\tilde{\tau}_i = \tau_i/T_R$ is the dimensionless particle response time.

119

A.6   The Dimensionless parameters

Therefore, in the set of the dimensionless equations A.22 - A.28, the following dimensionless parameter are found which govern the dynamical evolution:

$$Re = \frac{U_R L_R}{\nu} \qquad \text{Reynolds number (convection/diffusion)}$$

$$Pr = \frac{\nu}{\kappa} \qquad \text{Prandtl number (momentum diffusivity/heat diffusivity)}$$

$$Sc = \frac{\nu}{\kappa_v} \qquad \text{vapor Schmidt number (momentum diffusivity/}$$
$$\text{vapor mass diffusivity)}$$

$$\alpha_a = \frac{\rho_L}{\rho_0} \qquad \text{ratio between liquid water density and air density}$$

$$\alpha_v = \frac{\rho_L}{\rho_{vs}(T_0)} \qquad \text{ratio between liquid water density and vapor density}$$

$$\alpha_{av} = \frac{\rho_{vs}(T_0)}{\rho_0} = \frac{\alpha_a}{\alpha_v} \qquad \text{ratio between vapor density and air density}$$

$$\alpha_F = \frac{g L_R}{U_R^2} \qquad \sim\text{weight/inertia} (\sim \text{proportional to inverse Froude number})$$

$$\beta = \frac{L}{c_p T_0} \qquad \text{a sort of inverse Sfefan number (condensation latent heat/}$$
$$\text{air enthalphy)}$$

One can rewrite the dimensionless equations A.22 - A.28 with the dimensionless parameters defined before. Therefore the model equations, by dropping the tildes˜ for the dimensionless forms will be:

$$\nabla \cdot \mathbf{u} = 0, \tag{A.29}$$

$$\frac{\partial \mathbf{u}}{\partial t} + \mathbf{u} \cdot \nabla \mathbf{u} = -\nabla p + \frac{1}{Re}\nabla^2 \mathbf{u} + \alpha_F B \mathbf{e}_z, \tag{A.30}$$

$$\frac{\partial T}{\partial t} + \mathbf{u} \cdot \nabla T = \frac{1}{Re\,Pr}\nabla^2 T - \beta \alpha_a C_d, \tag{A.31}$$

$$\frac{\partial \rho_v}{\partial t} + \mathbf{u} \cdot \nabla \rho_v = \frac{1}{Re\,Sc}\nabla^2 \rho_v - \alpha_v C_d. \tag{A.32}$$

The source terms are:

$$B = T + \epsilon \alpha_{av}(\rho_v - 1)$$

$$C_d = \frac{1}{V}\sum_i 4\pi r_i^2 \frac{\mathrm{d}r_i}{\mathrm{d}t}$$

And the dimensionless droplet equations are:

$$\frac{\mathrm{d}\mathbf{x}_i}{\mathrm{d}t} = \mathbf{v}_i, \tag{A.33}$$

$$\frac{\mathrm{d}\mathbf{v}_i}{\mathrm{d}t} = -\frac{\mathbf{v}_i - \mathbf{u}(\mathbf{x}_i, t)}{\tilde{\tau}_i} - \alpha_F \mathbf{e}_z, \tag{A.34}$$

$$\frac{\mathrm{d}r_i}{\mathrm{d}t} = C_* \frac{\varphi(\mathbf{x}_i, t) - 1}{r_i}, \quad \varphi(\mathbf{x}_i, t) = \frac{\rho_v(\mathbf{x}_i, t)}{\rho_{vs}(T)(\mathbf{x}_i, t)} \tag{A.35}$$

The new term C_*, which depends on the conditions around each droplet, is given by:

$$
\begin{aligned}
C_* &= \frac{C}{U_R L_R} = \frac{\kappa_v}{U_R L_R} \frac{\rho_{vs}(T_0)}{\rho_L} \left(1 + \frac{L^2 \rho_{vs}(T_0)}{R_v T_0^2} \frac{\kappa_v}{\lambda_T} \right)^{-1} \\
&= \frac{\nu}{U_R L_R} \frac{\kappa_v}{\nu} \frac{\rho_{vs}(T_0)}{\rho_L} \left(1 + \frac{L^2 \rho_{vs}(T_0)}{R_v T_0^2} \frac{\kappa_v}{\lambda_T} \right)^{-1} \\
&= \frac{1}{Re} \frac{1}{\alpha_v} \cdot Sc^{-1} \left(1 + \frac{L^2 \rho_{vs}(T_0)}{R_v T_0^2} \frac{\kappa_v}{\lambda_T} \right)^{-1} \\
&= \frac{1}{Re} \frac{1}{Sc_*} \frac{1}{\alpha_v}.
\end{aligned}
$$

In the last line, a 'modified' Schmidt number (in line with the 'modified' diffusivity by Kumar et al. (2013) [77]) for the water vapor is defined as:

$$Sc_* = Sc \left(1 + \frac{L^2 \rho_{vs}(T_0)}{R_v T_0^2} \frac{\kappa_v}{\lambda_T} \right).$$

The dimensionless relaxation time of a droplet $\tilde{\tau}_i$ is also another dimensionless quantity, such that:

$$
\begin{aligned}
\tilde{\tau}_i &= \frac{\tau_i}{T_R} = \frac{\tau_i U_R}{L_R} \\
&= \frac{2}{9} \frac{\rho_L}{\rho_0} \frac{\tilde{r}_i^2 L_R^2}{\nu} \frac{U_R}{L_R} \\
&= \frac{2}{9} \frac{\rho_L}{\rho_0} \frac{U_R L_R}{\nu} \tilde{r}_i^2 \\
&= \frac{2}{9} \alpha_a Re \, \tilde{r}_i^2.
\end{aligned}
$$

Dimensionless saturated water vapor density $\tilde{\rho}_{vs}$ at $\tilde{T}$ is also another dimensionless quantity which is approximated by the Clausius-Clapeyron law:

$$
\begin{aligned}
\tilde{\rho}_{vs}(\tilde{T}) &= \frac{\rho_{vs}(T)}{\rho_{vs}(T_0)} = \frac{1}{\rho_{vs}(T_0)} \frac{p_{vs}(T)}{R_v T} = \frac{1}{\rho_{vs}(T_0)} \frac{p_{vs}(T_0)}{R_v T} \exp\left(\frac{L}{R_v}\left(\frac{1}{T_0} - \frac{1}{T}\right)\right) \\
&= \frac{1}{\rho_{vs}(T_0)} \frac{p_{vs}(T_0)}{R_v T_0} \frac{1}{1+\tilde{T}} \exp\left(\frac{L}{R_v T_0}\left(\frac{T-T_0}{T}\right)\right) \\
&= \frac{1}{1+\tilde{T}} \exp\left(\frac{L}{c_p T_0} \frac{c_p}{R_v}\left(\frac{\tilde{T}}{1+\tilde{T}}\right)\right) \\
&= \frac{1}{1+\tilde{T}} \exp\left(\beta \frac{\gamma}{\gamma-1}\left(\frac{\tilde{T}}{1+\tilde{T}}\right)\right).
\end{aligned}
$$

Here, γ is the ratio of the specific heat capacities of water vapor at a constant pressure c_p and at a constant volume c_v, so that $\gamma \simeq 4/3$. And the R_v is the gas constant for the water vapor, so that $c_p - c_v = R_v$.

Bibliography

[1]   E. Adirosi et al. "Raindrop size distribution: Fitting performance of common theoretical models". In: *Advances in Water Resources* 96 (2016), pp. 290–305. ISSN: 0309-1708. DOI: 10.1016/j.advwatres.2016.07.010.

[2]   M. Andrejczuk et al. "Numerical Simulation of Cloud–Clear Air Interfacial Mixing". In: *Journal of the Atmospheric Sciences* 61.14 (2004), pp. 1726–1739. DOI: 10.1175/1520-0469(2004)061<1726:NSOCAI>2.0.CO;2.

[3]   M. Andrejczuk et al. "Numerical Simulation of Cloud–Clear Air Interfacial Mixing: Effects on Cloud Microphysics". In: *Journal of the Atmospheric Sciences* 63.12 (2006), pp. 3204–3225. DOI: 10.1175/JAS3813.1.

[4]   M. Andrejczuk et al. "Numerical Simulation of Cloud–Clear Air Interfacial Mixing: Homogeneous versus Inhomogeneous Mixing". In: *Journal of the Atmospheric Sciences* 66.8 (2009), pp. 2493–2500. DOI: 10.1175/2009JAS2956.1.

[5]   P. Bagchi, M.Y. Ha, and S. Balachandar. "Direct Numerical Simulation of Flow and Heat Transfer From a Sphere in a Uniform Cross-Flow ". In: *Journal of Fluids Engineering* 123.2 (2000), pp. 347–358. DOI: 10.1115/1.1358844.

[6]   P. Bagchi and K. Kottam. "Effect of freestream isotropic turbulence on heat transfer from a sphere". In: *Physics of Fluids* 20.7 (2008), p. 073305. DOI: 10.1063/1.2963138.

[7]   B.A. Baker. "On the Nucleation of Ice in Highly Supersaturated Regions of Clouds". In: *Journal of the Atmospheric Sciences* 48.16 (1991), pp. 1904–1907. DOI: 10.1175/1520-0469(1991)048<1905:OTNOII>2.0.CO;2.

[8]   M.B. Baker. "Cloud Microphysics and Climate". In: *Science* 276.5315 (1997), pp. 1072–1078. DOI: 10.1126/science.276.5315.1072.

[9]   T. Bhowmick and M. Iovieno. "Direct Numerical Simulation of a Warm Cloud Top Model Interface: Impact of the Transient Mixing on Different Droplet Population". In: *Fluids* 4.3 (2019). DOI: 10.3390/fluids4030144.

[10] T. Bhowmick et al. "Population Distribution in the Wake of a Sphere". In: *Symmetry* 12.9 (2020). DOI: 10.3390/sym12091498.

[11]   T. Bhowmick et al. "Supersaturation in the Wake of a Precipitating Hydrometeor and Its Impact on Aerosol Activation". In: *Geophysical Research Letters* 47.22 (2020). DOI: 10.1029/2020GL091179.

[12]   C. Bouka Biona et al. "Diurnal cycle of temperature and wind fluctuations within an African equatorial rain forest". In: *Agricultural and Forest Meteorology* 109.2 (2001), pp. 135–141. ISSN: 0168-1923. DOI: 10.1016/S0168-1923(01)00253-2.

[13]   M. Birouk and M.M. Abou Al-Sood. "Numerical Study of Sphere Drag Coefficient in Turbulent Flow at Low Reynolds Number". In: *Numerical Heat Transfer, Part A: Applications* 51.1 (2007), pp. 39–57. DOI: 10.1080/10407780600710227.

[14]   E. Bodenschatz. "Clouds resolved". In: *Science* 350.6256 (2015), pp. 40–41. DOI: 10.1126/science.aad1386.

[15]   E. Bodenschatz and M. Eckert. "Prandtl and the Göttingen school". In: *A Voyage Through Turbulence*. Ed. by P.A. Davidson et al. Cambridge University Press, 2011, pp. 40–100. DOI: 10.1017/CBO9781139018241.003.

[16]   E. Bodenschatz et al. "Can We Understand Clouds Without Turbulence?" In: *Science* 327.5968 (2010), pp. 970–971. ISSN: 0036-8075. DOI: 10.1126/science.1185138.

[17]   G. Boffetta et al. "The Eulerian description of dilute collisionless suspension". In: *EPL* 78.1 (2007), p. 14001. DOI: 10.1209/0295-5075/78/14001.

[18]   M. Carbone and M. Iovieno. "Application of the nonuniform fast fourier transform to the direct numerical simulation of two-way coupled particle laden flows". In: *WIT Transactions on Engineering Sciences* 120 (2018), pp. 237–253. DOI: 10.2495/AFM180241.

[19]   K.K Chandrakar et al. "Aerosol indirect effect from turbulence-induced broadening of cloud-droplet size distributions". In: *Proceedings of the National Academy of Sciences* 113.50 (2016), pp. 14243–14248. DOI: 10.1073/pnas.1612686113.

[20]   A. Chouippe et al. "Heat and water vapor transfer in the wake of a falling ice sphere and its implication for secondary ice formation in clouds". In: *New Journal of Physics* 21.4 (2019), p. 043043. DOI: 10.1088/1367-2630/ab0a94.

[21]   A. Cimarelli et al. "Spectral enstrophy budget in a shear-less flow with turbulent/non-turbulent interface". In: *Physics of Fluids* 27.12 (2015), p. 125106. DOI: 10.1063/1.4937433.

[22]   R. Clift and W.H. Gauvin. "Motion of entrained particles in gas streams". In: *The Canadian Journal of Chemical Engineering* 49.4 (1971), pp. 439–448. DOI: 10.1002/cjce.5450490403.

[23] R. Clift, J. Grace, and M. Weber. *Bubbles, Drops, and Particles*. Academic Press, 1978.

[24] J. Curtius. "Nucleation of atmospheric particles". In: *Eur. Phys. J. Conferences* 1 (2009), pp. 199–209. DOI: 10.1140/epjconf/e2009-00921-0.

[25] P.J. DeMott et al. "The Fifth International Workshop on Ice Nucleation phase 2 (FIN-02): laboratory intercomparison of ice nucleation measurements". In: *Atmospheric Measurement Techniques* 11.11 (2018), pp. 6231–6257. DOI: 10.5194/amt-11-6231-2018.

[26] S.C.R. Dennis, J.D.A. Walker, and J. D. Hudson. "Heat transfer from a sphere at low Reynolds numbers". In: *Journal of Fluid Mechanics* 60.2 (1973), pp. 273–283. DOI: 10.1017/S0022112073000169.

[27] B.J. Devenish et al. "Droplet growth in warm turbulent clouds". In: *Quarterly Journal of the Royal Meteorological Society* 138.667 (2012), pp. 1401–1429. DOI: 10.1002/qj.1897.

[28] U. Dusek et al. "Size Matters More Than Chemistry for Cloud-Nucleating Ability of Aerosol Particles". In: *Science* 312.5778 (2006), pp. 1375–1378. DOI: 10.1126/science.1125261.

[29] J.E. Dye and P.V. Hobbs. "The Influence of Environmental Parameters on the Freezing and Fragmentation of Suspended Water Drops". In: *Journal of the Atmospheric Sciences* 25.1 (1968), pp. 82–96. DOI: 10.1175/1520-0469(1968)025<0082:TIOEPO>2.0.CO;2.

[30] R. Eichhorn and S. Small. "Experiments on the lift and drag of spheres suspended in a Poiseuille flow". In: *Journal of Fluid Mechanics* 20.3 (1964), pp. 513–527. DOI: 10.1017/S0022112064001380.

[31] S. Elghobashi. "Particle-laden turbulent flows: direct simulation and closure models". In: *Appl. Sci. Res.* 48.3 (1991), pp. 301–314. ISSN: 1573-1987. DOI: 10.1007/BF02008202.

[32] S. Elghobashi and G.C. Truesdell. "Direct simulation of particle dispersion in a decaying isotropic turbulence". In: *Journal of Fluid Mechanics* 242 (1992), pp. 655–700. DOI: 10.1017/S0022112092002532.

[33] S. Elghobashi and G.C. Truesdell. "On the two-way interaction between homogeneous turbulence and dispersed solid particles. I: Turbulence modification". In: *Physics of Fluids A: Fluid Dynamics* 5.7 (1993), pp. 1790–1801. DOI: 10.1063/1.858854.

[34] F. Raes. "Take a glass of water [1]... - concepts from physical chemistry used in describing the behaviour of aerosol and cloud droplets -". In: *J. Phys. IV France* 139 (2006), pp. 63–80. DOI: 10.1051/jp4:2006139006.

[35] P.R. Field et al. "Secondary Ice Production: Current State of the Science and Recommendations for the Future". In: *Meteorological Monographs* 58 (2017), pp. 7.1–7.20. DOI: 10.1175/AMSMONOGRAPHS-D-16-0014.1.

[36] B. Fornberg. "Steady viscous flow past a sphere at high Reynolds numbers". In: *Journal of Fluid Mechanics* 190 (1988), pp. 471–489. DOI: 10.1017/S0022112088001417.

[37] S.K. Friedlander. "Mass and heat transfer to single spheres and cylinders at low Reynolds numbers". In: *AIChE Journal* 3.1 (1957), pp. 43–48. DOI: 10.1002/aic.690030109.

[38] N. Fukuta and H.J. Lee. "A Numerical Study of the Supersaturation Field around Growing Graupel". In: *Journal of the Atmospheric Sciences* 43.17 (1986), pp. 1833–1843. DOI: 10.1175/1520-0469(1986)043<1833:ANSOTS>2.0.CO;2.

[39] A Gagin. "The Effect of Supersaturation on the Ice Crystal Production by Natural Aerosols". In: *Journal de Recherches Atmosphériques* 6 (1972), pp. 175–185.

[40] L. Gallana et al. "Energy and water vapor transport across a simplified cloud-clear air interface". In: *Journal of Physics: Conference Series* 547 (June 2014). DOI: 10.1088/1742-6596/547/1/012042.

[41] Z. Gao et al. "Investigation of Turbulent Entrainment-Mixing Processes With a New Particle-Resolved Direct Numerical Simulation Model". In: *Journal of Geophysical Research: Atmospheres* 123.4 (2018), pp. 2194–2214. DOI: 10.1002/2017JD027507.

[42] C.H. Gibson, C.C. Chen, and S.C. Lin. "Measurements of turbulent velocity and temperature fluctuations in the wake of a sphere." In: *AIAA Journal* 6.4 (1968), pp. 642–649. DOI: 10.2514/3.4557.

[43] T. Gotoh, T. Suehiro, and I. Saito. "Continuous growth of cloud droplets in cumulus cloud". In: *New Journal of Physics* 18.4 (2016), p. 043042. DOI: 10.1088/1367-2630/18/4/043042.

[44] P. Götzfried et al. "Droplet dynamics and fine-scale structure in a shearless turbulent mixing layer with phase changes". In: *Journal of Fluid Mechanics* 814 (2017), pp. 452–483. DOI: 10.1017/jfm.2017.23.

[45] W.W. Grabowski. "Dynamics of cumulus entrainment". In: *Geophysical and Astrophysical Convection*. Ed. by P. Fox and R.M. Kerr. Gordon and Breach Science Publishers, Sydney, 2000, pp. 107–127.

[46] W.W. Grabowski and L.P. Wang. "Growth of Cloud Droplets in a Turbulent Environment". In: *Annual Review of Fluid Mechanics* 45.1 (2013), pp. 293–324. DOI: 10.1146/annurev-fluid-011212-140750.

[47] Z. Guo, B. Shi, and C. Zheng. "A coupled lattice BGK model for the Boussinesq equations". In: *International Journal for Numerical Methods in Fluids* 39.4 (2002), pp. 325–342. DOI: 10.1002/fld.337.

[48] Z. Guo, C. Zheng, and B. Shi. "An extrapolation method for boundary conditions in lattice Boltzmann method". In: *Physics of Fluids* 14.6 (2002), pp. 2007–2010. DOI: 10.1063/1.1471914.

[49] J.D. Hader, T.P. Wright, and M.D. Petters. "Contribution of pollen to atmospheric ice nuclei concentrations". In: *Atmospheric Chemistry and Physics* 14.11 (2014), pp. 5433–5449. DOI: 10.5194/acp-14-5433-2014.

[50] R.L. Harris-Hobbs and W.A. Cooper. "Field Evidence Supporting Quantitative Predictions of Secondary Ice Production Rates". In: *Journal of the Atmospheric Sciences* 44.7 (1987), pp. 1071–1082. DOI: 10.1175/1520-0469(1987)044<1071:FESQPO>2.0.CO;2.

[51] A. Heymsfield and P. Willis. "Cloud Conditions Favoring Secondary Ice Particle Production in Tropical Maritime Convection". In: *Journal of the Atmospheric Sciences* 71.12 (2014), pp. 4500–4526. DOI: 10.1175/JAS-D-14-0093.1.

[52] M.A.T. van Hinsberg et al. "Optimal interpolation schemes for particle tracking in turbulence". In: *Phys. Rev. E* 87 (4 2013), p. 043307. DOI: 10.1103/PhysRevE.87.043307.

[53] M. Hochbruck and A. Ostermann. "Exponential integrators". In: *Acta Numerica* 19 (2010), 209–286. DOI: 10.1017/S0962492910000048.

[54] R.J. Hogan et al. "Estimate of the global distribution of stratiform supercooled liquid water clouds using the LITE lidar". In: *Geophysical Research Letters* 31.5 (2004). DOI: 10.1029/2003GL018977.

[55] C. Hoose and O. Möhler. "Heterogeneous ice nucleation on atmospheric aerosols: a review of results from laboratory experiments". In: *Atmospheric Chemistry and Physics* 12.20 (2012), pp. 9817–9854. DOI: 10.5194/acp-12-9817-2012.

[56] "Chapter 1 Identification of Clouds". In: *Cloud Dynamics*. Ed. by R.A. Houze. Vol. 53. International Geophysics. Academic Press, 1993, pp. 3–25. DOI: 10.1016/S0074-6142(08)62842-9.

[57] J. Huang. "A Simple Accurate Formula for Calculating Saturation Vapor Pressure of Water and Ice". In: *Journal of Applied Meteorology and Climatology* 57.6 (2018), pp. 1265–1272. DOI: 10.1175/JAMC-D-17-0334.1.

[58] Y. Huang et al. "Factors controlling secondary ice production in cumulus clouds". In: *Quarterly Journal of the Royal Meteorological Society* 143.703 (2017), pp. 1021–1031. DOI: 10.1002/qj.2987.

[59] J.G. Hudson and S. Noble. "CCN and Vertical Velocity Influences on Droplet Concentrations and Supersaturations in Clean and Polluted Stratus Clouds". In: *Journal of the Atmospheric Sciences* 71.1 (2013), pp. 312–331. DOI: 10.1175/JAS-D-13-086.1.

[60] P.J. Huffman. "Supersaturation Spectra of AgI and Natural Ice Nuclei". In: *Journal of Applied Meteorology* 12.6 (1973), pp. 1080–1082. DOI: 10.1175/1520-0450(1973)012<1080:SSOAAN>2.0.CO;2.

[61] M. Iovieno, C. Cavazzoni, and D. Tordella. "A new technique for a parallel dealiased pseudospectral Navier–Stokes code". In: *Computer Physics Communications* 141.3 (2001), pp. 365–374. ISSN: 0010-4655. DOI: 10.1016/S0010-4655(01)00433-7.

[62] M. Iovieno et al. "Mixing of a passive scalar across a thin shearless layer: concentration of intermittency on the sides of the turbulent interface". In: *Journal of Turbulence* 15.5 (2014), pp. 311–334. DOI: 10.1080/14685248.2014.905393.

[63] P.J. Ireland and L.R. Collins. "Direct numerical simulation of inertial particle entrainment in a shearless mixing layer". In: *Journal of Fluid Mechanics* 704 (2012), pp. 301–332. DOI: 10.1017/jfm.2012.241.

[64] T. Ishihara, T. Gotoh, and Y. Kaneda. "Study of High–Reynolds Number Isotropic Turbulence by Direct Numerical Simulation". In: *Annual Review of Fluid Mechanics* 41.1 (2009), pp. 165–180. DOI: 10.1146/annurev.fluid.010908.165203.

[65] I. Jen-La Plante et al. "Physics of Stratocumulus Top (POST): turbulence characteristics". In: *Atmospheric Chemistry and Physics* 16.15 (2016), pp. 9711–9725. DOI: 10.5194/acp-16-9711-2016.

[66] T.A. Johnson and V.C. Patel. "Flow past a sphere up to a Reynolds number of 300". In: *Journal of Fluid Mechanics* 378 (1999), pp. 19–70. DOI: 10.1017/S0022112098003206.

[67] Z.A. Kanji et al. "Overview of Ice Nucleating Particles". In: *Meteorological Monographs* 58 (2017), pp. 1.1–1.33. DOI: 10.1175/AMSMONOGRAPHS-D-16-0006.1.

[68] G.G. Katul et al. "Active Turbulence and Scalar Transport near the Forest–Atmosphere Interface". In: *Journal of Applied Meteorology* 37.12 (1998), pp. 1533–1546. DOI: 10.1175/1520-0450(1998)037<1533:ATASTN>2.0.CO;2.

[69] A.V. Korolev and I.P. Mazin. "Supersaturation of Water Vapor in Clouds". In: *Journal of the Atmospheric Sciences* 60.24 (2003), pp. 2957–2974. DOI: 10.1175/1520-0469(2003)060<2957:SOWVIC>2.0.CO;2.

[70] M. Kotouč, G. Bouchet, and J. Dušek. "Transition to turbulence in the wake of a fixed sphere in mixed convection". In: *Journal of Fluid Mechanics* 625 (2009), pp. 205–248. DOI: 10.1017/S0022112008005557.

[71] H. Kramers. "Heat transfer from spheres to flowing media". In: *Physica* 12.2 (1946), pp. 61–80. ISSN: 0031-8914. DOI: 10.1016/S0031-8914(46)80024-7.

[72] M. Krayer et al. "On the ice-nucleating potential of warm hydrometeors in mixed-phase clouds". In: *Atmospheric Chemistry and Physics Discussions* 2020 (2020), pp. 1–21. DOI: 10.5194/acp-2020-136.

[73] S.M. Kreidenweis, M. Petters, and U. Lohmann. "100 Years of Progress in Cloud Physics, Aerosols, and Aerosol Chemistry Research". In: *Meteorological Monographs* 59 (2019), pp. 11.1–11.72. DOI: 10.1175/AMSMONOGRAPHS-D-18-0024.1.

[74] T. Krüger et al. *Lattice Boltzmann Method: Fundamentals and Engineering Applications with Computer Codes*. Springer, Cham, 2017. DOI: 10.1007/978-3-319-44649-3.

[75] M. Kulmala et al. "Direct Observations of Atmospheric Aerosol Nucleation". In: *Science* 339.6122 (2013), pp. 943–946. DOI: 10.1126/science.1227385.

[76] M. Kulmala et al. "Toward Direct Measurement of Atmospheric Nucleation". In: *Science* 318.5847 (2007), pp. 89–92. DOI: 10.1126/science.1144124.

[77] B. Kumar, J. Schumacher, and R.A. Shaw. "Cloud microphysical effects of turbulent mixing and entrainment". In: *Theoretical and Computational Fluid Dynamics* 27.3 (2013), pp. 361–376. ISSN: 1432-2250. DOI: 10.1007/s00162-012-0272-z.

[78] B. Kumar, J. Schumacher, and R.A. Shaw. "Lagrangian Mixing Dynamics at the Cloudy–Clear Air Interface". In: *Journal of the Atmospheric Sciences* 71.7 (2014), pp. 2564–2580. DOI: 10.1175/JAS-D-13-0294.1.

[79] B. Kumar et al. "Cloud-edge mixing: Direct numerical simulation and observations in Indian Monsoon clouds". In: *Journal of Advances in Modeling Earth Systems* 9.1 (2017), pp. 332–353. DOI: 10.1002/2016MS000731.

[80] B. Kumar et al. "Scale Dependence of Cloud Microphysical Response to Turbulent Entrainment and Mixing". In: *Journal of Advances in Modeling Earth Systems* 10.11 (2018), pp. 2777–2785. DOI: 10.1029/2018MS001487.

[81] A.S. Lanotte, A. Seminara, and F. Toschi. "Cloud Droplet Growth by Condensation in Homogeneous Isotropic Turbulence". In: *Journal of the Atmospheric Sciences* 66.6 (2009), pp. 1685–1697. DOI: 10.1175/2008JAS2864.1.

[82] S.G. Lasher-trapp, W.A. Cooper, and A.M. Blyth. "Broadening of droplet size distributions from entrainment and mixing in a cumulus cloud". In: *Quarterly Journal of the Royal Meteorological Society* 131.605 (2005), pp. 195–220. DOI: 10.1256/qj.03.199.

[83] J. Latt et al. "Palabos: Parallel Lattice Boltzmann Solver". In: *Computers & Mathematics with Applications* (2020). ISSN: 0898-1221. DOI: 10.1016/j.camwa.2020.03.022.

[84] K.M. Lau and H.T. Wu. "Warm rain processes over tropical oceans and climate implications". In: *Geophysical Research Letters* 30.24 (2003). DOI: 10.1029/2003GL018567.

[85] K. Lehmann, H. Siebert, and R.A. Shaw. "Homogeneous and Inhomogeneous Mixing in Cumulus Clouds: Dependence on Local Turbulence Structure". In: *Journal of the Atmospheric Sciences* 66.12 (2009), pp. 3641–3659. DOI: 10.1175/2009JAS3012.1.

[86] M. Lesieur. *Turbulence in Fluids*. Vol. 84. Springer Netherlands, 2008. DOI: 10.1007/978-1-4020-6435-7.

[87] U. Lohmann. "AEROSOLS | Aerosol–Cloud Interactions and Their Radiative Forcing". In: *Encyclopedia of Atmospheric Sciences (Second Edition)*. Ed. by G.R. North, J. Pyle, and F. Zhang. Second Edition. Oxford: Academic Press, 2015, pp. 17–22. DOI: 10.1016/B978-0-12-382225-3.00052-9.

[88] M. Lothon, D.H. Lenschow, and S.D. Mayor. "Doppler Lidar Measurements of Vertical Velocity Spectra in the Convective Planetary Boundary Layer". In: *Boundary-Layer Meteorology* 132.2 (2009), pp. 205–226. ISSN: 1573-1472. DOI: 10.1007/s10546-009-9398-y.

[89] A. de Lozar and J. P. Mellado. "Cloud droplets in a bulk formulation and its application to buoyancy reversal instability". In: *Quarterly Journal of the Royal Meteorological Society* 140.682 (2014), pp. 1493–1504. DOI: 10.1002/qj.2234.

[90] R.H. Magarvey and R.L. Bishop. "Transition Ranges for Three-Dimensional Wakes". In: *Canadian Journal of Physics* 39.10 (1961), pp. 1418–1422. DOI: 10.1139/p61-169.

[91] S.P. Malinowski et al. "Physics of Stratocumulus Top (POST): turbulent mixing across capping inversion". In: *Atmospheric Chemistry and Physics* 13.24 (2013), pp. 12171–12186. DOI: 10.5194/acp-13-12171-2013.

[92] M.R. Maxey and J. Riley. "Equation of motion for a small rigid sphere in a nonuniform flow". In: *The Physics of Fluids* 26.4 (1983), pp. 883–889. DOI: 10.1063/1.864230.

[93]   G. McFiggans et al. "The effect of physical and chemical aerosol properties on warm cloud droplet activation". In: *Atmospheric Chemistry and Physics* 6.9 (2006), pp. 2593–2649. DOI: 10.5194/acp-6-2593-2006.

[94]   J.P. Mellado. "Cloud-Top Entrainment in Stratocumulus Clouds". In: *Annual Review of Fluid Mechanics* 49.1 (2017), pp. 145–169. DOI: 10.1146/annurev-fluid-010816-060231.

[95]   M.P. Meyers, P.J. DeMott, and W.R. Cotton. "New Primary Ice-Nucleation Parameterizations in an Explicit Cloud Model". In: *Journal of Applied Meteorology* 31.7 (1992), pp. 708–721. DOI: 10.1175/1520-0450(1992)031<0708:NPINPI>2.0.CO;2.

[96]   E.E. Michaelides. *Particles, Bubbles and Drops.* World Scientific, 2006. DOI: 10.1142/6018.

[97]   A.K. Mishra. "Investigating changes in cloud cover using the long-term record of precipitation extremes". In: *Meteorological Applications* 26.1 (2019), pp. 108–116. DOI: 10.1002/met.1745.

[98]   A.A. Mohamad. *The Lattice Boltzmann Method: Principles and Practice.* Springer-Verlag London Ltd., 2019. DOI: 10.1007/978-1-4471-7423-3.

[99]   A.S. Monin and A.M. Yaglom. *Statistical Fluid Mechanics: Mechanics of Turbulence.* Vol. 2. The MIT Press, 1981.

[100] R.B. Montgomery. "Viscosity and Thermal Conductivity of Air and Diffusivity of Water Vapor in Air". In: *Journal of Meteorology* 4.6 (1947), pp. 193–196. DOI: 10.1175/1520-0469(1947)004<0193:VATCOA>2.0.CO;2.

[101] S.C. Mossop. "Production of secondary ice particles during the growth of graupel by riming". In: *Quarterly Journal of the Royal Meteorological Society* 102.431 (1976), pp. 45–57. DOI: 10.1002/qj.49710243104.

[102] B.J. Murray et al. "Ice nucleation by particles immersed in supercooled cloud droplets". In: *Chem. Soc. Rev.* 41 (19 2012), pp. 6519–6554. DOI: 10.1039/C2CS35200A.

[103] V. Nair, T. Heus, and M. van Reeuwijk. "Dynamics of Subsiding Shells in Actively Growing Clouds with Vertical Updrafts". In: *Journal of the Atmospheric Sciences* 77.4 (2020), pp. 1353–1369. DOI: 10.1175/JAS-D-19-0018.1.

[104] R. Natarajan and A. Acrivos. "The instability of the steady flow past spheres and disks". In: *Journal of Fluid Mechanics* 254 (1993), pp. 323–344. DOI: 10.1017/S0022112093002150.

[105] N. Nix and N. Fukuta. "Nonsteady-State Kinetics of Droplet Growth in Cloud Physics". In: *Journal of the Atmospheric Sciences* 31.5 (1974), pp. 1334–1343. DOI: 10.1175/1520-0469(1974)031<1334:NSKODG>2.0.CO;2.

[106]   C.S. Nor Azwadi and S. Syahrullail. "A three-dimension double-population thermal lattice BGK model for simulation of natural convection heat transfer in a cubic cavity". In: *WSEAS Transactions on Mathematics* 8 (2009), pp. 561–571.

[107]   R. Onishi, K. Matsuda, and K. Takahashi. "Lagrangian Tracking Simulation of Droplet Growth in Turbulence–Turbulence Enhancement of Autoconversion Rate". In: *Journal of the Atmospheric Sciences* 72.7 (2015), pp. 2591–2607. DOI: 10.1175/JAS-D-14-0292.1.

[108]   H. Opadrishta. "Multiple-relaxation-time lattice Boltzmann simulations of turbulent pipe flows". MA thesis. Department of Mechanical Engineering, University of Delaware, 2016. URL: http://udspace.udel.edu/handle/19716/21444.

[109]   D. Ormières and M. Provansal. "Transition to Turbulence in the Wake of a Sphere". In: *Phys. Rev. Lett.* 83 (1 1999), pp. 80–83. DOI: 10.1103/PhysRevLett.83.80.

[110]   V.E. Perrin and H.J.J. Jonker. "Lagrangian Droplet Dynamics in the Subsiding Shell of a Cloud Using Direct Numerical Simulations". In: *Journal of the Atmospheric Sciences* 72.10 (2015), pp. 4015–4028. DOI: 10.1175/JAS-D-15-0045.1.

[111]   M.D. Petters and T.P. Wright. "Revisiting ice nucleation from precipitation samples". In: *Geophysical Research Letters* 42.20 (2015), pp. 8758–8766. DOI: 10.1002/2015GL065733.

[112]   M.B. Pinsky and A.P. Khain. "Turbulence effects on droplet growth and size distribution in clouds—A review". In: *Journal of Aerosol Science* 28.7 (1997), pp. 1177–1214. ISSN: 0021-8502. DOI: 10.1016/S0021-8502(97)00005-0.

[113]   M.B. Pinsky, A.P. Khain, and H. Krugliak. "Collisions of Cloud Droplets in a Turbulent Flow. Part V: Application of Detailed Tables of Turbulent Collision Rate Enhancement to Simulation of Droplet Spectra Evolution". In: *Journal of the Atmospheric Sciences* 65.2 (2008), pp. 357–374. DOI: 10.1175/2007JAS2358.1.

[114]   P. Prabhakaran et al. "Can Hail and Rain Nucleate Cloud Droplets?" In: *Phys. Rev. Lett.* 119 (12 2017), p. 128701. DOI: 10.1103/PhysRevLett.119.128701.

[115]   P. Prabhakaran et al. "High Supersaturation in the Wake of Falling Hydrometeors: Implications for Cloud Invigoration and Ice Nucleation". In: *Geophysical Research Letters* 47.10 (2020), e2020GL088055. DOI: 10.1029/2020GL088055.

[116] H.R. Pruppacher and J.D. Klett. *Microphysics of Clouds and Precipitation.* second. Springer, Dordrecht, 2010. DOI: 10.1007/978-0-306-48100-0.

[117] Y. Qian, D. D'Humières, and P. Lallemand. "Lattice BGK models for Navier-Stokes equation". In: *Europhysics Letters* 17.6 (1992), pp. 479–484.

[118] C. Rabe, J. Malet, and F. Feuillebois. "Experimental investigation of water droplet binary collisions and description of outcomes with a symmetric Weber number". In: *Physics of Fluids - PHYS FLUIDS* 22 (2010), 047101–(1:11). DOI: 10.1063/1.3392768.

[119] A. Radkevich et al. "Scaling turbulent atmospheric stratification. III: Space–time stratification of passive scalars from lidar data". In: *Quarterly Journal of the Royal Meteorological Society* 134.631 (2008), pp. 317–335. DOI: 10.1002/qj.203.

[120] W.E. Ranz and W.R. Marshall-Jr. "Evaporation from drops : Part I and II". In: *Chemical Engineering Program* 48 (1952), pp. 141–146, 173–180.

[121] A. Richter and P.A. Nikrityuk. "Drag forces and heat transfer coefficients for spherical, cuboidal and ellipsoidal particles in cross flow at sub-critical Reynolds numbers". In: *International Journal of Heat and Mass Transfer* 55.4 (2012), pp. 1343–1354. ISSN: 0017-9310. DOI: 10.1016/j.ijheatmasstransfer.2011.09.005.

[122] F.W. Roos and W.W. Willmarth. "Some experimental results on sphere and disk drag". In: *AIAA Journal* 9.2 (1971), pp. 285–291. DOI: 10.2514/3.6164.

[123] W.C. de Rooy et al. "Entrainment and detrainment in cumulus convection: an overview". In: *Quarterly Journal of the Royal Meteorological Society* 139.670 (2013), pp. 1–19. DOI: 10.1002/qj.1959.

[124] D. Rosenfeld et al. "Satellite retrieval of cloud condensation nuclei concentrations by using clouds as CCN chambers". In: *Proceedings of the National Academy of Sciences* 113.21 (2016), pp. 5828–5834. DOI: 10.1073/pnas.1514044113.

[125] M.A. Safi, N. Prasianakis, and S. Turek. "Benchmark computations for 3D two-phase flows: A coupled lattice Boltzmann-level set study". In: *Computers Mathematics with Applications* 73.3 (2017), pp. 520–536. ISSN: 0898-1221. DOI: 10.1016/j.camwa.2016.12.014.

[126] J.H. Seinfeld and S.N. Pandis. *Atmospheric Chemistry and Physics: From Air Pollution to Climate Change.* 2nd ed. John Wiley & Sons, New York, 2006.

[127] R.A. Shaw. "Particle-turbulence interactions in atmospheric clouds". In: *Annual Review of Fluid Mechanics* 35.1 (2003), pp. 183–227. DOI: 10.1146/annurev.fluid.35.101101.161125.

[128] H. Siebert and R.A. Shaw. "Supersaturation Fluctuations during the Early Stage of Cumulus Formation". In: *Journal of the Atmospheric Sciences* 74.4 (2017), pp. 975–988. DOI: 10.1175/JAS-D-16-0115.1.

[129] H. Siebert, R.A. Shaw, and Z. Warhaft. "Statistics of Small-Scale Velocity Fluctuations and Internal Intermittency in Marine Stratocumulus Clouds". In: *Journal of the Atmospheric Sciences* 67.1 (2010), pp. 262–273. DOI: 10.1175/2009JAS3200.1.

[130] H. Siebert et al. "High-resolution measurement of cloud microphysics and turbulence at a mountaintop station". In: *Atmospheric Measurement Techniques* 8.8 (2015), pp. 3219–3228. DOI: 10.5194/amt-8-3219-2015.

[131] H. Siebert et al. "Probing Finescale Dynamics and Microphysics of Clouds with Helicopter-Borne Measurements". In: *Bulletin of the American Meteorological Society* 87.12 (2006), pp. 1727–1738. DOI: 10.1175/BAMS-87-12-1727.

[132] H. Siebert et al. "Towards understanding the role of turbulence on droplets in clouds: In situ and laboratory measurements". In: *Atmospheric Research* 97.4 (2010), pp. 426–437. ISSN: 0169-8095. DOI: 10.1016/j.atmosres.2010.05.007.

[133] G. Silva and V. Semiao. "First- and second-order forcing expansions in a lattice Boltzmann method reproducing isothermal hydrodynamics in artificial compressibility form". In: *Journal of Fluid Mechanics* 698 (2012), pp. 282–303. DOI: 10.1017/jfm.2012.83.

[134] B. Stevens and S. Bony. "What are climate models missing?" In: *Science* 340.6136 (2013), pp. 1053–1054. DOI: 10.1126/science.1237554.

[135] R.B. Stull. *An Introduction to Boundary Layer Meteorology.* Kluwer Academic, Dordrecht, 1988.

[136] S. Succi. *Lattice Boltzmann equation for fluid dynamics and beyond.* Oxford: Clarendon Press, 2001. ISBN: 0-19-850398-9.

[137] S. Sundaram and L. R Collins. "Numerical Considerations in Simulating a Turbulent Suspension of Finite-Volume Particles". In: *J. Comp. Phys.* 124 (2 1996), pp. 337–350. DOI: 10.1006/jcph.1996.0064.

[138] M. Tabata and K. Itakura. "A Precise Computation of Drag Coefficients of a Sphere". In: *International Journal of Computational Fluid Dynamics* 9.3-4 (1998), pp. 303–311. DOI: 10.1080/10618569808940861.

[139] S. Taneda. "Experimental Investigation of the Wake behind a Sphere at Low Reynolds Numbers". In: *Journal of the Physical Society of Japan* 11.10 (1956), pp. 1104–1108. DOI: 10.1143/JPSJ.11.1104.

134

[140] L. Thomas, W.W. Grabowski, and B. Kumar. "Diffusional growth of cloud droplets in homogeneous isotropic turbulence: DNS, scaled-up DNS, and stochastic model". In: *Atmospheric Chemistry and Physics* 20.14 (2020), pp. 9087–9100. DOI: `10.5194/acp-20-9087-2020`.

[141] F.B. Tian et al. "The lattice Boltzmann method and its applications in complex flows and fluid–structure interactions". In: *Proceedings of the Institution of Mechanical Engineers, Part C: Journal of Mechanical Engineering Science* 232.3 (2018), pp. 403–404. ISSN: 0954-4062. DOI: `10.1177/0954406218754913`.

[142] A.G. Tomboulides and S. A. Orszag. "Numerical investigation of transitional and weak turbulent flow past a sphere". In: *Journal of Fluid Mechanics* 416 (2000), pp. 45–73. DOI: `10.1017/S0022112000008880`.

[143] D. Tordella and M. Iovieno. "Numerical experiments on the intermediate asymptotics of shear-free turbulent transport and diffusion". In: *Journal of Fluid Mechanics* 549 (2006), pp. 429–441. DOI: `10.1017/S0022112005007688`.

[144] D. Tordella and M. Iovieno. "Small-Scale Anisotropy in Turbulent Shearless Mixing". In: *Phys. Rev. Lett.* 107 (19 2011), p. 194501. DOI: `10.1103/PhysRevLett.107.194501`.

[145] J.D. Tritton. *Physical Fluid Dynamics*. Springer Netherlands, 1977. DOI: `10.1007/978-94-009-9992-3`.

[146] A. Unnikrishnan and R.P. Chhabra. "An experimental study of motion of cylinders in newtonian fluids: Wall effects and drag coefficient". In: *The Canadian Journal of Chemical Engineering* 69.3 (1991), pp. 729–735. DOI: `10.1002/cjce.5450690315`.

[147] P.A. Vaillancourt and M. K. Yau. "Review of Particle-Turbulence Interactions and Consequences for Cloud Physics". In: *Bulletin of the American Meteorological Society* 81.2 (2000), pp. 285–298. DOI: `10.1175/1520-0477(2000)081<0285:ROPIAC>2.3.CO;2`.

[148] P.A. Vaillancourt, M.K. Yau, and W.W. Grabowski. "Microscopic Approach to Cloud Droplet Growth by Condensation. Part I: Model Description and Results without Turbulence". In: *Journal of the Atmospheric Sciences* 58.14 (2001), pp. 1945–1964. DOI: `10.1175/1520-0469(2001)058<1945:MATCDG>2.0.CO;2`.

[149] P.A. Vaillancourt et al. "Microscopic Approach to Cloud Droplet Growth by Condensation. Part II: Turbulence, Clustering, and Condensational Growth". In: *Journal of the Atmospheric Sciences* 59.24 (2002), pp. 3421–3435. DOI: `10.1175/1520-0469(2002)059<3421:MATCDG>2.0.CO;2`.

135

[150] A. Waldvogel. "The N0 Jump of Raindrop Spectra". In: *Journal of the Atmospheric Sciences* 31.4 (1974), pp. 1067–1078. DOI: `10.1175/1520-0469(1974)031<1067:TJORS>2.0.CO;2`.

[151] J. Wang et al. "Amazon boundary layer aerosol concentration sustained by vertical transport during rainfall". In: *Nature (London)* 539.7629 (2016). ISSN: 0028-0836. DOI: `10.1038/nature19819`.

[152] J.B. Will, N.P. Kruyt, and C.H. Venner. "An experimental study of forced convective heat transfer from smooth, solid spheres". In: *International Journal of Heat and Mass Transfer* 109 (2017), pp. 1059–1067. ISSN: 0017-9310. DOI: `10.1016/j.ijheatmasstransfer.2017.02.018`.

[153] R. Wood. "Stratocumulus Clouds". In: *Monthly Weather Review* 140.8 (2012), pp. 2373–2423. DOI: `10.1175/MWR-D-11-00121.1`.

[154] J. Wu and C. Shu. "Simulation of three-dimensional flows over moving objects by an improved immersed boundary–lattice Boltzmann method". In: *International Journal for Numerical Methods in Fluids* 68.8 (2012), pp. 977–1004. DOI: `10.1002/fld.2589`.

[155] F. Yang et al. "Cloud droplet size distribution broadening during diffusional growth: ripening amplified by deactivation and reactivation". In: *Atmospheric Chemistry and Physics* 18.10 (2018), pp. 7313–7328. DOI: `10.5194/acp-18-7313-2018`.

[156] T. Yuan et al. "Estimating glaciation temperature of deep convective clouds with remote sensing data". In: *Geophysical Research Letters* 37.8 (2010). DOI: `10.1029/2010GL042753`.

[157] T. Yuge. "Experiments on Heat Transfer From Spheres Including Combined Natural and Forced Convection". In: *Journal of Heat Transfer* 82.3 (1960), pp. 214–220. DOI: `10.1115/1.3679912`.

[158] L. Zaichik, V.M. Alipchenkov, and E.G. Sinaiski. *Particles in Turbulent Flows*. Vol. 84. Wiley-VCH Verlag GmbH & Co. KGaA, 2009.